

RICE UNIVERSITY

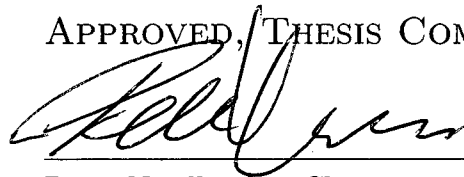
**Plasmonic Properties of Metallic Nanostructures with  
Reduced Symmetry**

by

**Yanpeng Wu**

A THESIS SUBMITTED  
IN PARTIAL FULFILLMENT OF THE  
REQUIREMENTS FOR THE DEGREE  
**DOCTOR OF PHILOSOPHY**

APPROVED, THESIS COMMITTEE:



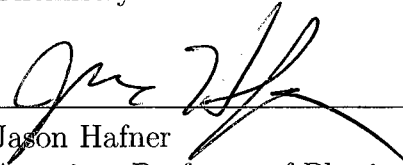
---

Peter Nordlander, Chair  
Professor of Physics and Astronomy;  
Professor of Electrical and Computer  
Engineering



---

Naomi Halas  
Stanley C. Moore Professor of Electrical  
and Computer Engineering; Professor of  
Chemistry



---

Jason Hafner  
Associate Professor of Physics and  
Astronomy; Associate Professor of  
Chemistry

Houston, Texas

December, 2009

UMI Number: 3421332

All rights reserved

INFORMATION TO ALL USERS

The quality of this reproduction is dependent upon the quality of the copy submitted.

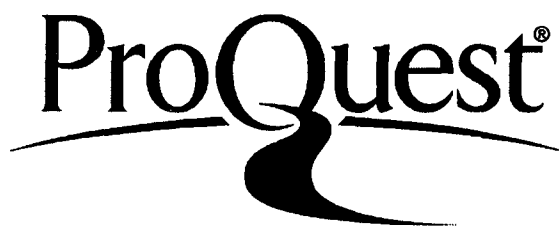
In the unlikely event that the author did not send a complete manuscript and there are missing pages, these will be noted. Also, if material had to be removed, a note will indicate the deletion.



UMI 3421332

Copyright 2010 by ProQuest LLC.

All rights reserved. This edition of the work is protected against unauthorized copying under Title 17, United States Code.



ProQuest LLC  
789 East Eisenhower Parkway  
P.O. Box 1346  
Ann Arbor, MI 48106-1346

# ABSTRACT

## Plasmonic Properties of Metallic Nanostructures with Reduced Symmetry

by

Yanpeng Wu

In this thesis, we theoretically study the plasmonic properties of metallic nanostructures with reduced symmetry using the Plasmon Hybridization (PH) and the Finite Difference Time Domain (FDTD) methods. Both methods provide efficient and accurate results for calculating physical properties of metallic nanostructures, including the optical cross section spectra, the local electromagnetic fields and induced charge densities around the surface of the nanostructures.

The PH method is applied to a nanoshell with an offset core (nanoegg). The results show that the reduction in symmetry relaxes the selection rules in the hybridization of primitive plasmon modes, allowing for an admixture of dipolar components in higher multipolar plasmon modes of the particle. The hybridization therefore makes higher multipolar nanoshell plasmon modes dipole active, resulting in a core offset-dependent shift for the plasmon energies and a multi-peaked feature in the optical

spectrum. The polarization dependence of the optical absorption spectra is found to be relatively weak. The calculations also show significantly larger local-field enhancements on nanoegg's external surface than the equivalent concentric spherical nanostructure. The results agree very well with results from FDTD simulations and experiments, suggesting applications of nanoeggs as substrates for surface enhanced Raman spectroscopy (SERS).

Another comprehensive investigation of the plasmonic interactions of individual metallic nanoshells with dielectric substrates is performed using the FDTD method. The results show that the adjacent dielectric breaks the spherical symmetry of individual nanoshell and lifts the degeneracy of the dipole and quadrupole plasmon modes, introducing significant polarization dependent redshifts and hybridization of the nanoparticle plasmon resonances. The results also show that, for small nanoparticle-substrate separations and substrates with large dielectric permittivities, the hybridized quadrupolar nanoparticle plasmon resonances also appear in the scattering spectrum. We discuss different numerical approaches in FDTD simulations for calculating the scattering spectrum in typical dark-field scattering geometries. We also discuss issues of numerical convergence and show that the scattering spectra can be calculated using finite substrate slab models. The results agree very well with experiments, showing that dielectric substrates matter in optical measurements of plasmonic nanoparticles.

FDTD method is also applied to a bowtie-shaped nanostructure (nanobowtie).

The calculations show significantly large SERS enhancements across a broad bandwidth of exciting wavelengths because of the complicated mode structure possible in the interelectrode gap. Nanometer-scale asperities in the gap area break the interelectrode symmetry of the structure, resulting in optical excitations of many interelectrode modes besides the simple dipolar plasmon mode commonly considered. The broken symmetry also leads to much less dependence of the calculated enhancement on polarization direction, as seen experimentally. The calculations confirm that the electromagnetic enhancement is confined in the normal direction to the film thickness and to a region comparable to the radius of curvature of the asperity. The calculated electromagnetic enhancements can exceed  $10^{11}$ , approaching that sufficient for single-molecule sensitivity. We also compare the calculated extinction spectra for various values of interelectrode conductance connecting the source and drain. The results show that negligible charge transfer occurs between the two electrodes until junction conductance approaches the conductance quantum,  $G_0 = 2e^2/h$ .

## Acknowledgments

I am very grateful to my advisor, Prof. Peter Nordlander, for his guidance and supervisal. His exceptional intuition in physics, solid theoretical background and a persistent passion for seeking simple but elegant physical pictures have greatly impressed me and have been constantly inspiring my research. His patience and encouragement are also great appreciated. Additionally the experience I gained as a Linux administrator and in developing a large-scale parallel computing software package will be an invaluable life skill. I would like to thank the other members of my thesis committee, Prof. Naomi Halas and Prof. Jason Hafner for taking their time attending in my thesis defense. I would like to thank all of my previous and current colleagues, particularly Dr. Chris Oubre, Dr. Daniel Brandl, Dr. Fei Le, Dr. Feng Hao, Mr. Britan Willingham, Dr. Chizuko Dutta, Mr. Tamer Ali for their invaluable discussions. I would like to thank my collaborators in research, Dr. Hui Wang, Mr. Britt Lassiter, Mr. Mark Knight, Dr. Colleen Nehl and Mr. Daniel Ward for their contributions and enlightenment to my research. I also acknowledge the Laboratory for Nanophotonics (LANP), which is a great platform for my exposure to latest publications and discussions with experimentalists. I should definitely thank my family, especially my wife Qi Gao who has been constantly supporting me. Last but not least, I acknowledge support from the funding providers. This work is supported by the

U.S. Army Research laboratory and the U.S. Army Research Office under contract / grant number W911NF-04-1-0203, the Robert A. Welch Foundation under grant C-1222, and by NSF under grants EEC-0304097, ECS-0421108 and CNS-0421109.

# Contents

Abstract	ii
Acknowledgments	v
List of Figures	x
<b>1 Introduction</b>	<b>1</b>
<b>2 Theoretical Methods</b>	<b>10</b>
2.1 Plasmon hybridization method . . . . .	10
2.2 FDTD method . . . . .	14
<b>3 Nonconcentric Nanoshells (Nanoeggs)</b>	<b>18</b>
3.1 Introduction . . . . .	18
3.2 Plasmon energies . . . . .	21
3.3 Optical absorption . . . . .	33
3.4 Electromagnetic field enhancements . . . . .	36
3.5 Single-particle dark-field scattering . . . . .	38
3.6 Conclusion . . . . .	39
<b>4 Nanoparticles near Dielectric Substrates</b>	<b>42</b>
4.1 Introduction . . . . .	42
4.2 Optical properties of a nanoshell near a dielectric slab . . . . .	45



4.2.1	Substrate induced symmetry breaking and hybridization . . . .	46
4.2.2	Finite slab effects . . . . .	52
4.2.3	Effect of nanoparticle-substrate separation . . . . .	55
4.2.4	Effect of substrate permittivity . . . . .	56
4.3	Dark-field Scattering . . . . .	57
4.4	Experiments and FEM results . . . . .	63
4.5	Conclusion . . . . .	66
<b>5</b>	<b>Nanobowtie structures</b>	<b>68</b>
5.1	Introduction . . . . .	68
5.2	FDTD calculations and discussions . . . . .	71
5.2.1	Perfectly symmetric bowties . . . . .	72
5.2.2	Bowties with nanoscale asperities . . . . .	74
5.2.3	Hot spots . . . . .	75
5.2.4	Interelectrode conductance . . . . .	81
5.3	Conclusion . . . . .	84
<b>6</b>	<b>Conclusions</b>	<b>86</b>
<b>A</b>	<b>Facts of RiceFDTD3.0</b>	<b>89</b>
A.1	Real-time information . . . . .	89
A.2	Parallelism . . . . .	89

	ix
<b>B Derivation of the Lagrangian</b>	<b>95</b>
B.1 Matrix notation . . . . .	95
B.1.1 Kinetic energy . . . . .	96
B.1.2 Potential energy . . . . .	98
B.1.3 Optical absorption . . . . .	102
<b>C Convergence Test for modeling an extended dielectric surface</b>	<b>104</b>
<b>References</b>	<b>106</b>

# List of Figures

2.1	Plasmon hybridization of metallic nanoshells . . . . .	13
2.2	Yee cell . . . . .	15
3.1	Synthesis of nanoeggs and comparison of experiments and FDTD results	20
3.2	Geometry and plasmon hybridization in a nanoegg . . . . .	23
3.3	Plasmon energies of a nanoegg as a function of the offset $D$ . . . . .	29
3.4	Comparison of plasmon energies obtained from FDTD and plasmon hybridization . . . . .	31
3.5	Calculated optical absorption spectra for a nanoegg . . . . .	35
3.6	Local electric field enhancements for a nanoshell and nanoeggs . . . . .	37
3.7	Normalized single-particle dark-field scattering spectra . . . . .	40
4.1	Geometry and parameters of the nanoshell/finite slab model . . . . .	46
4.2	Symmetry breaking in nanoshell/surface model . . . . .	48
4.3	Extinction spectra of the gold nanoshell/dielectric slab structure . . . . .	50
4.4	Effect of substrate size on the energy of the nanoshell plasmon resonances	54
4.5	Effect of nanoparticle-substrate separation $d$ on the energy of the nanoshell plasmon resonances. . . . .	56

4.6	Energies of the nanoshell plasmon resonances as a function of dielectric permittivity of the substrate . . . . .	57
4.7	Methods in FDTD simulations . . . . .	58
4.8	Comparison of extinction and dark-field scattering spectra with different methods . . . . .	61
4.9	Hybridizations between the quadrupolar and dipolar modes of nanoshells	63
4.10	Comparison of experiments and theoretical calculations . . . . .	65
5.1	Bowtie structures in experiments . . . . .	70
5.2	Geometry and parameters of the perfectly symmetric nanobowtie structure . . . . .	72
5.3	Calculated extinction spectra for bowties with different length . . . . .	73
5.4	Geometry and parameters of the nanobowtie structure with protrusions	75
5.5	Comparison of calculated extinction spectra for bowties with and without protrusions . . . . .	76
5.6	FDTD-calculated extinction spectrum and $ E ^4$ plot . . . . .	77
5.7	Maps of FDTD-calculated $ E $ for the 1535 nm mode . . . . .	78
5.8	Maps of FDTD-calculated $ E $ for the 937 nm mode . . . . .	79
5.9	Maps of FDTD-calculated $ E $ for the 746 nm mode . . . . .	80
5.10	The bowtie structure with an artificial molecule . . . . .	83

A.1	Real-time information of nanoshell plasmon resonances . . . . .	90
A.2	Global parallel algorithm in RiceFDTD . . . . .	92
A.3	A RiceFDTD simulation running across four different CPUs . . . . .	93
A.4	Scalability of RiceFDTD on STIC . . . . .	94
C.1	Convergence tests for modeling an extended dielectric surface in FDTD	105

# Chapter 1

## Introduction

Plasmons, the collective oscillations of the free electron gas density[1] are treated as quasi-particles originated from the quantization of plasma oscillations in metals. Using the Drude model[2], metals are modeled as free electron gas sitting on top of a uniform, positive charge background. The bulk plasmon energy is usually considered as a constant that only depends on the free electron density  $n_0$  and takes the form  $\omega_0 = \sqrt{4\pi n_0 e^2 / m_e}$ , where  $m_e$  is the electron mass.

With this model, people can easily understand why most metals and semiconductors possess shiny colors. It is because their bulk plasmon levels are usually at ultraviolet, so the electric field of incident visible light is screened by the free electrons in the metal and the incident light is simply reflected without any absorption.

Recently, the plasmonic properties of metallic nanostructures are of considerable scientific and technological importance. The plasmonic properties of a metallic nanoparticle are determined by its plasmon resonances, which are strongly dependent on particle geometry (size and shape), environment and the way they are excited, etc.

There has been a great desire to acquire multifunctional sensors with single-molecule sensitivity for a variety of sensing applications, from biochemical analysis to explosives detection. The geometrical sensitivity of plasmon resonances of metallic

nanoparticles and the ability to tune the plasmon resonances in these particles to wavelengths of interest for chemical and biological sensing have been one of the reasons for the growing interest in a rapidly expanding array of nanoparticle geometries, such as nanorods,[3, 4] nanorings,[5] nanocubes,[6, 7] triangular nanoprisms,[8, 9, 10] nanoshells,[11, 12] nanorice,[13] and branched nanocrystals.[14, 15] The resonant excitation of plasmons can lead to large electromagnetic field enhancements on the nanoparticle surfaces and in a nanoscale region outside of the nanoparticles, known as "hot spots", which greatly exceed the strength of the incident field and can result in enormous enhancements of the cross section for nonlinear optical spectroscopies such as Surface-Enhanced Raman Scattering (SERS). [16, 17, 18, 19, 20, 21, 22] This is because the Raman scattering rate is proportional to  $|E(\omega)|^2|E(\omega')|^2$  at the location of the objects detected (e.g. molecules), where  $|E(\omega)|$  is the electric field component at the frequency of the incident radiation, and  $|E(\omega')|$  is the component at the scattered frequency. The structural dependence of both the local-field and far-field optical properties of nanoparticles across the visible and near-infrared (NIR) spectral regions has enabled their use in a wide range of biomedical applications, an area of increasing importance and societal impact. [23, 24, 25, 26, 27]

Metallic nanoshells, spherical nanoparticles composed of a spherical dielectric core and a concentric metallic shell, are nanoparticles whose plasmon resonant energies are very sensitive to inner core and outer shell dimensions. [28, 29, 30, 31, 32, 33, 34] This

plasmonic tunability of nanoshells across the visible and infrared spectral regions has enabled a wide range of biomedical applications ranging from photothermal cancer therapy,[23, 35] as contrast agents in medical imaging,[24] drug delivery,[26] whole blood immunoassay,[27] and chemical sensors.[36] The plasmonic tunability of metallic nanoshells arises from the interaction of surface plasmons localized on the inner surface of the shell (cavity plasmons) and plasmons associated with the outer surface (sphere plasmons). [2, 37] In the limit of small particles (diameter much smaller than the wavelength of the incident light), only the dipolar plasmons can be excited.[38]

Reduced-symmetry nanoparticles such as nanoshells with defects are of considerable interest in SERS applications. The controlled texturing of their surfaces can lead to increased surface area and also increased electromagnetic field enhancements on their surfaces. [39, 40, 41, 42, 43] Such surface modification results in electric field enhancements occurring on open surface areas which may be advantageous compared to the field enhancements occurring in less accessible spots like nanoparticle junctions[44, 19, 45].

Plasmonic nanoparticles also exhibit a remarkable sensitivity to their environment, where interactions with adjacent structures and materials typically influence their plasmon properties in dramatic and easily observable ways. The influence of a directly adjacent[7] or an isotropically surrounding dielectric medium [46] also alters the plasmonic properties of a nanoparticle. [47, 48] This effect has been of tremen-



dous interest in the development of ultrasensitive localized surface plasmon resonant (LSPR) nanosensors capable of ultimately detecting individual molecular binding events. [49, 50]

The study of plasmonic nanoparticles at the individual nanostructure level has become a major experimental focus and has enabled numerous significant advances in our understanding of plasmons in nanoscale systems.[51] For example, in dark-field microspectroscopy, individual nanoparticles are dispersed onto a dielectric substrate, where UV-visible spectroscopy is subsequently performed on a nanostructure. Combining these local optical measurements with precise, nanoscale imaging of the individual nanostructure (e.g., scanning electron microscopy) allows us to relate the plasmonic properties of specific individual nanoparticles and their complexes to their specific nanoscale geometry. This enables quantitative comparison between the experimental spectra and theoretical calculations of their electromagnetic modes.

Given the success of this experimental approach, it is very important to examine the effect of the dielectric substrate on the plasmonic properties of the nanoparticle on its surface. Theoretically, the dielectric substrate breaks the symmetry of nanoparticles, lifting mode degeneracies and modifying the coupling of the plasmon modes to the far field. For metallic substrates, it has been well established that the interaction between the LSPR and the substrate plasmons can result in strongly redshifted hybridized plasmons containing admixtures of both the localized plasmon modes of the

nanoparticle and the propagating plasmon modes of the substrate. [52, 53, 54, 55, 56] These hybridized plasmon modes thus have mixed localized and propagating character and are fundamentally different from the original localized nanoparticle plasmon modes. For a nanoparticle near a dielectric surface, there are no substrate plasmons modes and the interaction results in a hybridization of the individual nanoparticle plasmon modes. This interaction can be simply understood using an image model, where the electromagnetic fields induced by a particular multipolar nanoparticle plasmon mode are screened by the substrate and acquire different multipolar components in the coordinate system centered on the nanoparticle. This screening, by the factor  $(\epsilon - 1)/(\epsilon + 1)$  where  $\epsilon$  is the permittivity of the substrate, thus mediates an interaction between multipolar plasmons of different order resulting in localized hybridized nanoparticle plasmons. For a nanoparticle embedded in a uniform dielectric, there is no such hybridization but only a redshift due to the dielectric screening. It is worth noting that the energy splitting caused by the presence of dielectric substrates can easily be misinterpreted as an anomalously broadened plasmon line shape for excitation of an individual nanoparticle with unpolarized light.

To design and fabricate a substrate for systematic SERS at the single-molecule level is even more challenging. Single-molecule SERS sensitivity was first clearly demonstrated using random aggregates of colloidal nanoparticles. [17, 16, 18, 57] Numerous other metal substrate configurations have been used for SERS, including

chemically engineered nanoparticles, [36, 58, 59] nanostructures defined by bottom-up patterning, [60, 61] and those made by traditional lithographic approaches.[62] In the most sensitive substrate geometries, incident light excites adjacent subwavelength nanoparticles or nanostructures, resulting in large field enhancements within the interparticle gap.[63, 64] Fractal aggregates of nanoparticles [65] can further increase field enhancements by focusing plasmon energy from larger length scales down to particular nanometer-scale hotspots. [45] However, precise and reproducible formation of such assemblies in predetermined locations has been extremely challenging. An alternative approach is tip-enhanced Raman spectroscopy (TERS), in which the incident light excites an interelectrode plasmon resonance localized between a sharp, metal scanned probe tip and an underlying metal substrate. Recent progress has been made in single-molecule TERS detection.[66, 67, 68] A similar approach was recently attempted using a mechanical break junction.[69] While useful for surface imaging, TERS requires feedback to control the tip-surface gap and is not scalable or readily integrated with other sensing modalities.

A scaleable and highly reliable method was recently demonstrated for producing planar extended electrodes with nanoscale spacings that exhibit very large SERS signals, with each electrode pair having one well-defined hot spot.[70] This nanoscale gap structures were also used to perform simultaneous measurements of electronic transport and SERS. [71] Conductance in nanoscale gap structures is dominated by

roughly a molecular volume. The conductance as a function of time is observed to correlate strongly with the SERS signal in the junctions measured. Conductance changes correlate with sudden changes in the intensity of sets of Raman modes and with spectral diffusion of mode positions. Experimental data suggest that both SERS and conductance changes are most likely due to changes in conformation and binding of an individual molecule. The combined data provide a great deal of information about the effect of molecular orientation and environment on both conduction and SERS. The most likely explanation for these results is that single-molecule multimodal sensing is possible. This combined measurement technique also opens the possibility of direct assessment of vibrational pumping and local heating in single-molecule electronic transport.

This thesis is focusing on the studies of plasmonic properties of metallic nanostructures with reduced symmetry and is comprised of the materials from the following publications:

- “Finite-Difference Time-Domain Modeling of the Optical Properties of Nanoparticles near Dielectric Substrates”, Yanpeng Wu and Peter Nordlander; *Journal of Physical Chemistry C* (Accepted, 2009)
- “Substrates Matter: Influence of an Adjacent Dielectric on an Individual Plasmonic Nanoparticle”, Mark W. Knight, Yanpeng Wu, J. Britt Lassiter, Peter Nordlander, Naomi J. Halas; *Nano Letters*, textbf9(5), 2188-2192 (2009)

- “Simultaneous Measurements of Electronic Conduction and Raman Response in Molecular Junctions”, Daniel R. Ward, Naomi J. Halas, Jacob W. Ciszek, James M. Tour, Yanpeng Wu, Peter Nordlander, Douglas Natelson; *Nano Letters*, **8**(3), 919-924 (2008)
- “Electromigrated Nanoscale Gaps for Surface-Enhanced Raman Spectroscopy”, Daniel R. Ward, Nathaniel K. Grady, Carly S. Levin, Naomi J. Halas, Yanpeng Wu, Peter Nordlander, Douglas Natelson; *Nano Letters*, **7**(5), 1396-1400 (2007)
- “Plasmon Hybridization in Nanoshells with a Nonconcentric Core”, Yanpeng Wu and Peter Nordlander; *Journal of Chemical Physics*, **125**, 124708 (2006)
- “Plasmons in Nanostructures with Reduced Symmetry”, Daniel Brandl, Yanpeng Wu and Peter Nordlander; *Proceedings of SPIE*, **6323**, 632311 (2006)
- “Symmetry Breaking in Individual Plasmonic Nanoparticles”, Hui Wang, Yanpeng Wu, Britt Lassiter, Colleen L. Nehl, Jason H. Hafner, Peter Nordlander, Naomi J. Halas; *Proceedings of the National Academy of Sciences of U.S.A.*, **103**(29), 10856-10860 (2006)
- “Plasmon Hybridization in Complex Metallic Nanostructures”, Peter Nordlander, Fei Le and Yanpeng Wu; *Proceedings of SPIE*, **5927** (2005)

This thesis is organized as follows. In Chapter 2 we briefly introduce two the-

oretical methods that we use for the study in this thesis: Plasmon Hybridization (PH) method and Finite Different Time Domain (FDTD) method. In Chapter 3 we study the core-offset dependent plasmonic properties of nonconcentric nanoshells (nanoeegs). In Chapter 4 we study the plasmonic properties of nanoshells near dielectric substrates. In Chapter 5 we apply FDTD in simulating planar extended electrodes with electromigrated nanoscale gaps (modeled as nanobowties). In Chapter 6 we present the main conclusions of this thesis.

# Chapter 2

## Theoretical Methods

In this thesis, we use two theoretical methods - Plasmon Hybridization (PH) and Finite-Difference Time-Domain (FDTD) to study both far-field (e.g., extinction, scattering and absorption spectra) and near-field (e.g., local electric field enhancements and surface charge densities) properties.

### 2.1 Plasmon hybridization method

The PH method is a quasi-static analytical approximation of the Maxwell's Equations, [2, 37]. In the PH method, the conduction electrons/plasmons of the nanostructure are considered to be a charged, incompressible and irrotational liquid situated on top of a rigid, uniformly charged positive background representing the ion cores. The ion cores are treated within the jellium approximation, so the positive background charge is assumed to be uniformly distributed within the particle's boundaries. Plasmon modes are self-sustained deformations of the electron liquid. Since the conduction electron liquid is incompressible, the only effect of such deformations is the appearance of surface charges. The electrostatic potential of these surface charges provides the restoring force driving the plasmon oscillations. The plasmons of the interacting system are therefore expressed in terms of the primitive plasmons of the elementary surface modes. Since the PH method does not include phase retardation

effect, our research with the PH method mainly focuses on quasi-static limit where the size of the particle is no larger than a quarter of the incident wavelength. The plasmonic interaction in the system is therefore modeled with instantaneous Coulomb potential.

The plasmon deformation field can be expressed as a gradient of a scalar potential  $\eta$  which satisfies Laplace equation in the nanostructure.[37] The potential  $\eta$  is expanded in a complete set of primitive plasmon modes appropriate for the geometry of the nanostructure,

$$\eta(\vec{r}, t) = \sum_i \dot{A}_i(t) \chi_i(\vec{r}). \quad (2.1)$$

The quantity  $A_i(t)$  refers to the time-dependent amplitude of a primitive plasmon mode with an associated deformation field  $\Delta\vec{x}(\vec{r}) = \nabla\chi_i(\vec{r})$  of the electron distribution. When background dielectrics such as dielectric embedding media or the background polarizability of the metals are present, the surface charges will be screened which reduce the interaction between the primitive plasmons.

Using the expression Eq. (2.1), the kinetic and potential energy of the primitive plasmons can be directly expressed in terms of the amplitudes of the primitive plasmon modes.[37] The resulting Lagrangian has the form

$$L = \vec{A}^t \hat{T} \vec{A} - \vec{A}^t \hat{V} \vec{A}, \quad (2.2)$$

where a vector notation  $\vec{A}$  has been adopted for the amplitudes  $A_i(t)$  and a superscript  $t$  indicates the transpose of a vector or matrix. The matrices  $\hat{T}$  and  $\hat{V}$  are the kinetic



and potential energy of the primitive plasmons. The application of the Euler-Lagrange equations gives,

$$[\hat{T}^t + \hat{T}] \frac{d^2}{dt^2} \vec{A} = -[\hat{V}^t + \hat{V}] \vec{A}. \quad (2.3)$$

The plasmon modes of the system are obtained as the eigenmodes of the corresponding secular determinant,

$$\det |\hat{V}^t + \hat{V} - \omega^2[\hat{T}^t + \hat{T}]| = 0. \quad (2.4)$$

Although the above procedure would work for an arbitrary complete set of primitive plasmon modes, the advantage of the plasmon hybridization method becomes apparent when the primitive plasmons are chosen to correspond to realistic excitations. For a composite nanostructure, the primitive plasmon modes can be chosen as the plasmon modes associated with the individual particles or surfaces. The kinetic energy then becomes diagonal and the potential energy will have a diagonal part  $\hat{V}_0$  representing the potential energy of the primitive plasmons and a nondiagonal part  $\hat{V}$  describing the Coulomb interaction between the different primitive plasmons. For example, for metallic nanoshells (Figure 2.1), the hybridizations are between surface plasmons localized on the inner surface of the shell (cavity plasmons) and plasmons associated with the outer surface (sphere plasmons). [2, 37] In the shell geometry, these primitive plasmons interact and form bonding and antibonding composite plasmons. The interaction between cavity and sphere plasmons is diagonal in multipolar indices. The bonding and antibonding plasmons of the nanoshell can therefore be

labeled by the same multipolar index as the plasmons in a solid sphere and a spherical cavity. The structure of the eigenvalue problem is then equivalent to the secular equation describing how electronic levels interact (hybridize) and shift in the presence of interactions.

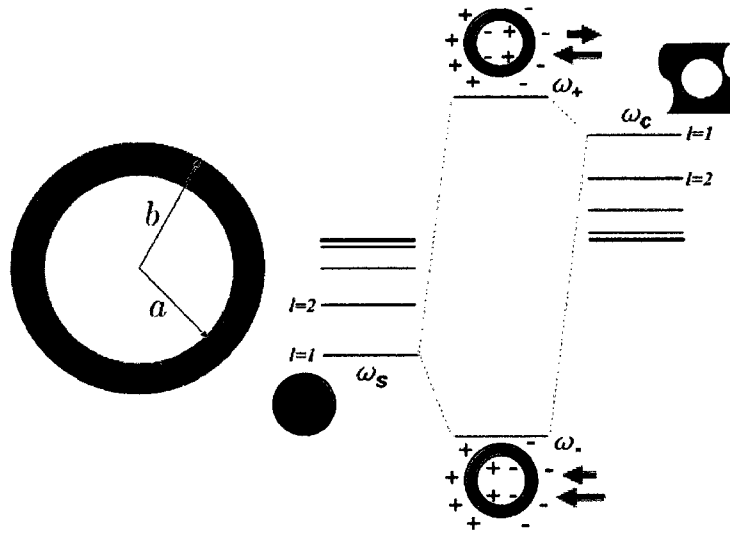


**Figure 2.1** Schematic picture showing the hybridizations between surface plasmons localized on the inner surface of the shell (cavity plasmons) and plasmons associated with the outer surface (sphere plasmons). These primitive plasmons interact only between same multipolar indices  $l$  and form bonding and antibonding nanoshell plasmons.

The plasmon hybridization method provides a very simple and intuitive approach for understanding the nature of the plasmon resonances in composite nanostructures. In quasi-static limit, when compared to the result from ab initio methods such as the Time Dependent Local Density Approximation (TDLDA) or the FDTD method, it has been shown to provide quantitative agreements. [34, 72, 64, 52, 73, 53, 74]. Mostly we focus on far-field optical properties of nanostructures such as the ener-

gies of the plasmons and the corresponding optical absorption spectra. The method can also be used to calculate near-field properties such as local electromagnetic field enhancements.

## 2.2 FDTD method

The FDTD method is an explicit time marching algorithm used to solve the partial differential Maxwell's equations on discretized Cartesian grids

$$\begin{aligned}\frac{\partial \vec{D}}{\partial t} &= \vec{\nabla} \times \vec{H} \\ \frac{\partial \vec{H}}{\partial t} &= -\frac{1}{\mu_0} \vec{\nabla} \times \vec{E}\end{aligned}\tag{2.5}$$

Electric fields and magnetic fields could be updated one after another numerically by central difference formulations, so the electromagnetic dynamics is simulated in a leapfrog manner. This "boot-strapping" algorithm was first proposed by Yee[75] that fields can be updated on an offset cell, Yee cell (Figure 2.2). [76, 77] However, people did not show much interest in this innovative idea because the computation domain is bounded and it was difficult in modeling an infinite space. In 1981, Mur successfully solved this problem by introducing absorbing boundary conditions,[78] which essentially makes the absorbing layer impedance matched to the dielectric permittivity of the medium in the computation space. Since then FDTD has been widely applied in engineering fields such as antenna array design,[79, 80] wireless communication,[81] biomedical research,[82] photonic crystal studies,[83, 84, 85]etc.

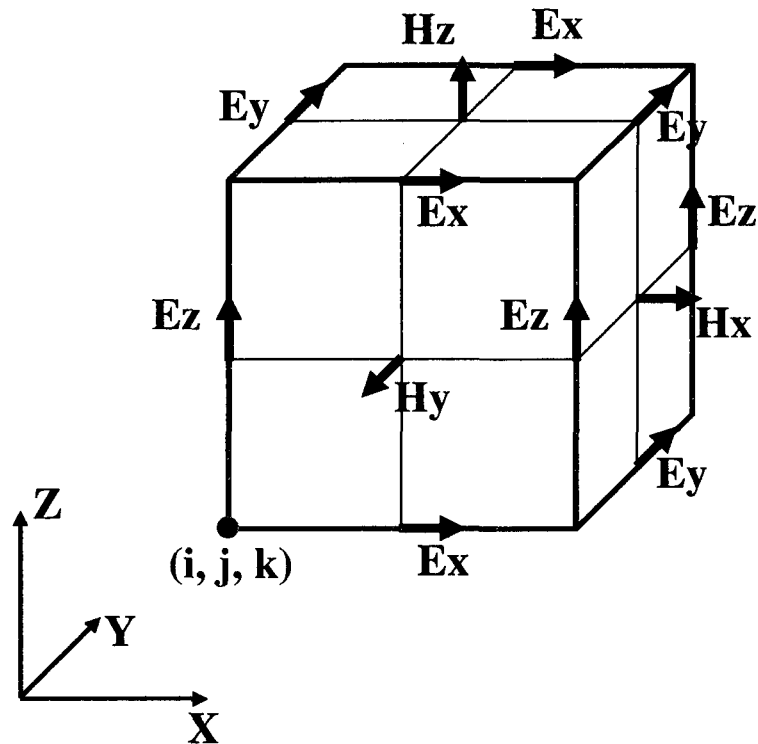


**Figure 2.2** Schematic illustration of the standard Yee cell used for FDTD. The vector components of the electric field and magnetic field are represented by blue and red arrows, respectively. Yee's algorithm is strictly applied in Cartesian coordinates.

FDTD algorithm possesses a great deal of advantages:

1. The method is conceptually simple. It is robust and well-understood.
2. It is working in the time domain versus the frequency domain so it provides an intuitive physical picture in real time. It allows wide frequency calculations in a single simulation. (See Appendix Figure A.1)
3. Depending on the specific application, FDTD usually implements faster than the alternatives.
4. It allows modeling arbitrary geometry and dispersive materials.
5. It is handy to predict near- and far-field optical properties of structures.
6. It is a fully retarded method so results are physical and in real situations.
7. Rapid improvements in computer technology has eliminated many of FDTD's inherent drawbacks, like a big appetite for memory. The natural parallelizability allows FDTD being implemented on distributed memory super computers (See Appendix Figure A.2, A.3, A.4).

The above advantages make FDTD a perfect simulation tool of investigating the plasmonic phenomena of nanoscale metallic structures. RiceFDTD is our homemade parallel computing software package (current version 3.0, developed by Yanpeng Wu in Nordlander's group at Rice University) developed for our basic plasmonic physics

research purposes, such as spectral analysis and electric field enhancement simulations of metallic nanostructures [86, 87, 74, 88, 89]. RiceFDTD provides efficient and accurate predictions with full retardation or damping effects in systems. It is parallelized using MPI-2 protocol and works on Beowulf clusters with hundreds of processors.

The bundle of PH and FDTD methods have provided us the enability and flexibility in studies of plasmonic properties of nanostructures. PH thoery and calculations can usually well interpret the plasmonic phenomena with an intuitive physical picture which FDTD sometimes might not be able to provide. PH method can be limited to applications for nanostructures with specific geometry, while FDTD can easily be applied on complex nanostructures.

# Chapter 3

## Nonconcentric Nanoshells (Nanoeggs)

### 3.1 Introduction

A new type of reduced-symmetry nanoparticle, the nanoshells with an offset core (nanoeggs), was developed and characterized using single particle optical spectroscopy.[90] Nanoeggs can be experimentally fabricated by using an anisotropic electroless plating technique (Figure 3.1A). All of the nanoeggs fabricated in this manner have the same orientation on the glass slides, with the point of contact with the glass substrate corresponding to the minimum in shell thickness for each nanoparticle. Increasing the time duration of the plating process results in an increase in the effective core offset of each nanoegg particle. Figure 3.1B and C shows typical transmission electron microscopy (TEM) images of a concentric nanoshell with homogenous shell thickness of 9 nm and a nanoegg with a core offset of 10 nm, respectively. In Figure 3.1D, the evolution of the extinction spectra of the oriented nanoegg films as a function of electroless plating time is plotted. These measurements were performed on nanoegg films by using normal incidence, unpolarized light. The spectral envelope of the plasmonic features shifts to shorter wavelengths as the electroless plating time increases. This trend is in good agreement with FDTD calculations (Figure 3.1E), which also show a spectral peak blueshift with increasing core offset, for the same orientation of core offset with respect to incident light. In these ensemble measurements, the plas-

mon peaks are significantly and asymmetrically broadened in comparison with the calculated spectra, because of the distribution in sizes and offsets in the fabricated nanostructures.

To theoretical study the plasmonic properties of nanoeggs, we model the nanoegg as a nanoshell with a nonconcentric core. In this reduced symmetry, the interactions between the primitive cavity and sphere plasmons are no longer diagonal in multipolar indices. Cavity and sphere plasmons of all multipolar indices interact (hybridize) and form bonding and antibonding nanoegg plasmons. The additional interaction results in stronger hybridization and large plasmon energy shifts and most importantly, in an admixture of optically active dipolar sphere plasmons into all nanoegg plasmons. Consequently several of the nanoegg plasmons can be excited by light also in the dipole limit. The nanoegg particle exhibits very large electromagnetic field enhancements on its thin shell side. This fact combined with the intrinsic tunability of a core-shell particle suggest that the nanoegg could be an attractive substrate for surface enhanced spectroscopies.

In this chapter, we show how the plasmon hybridization method, [2, 37] can be used to calculate the plasmonic properties of nanoshells with an offset core. We present an extensive investigation of the optical properties of nanoeggs as a function of offset parameter. We show that the plasmonic response of the nanoegg exhibits several distinct and tunable plasmon resonances. As the offset parameter increases,



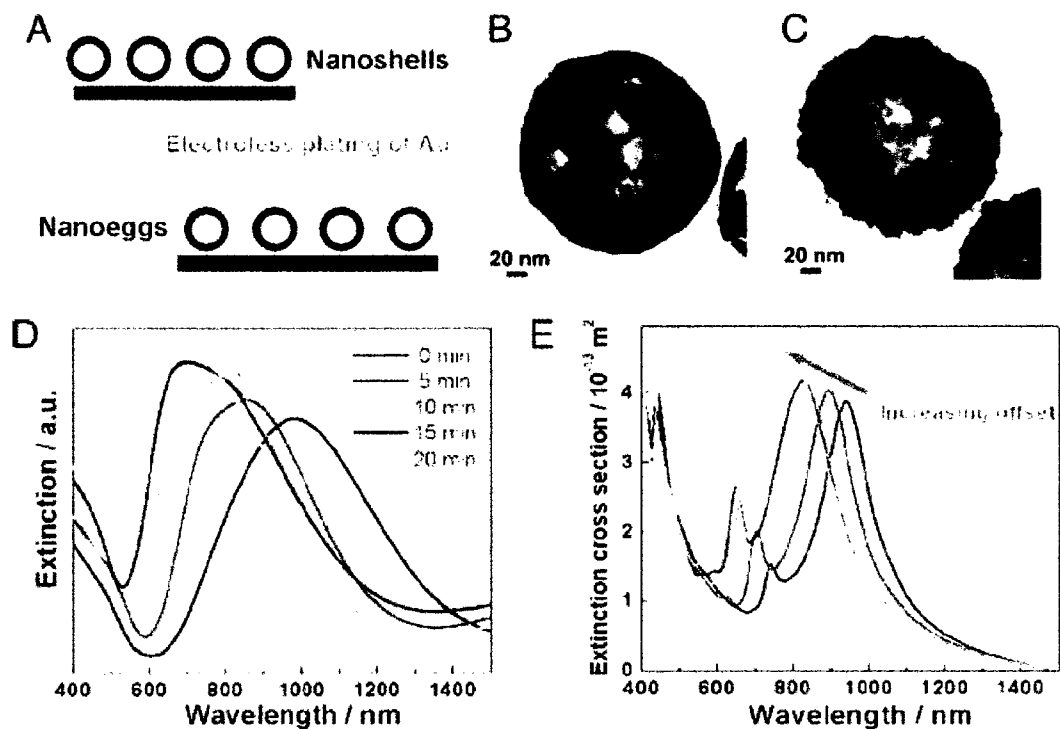


**Figure 3.1** Synthesis of nanoshells with a nonconcentric core. (A) Schematic of nanoegg fabrication. Monolayers of silicaCAu coreCshell nanoparticles were first immobilized on PVP-functionalized glass slides. The nanoshells used in this set of experiments are  $94 \pm 9$  nm in core radius and  $9 \pm 1$  nm in shell thickness. By controlling the reaction time, the offset extent can be controlled. Longer reaction time results in the formation of nanoeggs with larger offset cores. (B and C) TEM images of a nanoshell (B) and nanoegg (C). (D) Experimentally measured evolution of extinction spectra of oriented monolayer nanoegg film during metallization with unpolarized optical excitation at normal incidence. (E) Calculated normal incidence extinction spectra (FDTD) of reduced symmetry nanoparticles as a function of increasing offset. In this set of calculations, the nanoeggs have a silica core of 94 nm in radius. The thinnest part of the shell is 9 nm, and the thickest part of the shell is 9 nm for concentric nanoshell and varied to be 15, 21, 27, and 33 nm for nanoeggs.

the optical spectrum broadens and a multiple peak structure develops around the original dipolar plasmon resonance. For large offsets, the lowest energy plasmon resonances are strongly red-shifted compared to the concentric particle. We compare the results from plasmon hybridization with Finite-Difference Time-Domain (FDTD) simulations and find excellent agreement. We investigate the electromagnetic field enhancements for the nanoegg and show that they are much larger than for concentric nanoshells.

The organization of the chapter is as follows. In section II, we discuss how the plasmon hybridization method can be extended to treat a nanoshell with a nonconcentric core. In section III, we present the formalism and the results for optical absorption spectra. In section IV, we present FDTD simulations of the electromagnetic field enhancements. In section V, we show that in experiments, single-particle dark-field scattering spectra of a nanoegg clearly confirm our theoretical predictions.

### 3.2 Plasmon energies

As introduced in Chapter 2, for concentric nanoshells, the primitive modes are chosen as the plasmon modes associated with an individual solid sphere and a spherical cavity in a uniform bulk metal. For a nanoshell with an offset core,  $\eta$  can be written as:

$$\eta(r_S, \Omega_S; r_C, \Omega_C) = \sum_{l,m} \left[ \sqrt{\frac{a^{2l+1}}{l+1}} \dot{C}_{lm}(t) r_C^{-l-1} Y_{lm}(\Omega_C) \right]$$

$$+\sqrt{\frac{1}{16^{2l+1}}}\dot{S}_{lm}(t)r_S^l Y_{lm}(\Omega_S)], \quad (3.1)$$

where  $a$  and  $b$  are the inner and outer radius of the metallic shell, respectively. The variables  $C_{lm}$  and  $S_{lm}$  represent the time dependent amplitudes of the electron liquid deformations associated with the primitive cavity and solid sphere modes, respectively. The quantities  $l$  and  $m$  are the multipolar indices of the charge deformation. In the discussions below, we assume that the polar axis is oriented along the direction of the offset. Thus  $m = 0$  refers to plasmons polarized along the polar axis and  $m = \pm 1$  refer to plasmons polarized perpendicular to the polar axis. The coordinates  $(r_C, \Omega_C)$  and  $(r_S, \Omega_S)$  are spherical coordinates referring to coordinate systems centered on the cavity and the sphere, respectively, as illustrated in Figure 3.2. The relation between the coordinates on the different coordinate systems can be expressed using simple geometric relations.

The reason why we apply a two-center spherical coordinate system instead of a single spherical coordinate system is because it leads to a simplification in the calculation of the surface charges associated with the primitive nanoshell plasmons. The surface charge densities  $\sigma$  can be obtained directly from  $\eta$ , [37]

$$\frac{\partial \sigma}{\partial t} = n_0 e (\mathbf{n} \cdot \nabla \eta), \quad (3.2)$$

where the quantity  $n_0$  is the electron density of the conduction electrons and  $e$  is the electron charge. The vector  $\mathbf{n}$  denotes the normal vector on the geometric boundaries

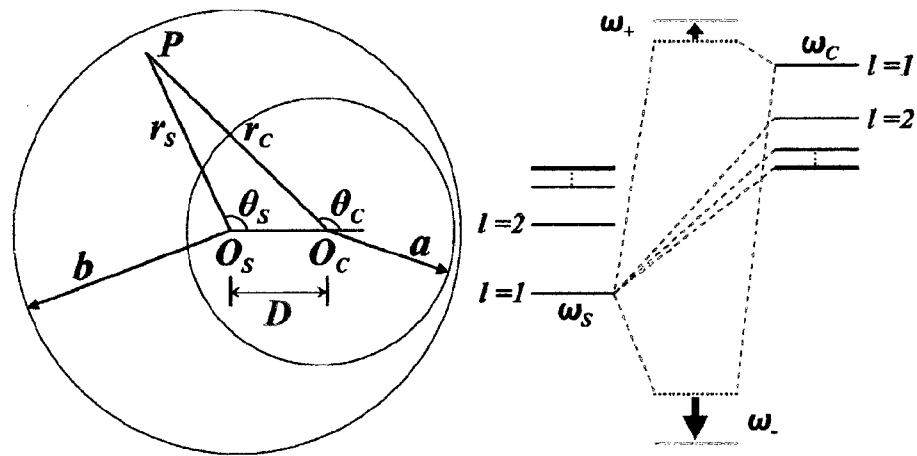


**Figure 3.2** Schematic picture illustrating the geometry and plasmon hybridization in a nanoshell with an offset core. The center of the cavity (radius  $a$ ) is offset a distance  $D$  from the center of the sphere (radius  $b$ ). The right portion illustrates how the primitive sphere plasmons,  $\omega_{S,l}$ , and the primitive cavity plasmons,  $\omega_{C,l}$ , interact and form bonding ( $\omega_-$ ) and antibonding ( $\omega_+$ ) hybridized plasmon modes. The green dashed lines illustrate the hybridization of sphere and cavity plasmons in a concentric nanoshell. For a nanoegg, a finite interaction (red dashed lines) exists between primitive plasmon modes of all multipolar order. This results in an extra redshift (red arrow) of the bonding  $l = 1$  nanoegg plasmon and a blueshift (blue arrow) of the antibonding  $l = 1$  nanoegg plasmon.

of the nanoegg, i.e., the inner and outer surfaces. Therefore, in Eq. (3.2) the dot product inside the parentheses includes two terms, one on the inner surface and the other on the outer surface. If a single spherical coordinates is used and the origin located at the center of the cavity for instance, the first term is straightforward because it can be addressed directly. However, the other term becomes more complicated and needs to be separated into radial and tangential components, since the normal vector on the outer surface is not in the radial direction from the origin. In a two-center coordinate system we can avoid this complication using the invariance,

$$\mathbf{n}_S \cdot \nabla_S \eta = \mathbf{n}_C \cdot \nabla_C \eta, \quad (3.3)$$

where the subscripts  $S$  and  $C$  refer to the coordinate system in which the same vector  $\mathbf{n}$  and gradient operator  $\nabla$  is expressed. Using this invariance, the dot products on the inner and outer surfaces can be calculated very simply in their respective coordinate systems. The surface charges  $\sigma$  can be written symmetrically in  $C_{lm}$  and  $S_{lm}$  terms, with one set of coefficients being the normal surface charges associated with the primitive plasmons in that particular coordinate system and the other set formulated as derivatives of functions expressed in the same coordinate system.

Eqs. (3.1), (3.2) and (3.3) lead to the following expression for the surface charge on the inner surface:

$$\sigma_C(t, \Omega_C) = -n_0 e \left. \frac{\partial \eta}{\partial r_C} \right|_{r_C=a} =$$

$$n_0 e \sum_{lm} \left[ \sqrt{\frac{l+1}{a^3}} C_{lm} Y_{lm}(\Omega_C) - \sqrt{\frac{1}{lb^{2l+1}}} S_{lm} \times \frac{\partial}{\partial r_C} \left[ r_S^l(r_C, \theta_C) Y_{lm}(\Omega_S(r_C, \theta_C)) \right] \right] \Big|_{r_C=a}, \quad (3.4)$$

and on the outer surface:

$$\sigma_S(t, \Omega_S) = n_0 e \frac{\partial \eta}{\partial r_S} \Big|_{r_S=b} = n_0 e \sum_{lm} \left[ \sqrt{\frac{l}{b^3}} S_{lm} Y_{lm}(\Omega_S) + \sqrt{\frac{a^{2l+1}}{l+1}} C_{lm} \times \frac{\partial}{\partial r_S} \left[ r_C^{-l-1}(r_S, \theta_S) Y_{lm}(\Omega_C(r_S, \theta_S)) \right] \right] \Big|_{r_S=b}. \quad (3.5)$$

The kinetic energy of this system can be calculated using the expression:

$$\begin{aligned} T &= \frac{1}{2} n_0 m_e \int \eta^* \nabla \eta \cdot d\mathbf{S} \\ &= \frac{m_e}{2e} \left[ \int a^2 \eta^* \dot{\sigma}_C \Big|_{r_C=a} d\Omega_C \right. \\ &\quad \left. + \int b^2 \eta^* \dot{\sigma}_S \Big|_{r_S=b} d\Omega_S \right], \end{aligned} \quad (3.6)$$

where  $m_e$  is the electron mass and the superscript \* denotes the complex conjugate.

The interaction is diagonal in azimuthal index,  $m$ , so in the following we will simply use  $m$  as a parameter. Introducing a vector notation for the primitive plasmon

amplitudes,

$$\mathbf{X}_m = \begin{pmatrix} C_{1m} \\ S_{1m} \\ \dots \\ C_{l_{max}m} \\ S_{l_{max}m} \end{pmatrix}, \quad (3.7)$$

where  $l_{max}$  denotes the highest order of multipolar primitive plasmons included, and the matrix notations introduced in the Appendix B, the kinetic energy for a specific  $m$  can be expressed as

$$T_m = \frac{1}{2} n_0 m_e (\dot{\mathbf{X}}_m^T \hat{T}_m \dot{\mathbf{X}}_m), \quad (3.8)$$

where the kinetic energy matrix  $\hat{T}_m$  is defined in the Appendix B. The superscript  $\mathbf{T}$  denotes the transpose of a vector or matrix.

The potential energy of the system can be calculated from,

$$\begin{aligned} V &= \frac{1}{2} \int \sigma^* \Phi dS \\ &= \frac{1}{2} \left[ \int a^2 \sigma_C^* \Phi \Big|_{r_C=a} d\Omega_C \right. \\ &\quad \left. + \int b^2 \sigma_S^* \Phi \Big|_{r_S=b} d\Omega_S \right], \end{aligned} \quad (3.9)$$

where the integration is over both the inner and outer surfaces and  $\Phi$  is the electrostatic potential from the primitive plasmons. Following the notations defined in the Appendix B, like for the kinetic energy, the potential energy can be expressed as a

quadratic form for a specific  $m$ :

$$V_m = \frac{1}{2} n_0 m_e (\mathbf{X}_m^T \hat{V}_m \mathbf{X}_m), \quad (3.10)$$

where the potential energy matrix  $\hat{V}_m$  is defined in the Appendix B. For  $D = 0$ , both  $\hat{T}_m$  and  $\hat{V}_m$  are block diagonal matrices where the interaction only exist between primitive plasmons of the same multipolar  $l$ . For finite  $D$ , off-diagonal components appear representing the hybridization of primitive plasmons of different multipolar orders.

The application of the Euler-Lagrange equations to the nanoegg Lagrangian gives,

$$\omega^2 [\hat{T}_m^T + \hat{T}_m] \boldsymbol{\nu} = [\hat{V}_m^T + \hat{V}_m] \boldsymbol{\nu}, \quad (3.11)$$

where the solutions for  $\omega$  are the energies for plasmon modes of azimuthal symmetry  $m$  of the system.

For small nanoparticles, an incident light wave represents a dipole-excitation and couples most strongly to the dipolar plasmons,  $l = 1$ . For this reason, we will focus our investigation on the parallel polarization  $m = 0$  and perpendicular polarization  $m = \pm 1$ . The nanoshells we study are gold, with the inner radius 8 nm and outer radius 10 nm. The experimentally synthesized nanoeggs consist of a thin layer of gold grown around a core consisting of silica. The inclusion of dielectric backgrounds in the plasmon hybridization method is straightforward[73] but would lead to a less transparent mathematical formalism. For this reason, we will model the nanoeggs



with a vacuum core surrounded by a metal with a renormalized electron density  $n_0$  corresponding to a bulk plasmon frequency of  $\omega_B = \sqrt{4\pi n_0 e^2 / m_e} = 4.6$  eV. This electron density corresponds to the experimentally observed value of 2.6 eV for the dipolar solid gold sphere plasmon resonance and effectively reproduce the tunability of the plasmon resonances of a real nanoshell over a wide range of aspect ratios.

To evaluate the plasmon energies, in principle all multipolar orders of the primitive plasmons should be included. In practice, we truncate this infinite summation at  $l_{max}$ , which depends on the size of the offset distance. In the calculations presented below we use an  $l_{max} = 50$  which has been verified to be sufficient for convergence.

In Figure 3.3, we show the energies of the hybridized plasmon modes for a non-concentric nanoshell as a function of offset parameter,  $D$ . The figure only shows the plasmon resonances originating from the  $l = 1 - 30$  primitive plasmons. The lower branch of curves in each panel represents the bonding nanoshell plasmons and the upper branch represents the antibonding modes. For zero offset  $D = 0$ , the plasmons can be classified by their multipolar index  $l$ . As the offset increases, primitive plasmons of different  $l$  mix resulting in nanoegg plasmons containing primitive plasmons of all multipolar orders. We will refer to the nanoegg plasmons using the multipolar index  $l$  to which they correspond in the limit of  $D = 0$ .

The figure shows a significant redshift of the low-energy bonding modes and a weaker but appreciable blue shift of the high-energy antibonding modes with increas-

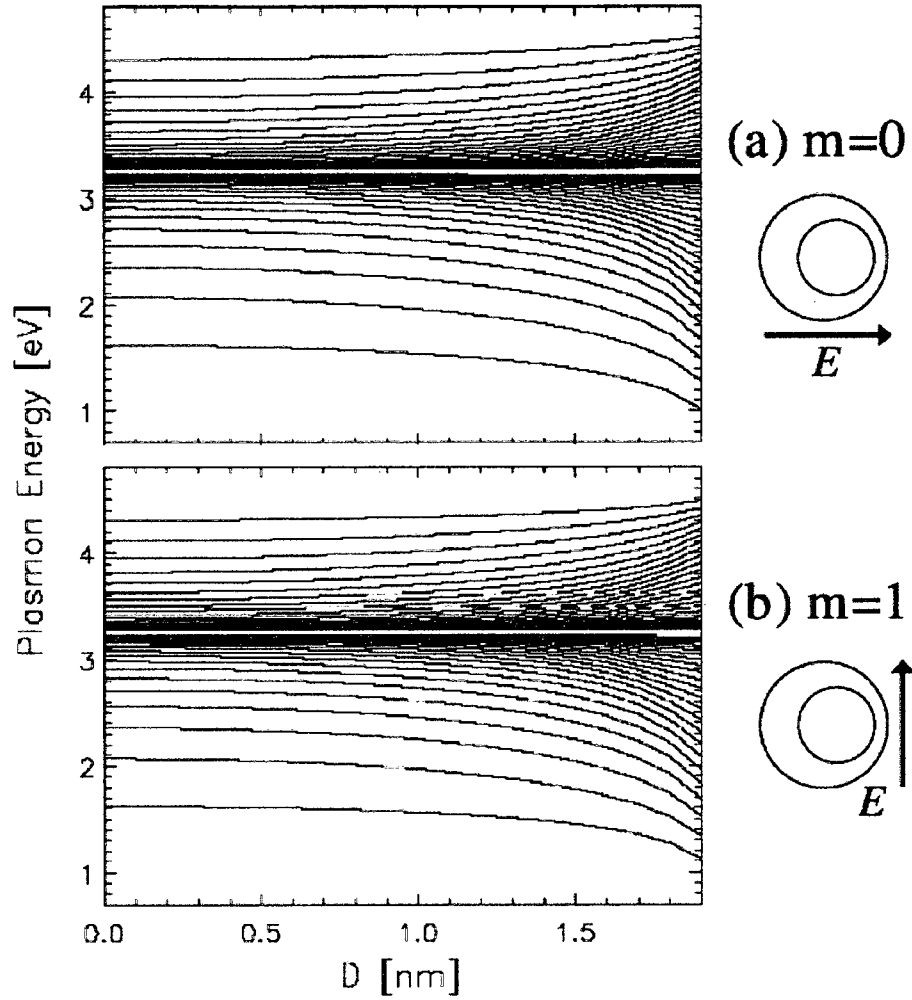


**Figure 3.3** Calculated plasmon energies of a nanoegg as a function of the offset  $D$ . The inner radius of the shell is 8 nm and the outer radius is 10 nm. The electron density of the shell corresponds to gold with a bulk plasmon energy of  $\omega_B = 4.60$  eV. The core is assumed to be vacuum. Panel (a) shows parallel polarization ( $m = 0$ ), and panel (b) shows perpendicular polarization ( $m = 1$ ). The curves include the bonding (lower branch) and antibonding nanoshell plasmons (upper branch) only for  $l = 1 - 30$ , resulting in the thin white horizontal strip around the surface plasmon energy ( $\omega_{SP} = \omega_B / \sqrt{2} \sim 3.25$  eV). The lowest and highest lines correspond to the bonding and antibonding  $l = 1$  plasmons, respectively.

ing offset distance. For small  $D$ , the energies of the hybridized plasmons vary only weakly with  $D$ . When the offset becomes larger, the energies depend very strongly on  $D$ . The effect is stronger for the low  $l$  plasmons because the interaction between primitive sphere and cavity plasmons decreases strongly with multipolar index  $l$ . For  $m = 0$  when  $D = 1.9$  nm, the redshift of the bonding  $l = 1$  nanoshell plasmon is quite large,  $\Delta E \sim 0.60$  eV. However, the largest redshift of plasmons occurs for the  $l = 5$  mode ( $\Delta E \sim 0.89$  eV). It can be understood by noting that energies of higher  $l$  modes are spaced closer together, leading to a stronger hybridization. This effect competes with the fact that the interaction decreases rapidly with increasing  $l$ , resulting in maximum shifts for intermediate  $l$ . The reason why the antibonding plasmons are less sensitive to the offset  $D$  is that they are primarily composed of primitive cavity plasmons and thus possess a smaller multipolar moment than the primitive sphere plasmons. The blue shift of the antibonding  $l = 1$ ,  $m = 0$  mode for  $D = 1.9$  nm is only  $\Delta E \sim 0.21$  eV.

The figure also shows that the orientation dependence of the plasmons is remarkably small. This is very different from the orientation dependence of nanoparticle dimer plasmons.[64, 86, 73] For nanoeggs, the plasmons polarized parallel to the polar axis are only slightly more shifted than the plasmons with perpendicular polarization. The orientation dependence of the hybridized plasmons is caused by the anisotropies of the multipolar interactions between the primitive plasmons.

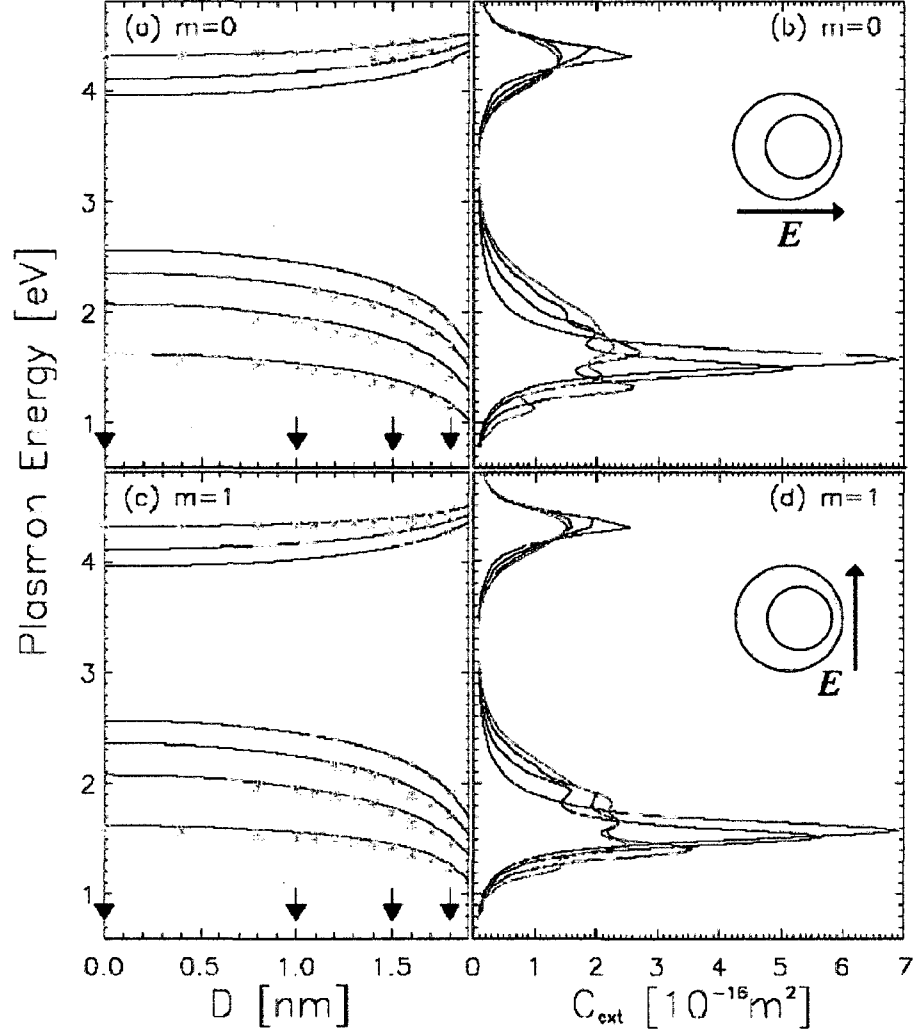


**Figure 3.4** Comparison of plasmon energies obtained from the FDTD extinction spectra and plasmon hybridization for different offset parameters  $D$  for the same nanoegg as in Figure 3.3. The upper panels refer to  $m = 0$  and the lower panels are for  $m = 1$ . The right panels show the FDTD extinction cross section calculated using a Drude dielectric function with a damping of  $\delta = 0.2$  eV. The solid lines in the left panels are the  $l = 1 - 4$  bonding and  $l = 1 - 3$  antibonding nanoegg plasmons from Figure 3.3. The orange stars are the plasmon resonances obtained from the FDTD extinction cross section. Panels (b) and (d) show the extinction spectra for  $D = 0$  nm (black),  $D = 1.0$  nm (blue),  $D = 1.5$  nm (green), and  $D = 1.8$  nm (red), as indicated by arrows of the same colors in panels (a) and (c).

Figure 3.4 shows a comparison of the plasmon energies obtained from plasmon hybridization method shown in Figure 3.3, with those obtained from the FDTD simulations. The plasmon energies correspond to distinct resonant peaks in the FDTD extinction spectra. The plasmon energies are obtained by fitting the extinction peaks with Lorentzians. The energies agree very well for all offsets considered. The retardation effects are negligible for the present small system, and the slight discrepancy is caused by numerical errors in the FDTD simulations [64, 76] and errors in the curve fitting. Panel (b) shows the calculated extinction cross section for  $m = 0$  at the four offsets indicated by arrows of the same colors in panel (a). For offset  $D = 0$  nm, two peaks are visible in the extinction spectrum. They are the bonding (at  $\sim 1.57$  eV) and antibonding (at  $\sim 4.31$  eV) dipolar nanoshell plasmons. The reason why the intensity of the antibonding peak is much smaller than the bonding resonance, is that the antibonding plasmon mode possesses a smaller dipole moment. For  $D = 1.0$  nm, the extinction spectrum shows two features in the lower energy part: a pronounced  $l = 1$  peak at around 1.49 eV and a weaker peak from the  $l = 2$  plasmon at around 1.91 eV. There is a very slight blue shift of the antibonding  $l = 1$  peak at  $\sim 4.33$  eV. The  $l = 2$  nanoegg plasmon mode is excited because of an admixture of the dipole-active primitive  $l = 1$  plasmons. The hybridization for this offset is still weak. For  $D = 1.5$  nm, where the hybridization between plasmon modes becomes stronger, the spectrum shows two distinct peaks at 1.33 eV ( $l = 1$ ) and at 1.68 eV ( $l = 2$ ) and two

weak shoulders at 1.97 eV ( $l = 3$ ) and at 2.20 eV ( $l = 4$ ). The high energy antibonding "hump" becomes broader and essentially splits into two peaks at 4.43 eV ( $l = 1$ ) and at around 4.29 eV ( $l = 2$ ). For the largest offset in FDTD simulations,  $D = 1.8$  nm, the spectrum exhibits several distinct peaks: at 1.14 eV ( $l = 1$ ), at 1.42 eV ( $l = 2$ ), at 1.68 eV ( $l = 3$ ), and at 1.88 eV ( $l = 4$ ). The antibonding  $l = 1 - 3$  modes lie very close in energy and form a featured structure around 4.3 eV. For this offset, the hybridization is very strong, and higher  $l$  modes contain a sizable admixture of the dipole-active primitive  $l = 1$  modes. The results for  $m = 1$  are very similar to the results for  $m = 0$  polarization.

### 3.3 Optical absorption

In the quasistatic limit, the nanoegg will couple to an external electromagnetic field through

$$\begin{aligned} V_{ext} &= \int \sigma^*(\mathbf{r})\Phi_{ext}(\mathbf{r})dS \\ &= E_0(t) \int r^{L+2}\sigma^*(\mathbf{r})Y_{LM}(\Omega)d\Omega, \end{aligned} \quad (3.12)$$

where we assume a pure multipole field,  $\Phi_{ext} = E_0(t)r^LY_{LM}(\Omega)$ , and  $E_0(t) = E_0e^{i\omega t}$ .

We use upper cases  $L$  and  $M$  to distinguish the multipolar and azimuthal indices of external field from the ones of the charge density  $\sigma$ , respectively.

The optical absorption spectrum  $f(\omega)$  is obtained from the optical polarizability

$\alpha(\omega)$  using

$$f(\omega) = \frac{\omega}{c} \text{Im}[\alpha(\omega + i\frac{\delta}{2})], \quad (3.13)$$

where  $\delta$  is the damping and corresponds to the FWHM of the peaks. The expression for the optical polarizability  $\alpha(\omega)$  is derived in the Appendix B. For a realistic description of the optical absorption,  $\delta$  should be determined from the frequency dependent imaginary part of the dielectric function.

In Figure 3.5, we compare the optical absorption spectra calculated using the plasmon hybridization method with the absorption spectra obtained using the FDTD method for different offsets and polarizations. The absorption spectra are very similar to the extinction spectra shown in the right panels of Figure 3.3 for the present small nanoparticle. The agreement between the two calculations is excellent for all four offsets and both polarizations. As discussed before, as the offset  $D$  increases, the higher order ( $l \geq 2$ ) nanoegg plasmon resonances become visible and redshift. For the largest offset  $D$ , so many of the bonding nanoegg plasmon modes are dipole active that the optical absorption spectrum appears strongly broadened. For parallel polarization of the incident light ( $m = 0$ ), the dipolar plasmon resonance shifts from  $\sim 770$  nm for  $D = 0$  nm to  $\sim 1060$  nm for  $D = 1.8$  nm. The structure around 288 nm represents excitation of antibonding  $l = 1 - 3$  nanoegg plasmon modes and would be strongly broadened if interband effects were included in  $\delta$ .

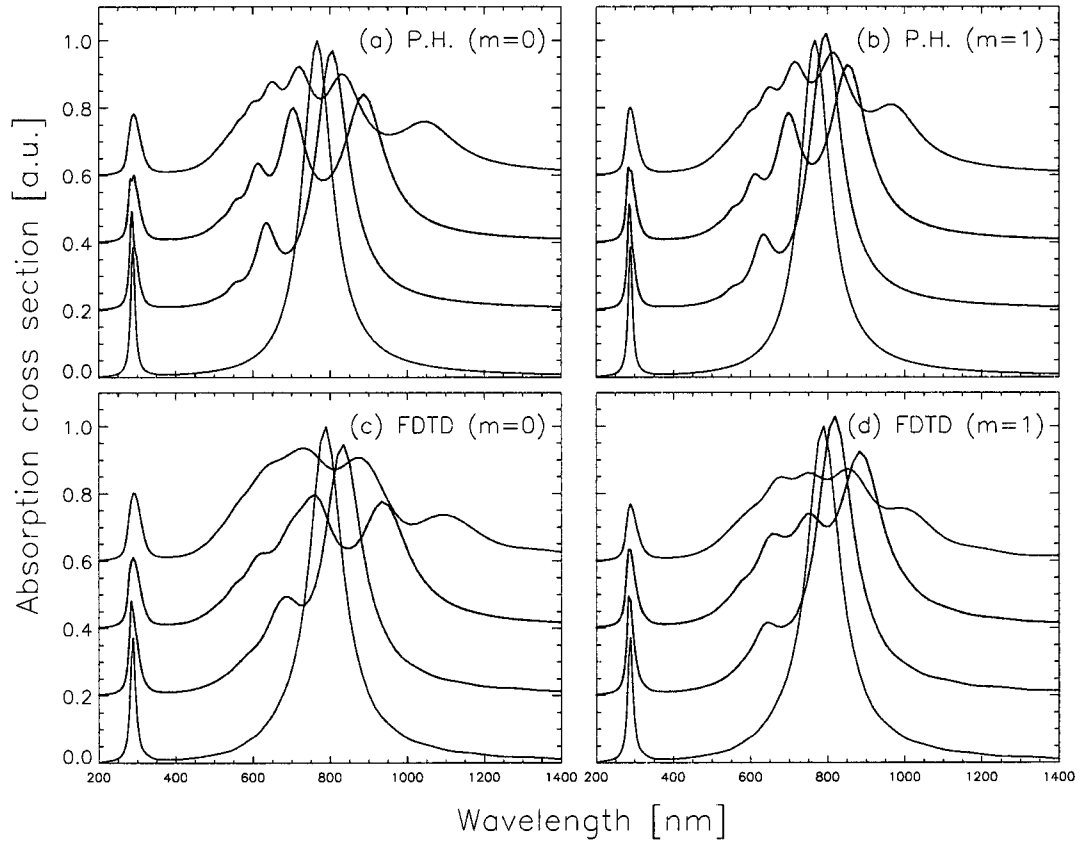


**Figure 3.5** Calculated optical absorption cross sections in arbitrary units for a nanoshell with an offset core for different offsets and polarizations. The optical absorption is calculated using a damping  $\delta = 0.2$  eV. The nanoshell is the same as used in Figure 3.3. Panels (a) and (c) are for  $m = 0$  and panels (b) and (d) are for  $m = 1$  polarization, respectively. The upper panels are obtained using plasmon hybridization method, and the lower panels show results from FDTD simulations. The offsets are  $D = 0$  nm (black),  $D = 1.0$  nm (blue),  $D = 1.5$  nm (green), and  $D = 1.8$  nm (red). The spectra have been offset vertically for clarity.



### 3.4 Electromagnetic field enhancements

In this section, we will investigate the electromagnetic field enhancements around nanoeggs for different wavelengths. The enhancement is defined as the ratio of the total electric field and the incident field at a particular spatial point. The enhancements are calculated using FDTD and a Drude dielectric function with the same damping  $\delta = 0.2$  eV as used elsewhere in this paper. This damping is about three times larger than the experimentally observed broadening ( $\delta = 0.069$  eV) resulting in underestimates of the actual field enhancements. [87]

In Figure 3.6, we show two-dimensional contour plots of electric field enhancements in a plane through the center of the nanoparticle for different wavelengths. The upper left panel shows the enhancements for excitation of the dipolar plasmon of a concentric nanoshell. The maximum enhancement in this case is 12.1. The three remaining panels show the enhancements for resonant excitation of the bonding  $l = 1 - 3$  plasmons for a nanoegg with  $D = 1.5$  nm. It can be seen that the nanoegg provides larger enhancements than the concentric nanoshell for all plasmon modes studied. The maximum enhancement 61 occurs for excitation of the  $l = 2$  plasmon. The enhancement for the  $l = 1$  mode is 26 and for the  $l = 3$  it is 20. The plasmon modes are strongly hybridized and none of the enhancement plots exhibits any particular multipolar symmetry. An analysis of the multipolar content of the nanoegg plasmons can be done straightforwardly using the plasmon hybridization method. The lowest

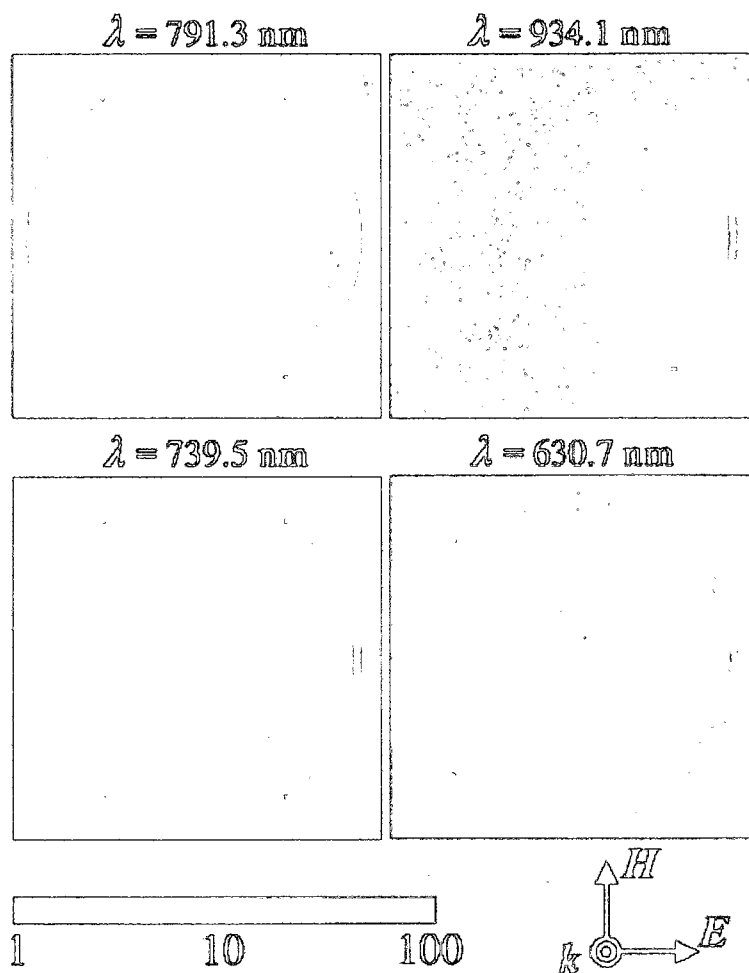


Figure 3.6 Two-dimensional contour plots of the local electric field enhancements for the concentric nanoshell (upper left panel) and a nanoegg with  $D = 1.5$  nm (the other three panels), excited with the parallel polarization at wavelengths corresponding to resonant excitation of the  $l = 1 - 3$  modes.  $\lambda = 791.3$  nm is the dipolar resonance wavelength of the concentric nanoshell and the maximum enhancement is 12.1. For the nonconcentric one, the wavelengths are 934.1 nm ( $l = 1$ ), 739.5 nm ( $l = 2$ ) and 630.7 nm ( $l = 3$ ), and the maximum enhancements are 26, 61 and 20, respectively.

multipolar primitive plasmon content of the  $l = 1$  nanoegg plasmon is (57% ( $l = 1$ ), 28% ( $l = 2$ ), 10% ( $l = 3$ ), 3% ( $l = 4$ ), 1% ( $l = 5$ ), ...). For the  $l = 2$  nanoegg plasmon the lowest multipolar content is (26%, 7%, 24%, 21%, 12%, ...) and for the  $l = 3$  nanoegg plasmon (9%, 25%, 5%, 4%, 14%, ...). The field enhancements increase with increasing offset  $D$ . For  $D = 1.8$  nm, the enhancements for the  $l = 1 - 3$  modes are 23, 99, and 37, respectively. The unique characteristics of nanoeggs providing large electromagnetic field enhancements on open surface areas over a broad range of wavelengths make these substrate particularly promising for SERS applications.

### 3.5 Single-particle dark-field scattering

To experimentally confirm our theoretical predictions and to further investigate the evolution of the plasmon energies of these reduced symmetry nanostructures, dark-field spectroscopic measurements were performed on isolated, individual, randomly oriented nanoeggs in reflection mode. [90] A sequence of single particle spectra is shown in Figure 3.7. The lowest spectrum is that of a single nanoshell, accompanied by representative spectra of reduced symmetry nanoparticles, each displaced vertically for clarity. The sequence of spectra shown with increasing vertical displacement corresponds to that of increasing offset  $D$ . The nanoshell bonding plasmon is seen at 730 nm and is accompanied by a much smaller broad peak at nominally 450 nm corresponding to the antibonding plasmon. For reduced symmetry nanoparticles, we see the onset and development of multi-peaked spectra of increasing complexity, accom-

panied by an overall redshift of the spectral envelope. Additionally, the antibonding plasmon peak becomes broader and eventually quite large, of similar magnitude as the accompanying lower energy modes in the nanoparticle spectrum. The peak positions and lineshapes vary significantly as the core offset changes. These single-particle spectra bear a striking qualitative resemblance to the theoretically calculated spectra shown in Figure 3.4 and 3.5. The presence of a dielectric substrate, the dark-field optical excitation and collection geometry, and phase-retardation effects[91] may affect the spectral widths observed for the experimentally fabricated nanoparticles relative to the theoretical spectra. Within experimental error, the fabricated nanoparticles have effective core offsets around  $D = 3.3$  nm and therefore correspond exactly to the regime where additional hybridized peaks should appear in the theoretical spectra. A direct analysis of the experimental spectra is needed and requires detailed modeling of the effect of the substrate, the effect of nanoparticle orientation, and the particular scattering geometry of the microscope.

### 3.6 Conclusion

We have shown that symmetry breaking can strongly modify the selection rules for the interaction of plasmon modes on an individual nanoparticle. For nanoshells with an offset core (nanoeggs), we have shown that the plasmon hybridization method provides a simple and intuitive understanding of their plasmonic structure. We show that the plasmons in the nanoegg are formed by hybridization of cavity and sphere plas-

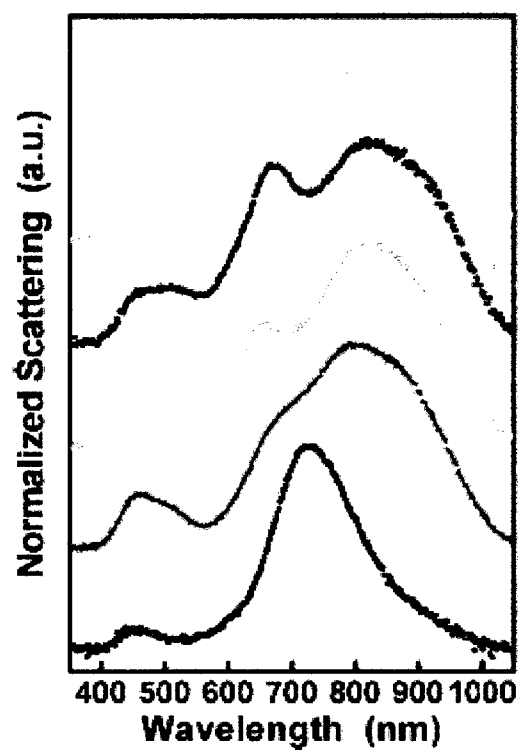


**Figure 3.7** Normalized single-particle dark-field scattering spectra of a nanoshell (black curve;  $[r_1, r_2] = [94, 103]$  nm) and four different reduced-symmetry nanoparticles (colored spectra). Nanoeggs were fabricated by electroless plating of Au onto the exposed surfaces of deposited nanoshells, to a maximum Au thickness of 25 nm. Selected unpolarized spectra of individual nanoparticles show that the fabrication process produces structures with a distribution of core offsets.

mons of all multipolar orders. For increasing offset between the core and the shell, the hybridization increases and leads to a strong redshift of the bonding plasmons. The hybridization also leads to an admixture of the primitive dipolar plasmons rendering many of the nanoegg plasmons dipole active. The results show a very small orientation dependence of the nanoegg plasmons. The plasmon energies and optical spectra obtained from the plasmon hybridization method are found to be in excellent agreement with the numerical FDTD results. Reduction in symmetry also is accompanied by an increased electromagnetic field enhancement on its external surface, located at the narrowest region of shell thickness. In contrast to many other geometries, here the region of maximum field enhancement is located on the open, exterior surface of an individual nanostructure and not within a narrow confined gap or junction. This approach may be useful in analyzing and understanding the near- and far-field optical response of other reduced-symmetry nanostructures of even greater complexity and, ultimately, in the design of various nanoparticle geometries with specific near-field optical properties.

# Chapter 4

## Nanoparticles near Dielectric Substrates

### 4.1 Introduction

The optical properties of metallic nanoparticles and their interactions with metallic [92, 93, 53, 94, 95, 96, 97, 98, 99] and dielectric substrates [100, 7, 101] are of considerable experimental and theoretical interests. The collective oscillations of the conduction electrons of a nanoparticle can result in characteristic Localized Surface Plasmon Resonances (LSPR) which dominate the optical spectra of metallic nanoparticles. These LSPR resonances are of utmost importance in many applications such as Surface Enhanced Raman Scattering (SERS).[102, 103, 104, 105, 106, 107, 108, 109, 110, 111, 112, 113]

The energies of LSPR can depend sensitively on the size and shape of the nanoparticle[114, 115, 116, 117, 118] and the dielectric properties of the surrounding media.[119] The latter property is the basis for LSPR sensing in which the presence of specific molecules on the surfaces of the nanoparticle can be detected from their screening-induced spectral shift of the LSPR.[120, 121, 122]

Significant shift of the LSPR can also result when nanoparticles are deposited on substrates. For metallic substrates, the interaction between the LSPR and the substrate plasmons can result in strongly redshifted hybridized plasmons containing admixtures of both the localized plasmon modes of the nanoparticle and the propa-

gating plasmon modes of the substrate. [52, 53, 54, 55, 56] These hybridized plasmon modes thus have mixed localized and propagating character and are fundamentally different from the original localized nanoparticle plasmon modes. For a nanoparticle near a dielectric surface, there are no substrate plasmons modes and the interaction results in a hybridization of the individual nanoparticle plasmon modes. This interaction can be simply understood using an image model, where the electromagnetic fields induced by a particular multipolar nanoparticle plasmon mode are screened by the substrate and acquire different multipolar components in the coordinate system centered on the nanoparticle. This screening thus mediates an interaction between multipolar plasmons of different order resulting in localized hybridized nanoparticle plasmons. For a nanoparticle embedded in a uniform dielectric, there is no such hybridization but only a redshift due to the dielectric screening.

In a recent study, a comprehensive investigation of the interaction of individual metallic nanoshells with dielectric substrates of different permittivities was performed.[101] The experiment revealed that the presence of the substrate lifts the degeneracy of the dipolar nanoshell modes. The dipolar mode oriented towards the surface was found to exhibit a significant redshift which increases with the permittivity of the substrate while the dipolar modes oriented parallel to the surface only showed negligible shifts. For substrate with a large dielectric permittivity such as ZnSe, the experiment also clearly showed the appearance of hybridized quadrupolar nanoshell modes in the sin-



gle particle scattering spectrum.

In this chapter, we present an extensive theoretical investigation of the interaction of metallic nanoparticles with dielectric surfaces. We show how the Finite-Difference Time-Domain (FDTD) method can be applied to describe this interaction and the resulting angular scattering cross section using finite slab models of the substrate. We investigate the shift of the LSPR resonances with nanoparticle-substrate separation and their dependence on the dielectric permittivity of the substrate. We also show that the degeneracy of the hybridized quadrupolar nanoparticle resonances are lifted and that for small nanoparticle-substrate separations, their spectral weight can be strongly enhanced due to the substrate induced intraparticle plasmon hybridization.

The organization of the chapter is as follows. In section II, we investigate the interaction of a metallic nanoparticle with a finite dielectric substrate and how the plasmon energies depend on the dimensions of the finite slab used to model the substrate. In section III, we discuss how an extended substrate can be described using a finite slab model embedded in an absorbing medium and how the differential scattering spectra appropriate for typical dark-field microscopy geometries can be calculated using the near-to-far field transformation. In section IV, we show a comparison with experiments and theoretical results using another numerical method - Finite Element Method (FEM).

## 4.2 Optical properties of a nanoshell near a dielectric slab

In this section we investigate the plasmonic interactions of a nanoshell with a finite dielectric slab. In the first subsection, we show how the symmetry breaking introduced by a substrate results in a lifting of the degeneracy of the dipolar and quadrupolar nanoparticle resonances and can result in intra nanoparticle hybridization of the plasmon resonances. In the second subsection we investigate how the energy of the hybridized plasmon resonances depend on the dimensions of the finite dielectric slab used to model the substrate.

The FDTD method provides efficient and accurate results for the numerical calculation of the optical properties of metallic nanostructures. The geometry in our study is illustrated in Figure 4.1. All the nanoshells modeled in this paper have  $R_1 = 74$  nm and  $R_2 = 80$  nm.[123] The core of nanoshells is assumed to be silica with a permittivity  $\epsilon_{core} = 2.04$ . For the metallic shell, a Drude dielectric function was used with parameters fitted to the experimental data for gold,[124] which has been shown to provide an accurate description of optical properties of gold for wavelengths larger than 500 nm.[87] The dielectric substrate was modeled as a finite block-shaped slab with lateral lengths  $L$  in the  $\hat{x}$  and  $\hat{y}$  directions and thickness  $T$  in the  $\hat{z}$  direction. In most applications below, the permittivity of the substrate will be assumed to be  $\epsilon_S = 6.5$  corresponding to ZnSe. The separation between the nanoshell and substrate is denoted  $d$ . The results for the finite slab model will also be compared to the results

for an infinite surface obtained using an approach described in section III.

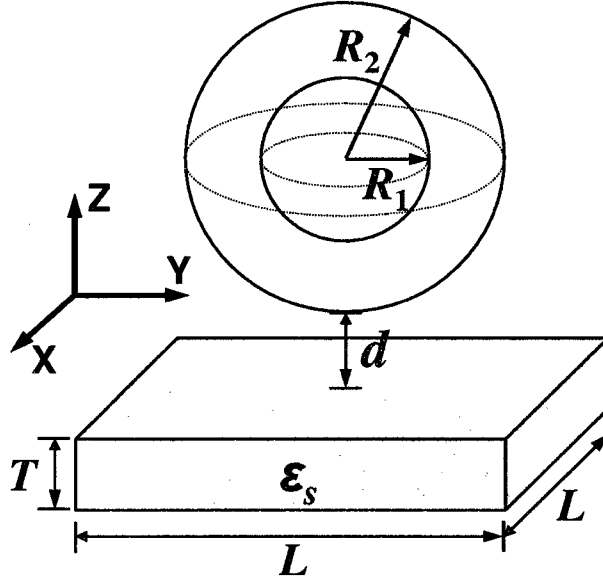


**Figure 4.1** Geometry and parameters of the nanoshell/finite slab model. The core of the gold nanoshell is silica  $\epsilon_{core} = 2.04$ . The finite slab of dielectric permittivity  $\epsilon_S$  has equal lateral lengths  $L$  in the  $\hat{x}$  and  $\hat{y}$  directions, and thickness  $T$  in the  $\hat{z}$  direction. The separation between the bottom of the nanoshell and the upper surface of the slab is  $d$ .

#### 4.2.1 Substrate induced symmetry breaking and hybridization

The effect of a dielectric surface on the plasmon resonances of a nearby nanoparticle can be understood using a simple image model. The plasmon induced charge density of the nanoparticle is screened by induced surface charges on the substrate. The magnitude of the substrate image charges depend on the permittivity of the substrate  $\epsilon_S$ , as  $(\epsilon_S - 1)/(\epsilon_S + 1)$ . This factor increases monotonously with  $\epsilon_S$  to 1 when  $\epsilon_S \rightarrow \infty$  representing a perfect image.

The plasmon modes of a spherical nanoparticle can be labeled by their multipolar

order  $(l, m)$  where  $m$  refers to the azimuthal orientation of the plasmon mode. For a plasmon mode of multipolar order  $l$ , the degeneracy is  $2l + 1$ . The presence of the dielectric substrate breaks the spherical symmetry of the nanoshell and lifts the degeneracies of their plasmon modes. Plasmon modes with charge densities close to the surface will couple stronger to the substrate than plasmon modes with charge densities located further from the substrate. This is illustrated for the bonding dipolar  $l = 1$  nanoshell modes in Figure 4.2a. With a dielectric substrate, the three-fold degenerate dipolar ( $l = 1, m = 0, \pm 1$ ) bonding nanoshell plasmon mode  $D_0$  splits into a nondegenerate  $D_1$  mode with a dipole moment perpendicular to the surface and a doubly degenerate  $D_2$  mode with dipole moments parallel to the substrate. The nanoparticle-substrate interaction for the  $D_1$  mode is much stronger than for the very weakly interacting  $D_2$  mode leading to a significant redshift for the  $D_1$  mode.[101]

For the present relatively large nanoshell, the incident light has a sufficient quadrupolar component that nanoshell quadrupolar modes can be excited. With a dielectric surface, the spherical symmetry of nanoshell is reduced to a rotational symmetry about the sphere center axis which is normal to the surface. The azimuthal index  $m$  is determined by the different polarizations of incident field with respect to the axis of symmetry. Thus, as illustrated in Figure 4.2b, the five-fold degenerate quadrupolar ( $l = 2, m = 0, \pm 1, \pm 2$ ) bonding nanoshell mode  $Q_0$  splits into three distinct modes: a nondegenerate  $Q_1$  mode for p-polarized excitation, a doubly degenerate  $Q_2$  mode for

45-degree polarization, and a doubly degenerate  $Q_3$  mode for s-polarized excitation. According to the charge density distribution of the quadrupolar mode ( $Q_0$ ) for an individual nanoshell, one would expect the  $Q_2$  mode to exhibit the strongest interaction with the substrate due to larger local charge density near the surface. The  $Q_1$  mode exhibits an intermediate interaction strength and the  $Q_3$  mode interacts only very weakly.

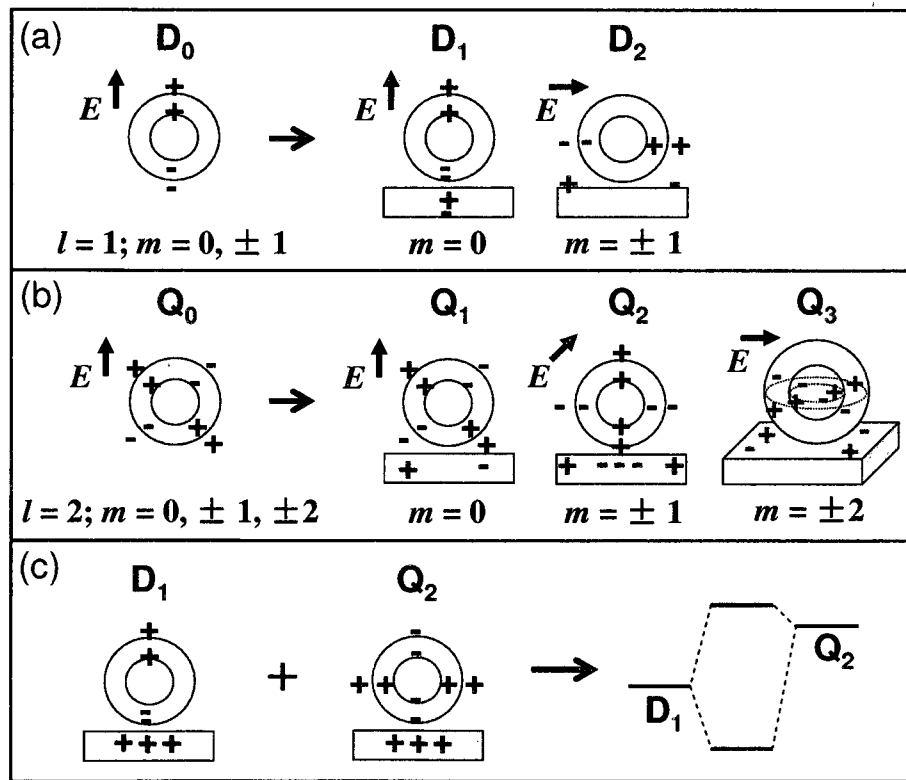


**Figure 4.2** Schematic illustrating the dipolar (a) and quadrupolar (b) plasmon bonding modes of a metallic nanoshell on a dielectric substrate, and the intra-nanoparticle plasmon hybridization (c) near a dielectric surface. The three-fold degenerate dipolar bonding mode  $D_0$  splits into a  $D_1$  and two  $D_2$  modes. The five-fold degenerate quadrupolar bonding mode  $Q_0$  splits into a  $Q_1$  mode, two  $Q_2$  modes and two  $Q_3$  modes. The black  $+/-$  signs represent the free surface charges on the nanoshell, and the red  $+/-$  signs represent the induced substrate charges.

The symmetry breaking introduced by the substrate also results in a hybridization of the nanoparticle plasmon resonances. Mathematically this can be understood from the fact that the substrate-induced fields across the nanoshell will contain multipolar components of all orders. The substrate-induced fields thus introduce an interaction between nanoparticle plasmons of different multipolar orders and lead to hybridization of the nanoparticle plasmon resonances. Such a hybridization would not be present for the individual nanoparticle in an isotropic medium. A simple physical model for this hybridization is illustrated in Figure 4.2c for the  $D_1$  and  $Q_2$  modes. Both these plasmon modes induce similar substrate surface charge on the substrate side of the junction. Thus the substrate mediate an interaction resulting in a bonding mode of  $D_1$  character and an antibonding mode of  $Q_2$  character. Since the antibonding mode also will contain a dipolar component, the spectral intensity of this mode will be enhanced compared to an individual nanoshell. This hybridization is similar to the plasmon hybridization in metallic nanoparticle dimers, which is sensitive to polarizations of incident light, particle-particle separation and surrounding medium.[125]

In Figure 4.3, extinction cross section spectra of the nanoshell-substrate system are shown for different polarizations. The extinction for a nanoshell in vacuum (black) shows the  $D_0$  and  $Q_0$  resonances at 891.8 nm and 711.9 nm, respectively. With a dielectric substrate, the  $D_1$  mode shifts to 1014.0 nm and the  $D_2$  mode to 938.0 nm. As discussed above, the  $D_1$  exhibit larger redshift since this mode interacts stronger

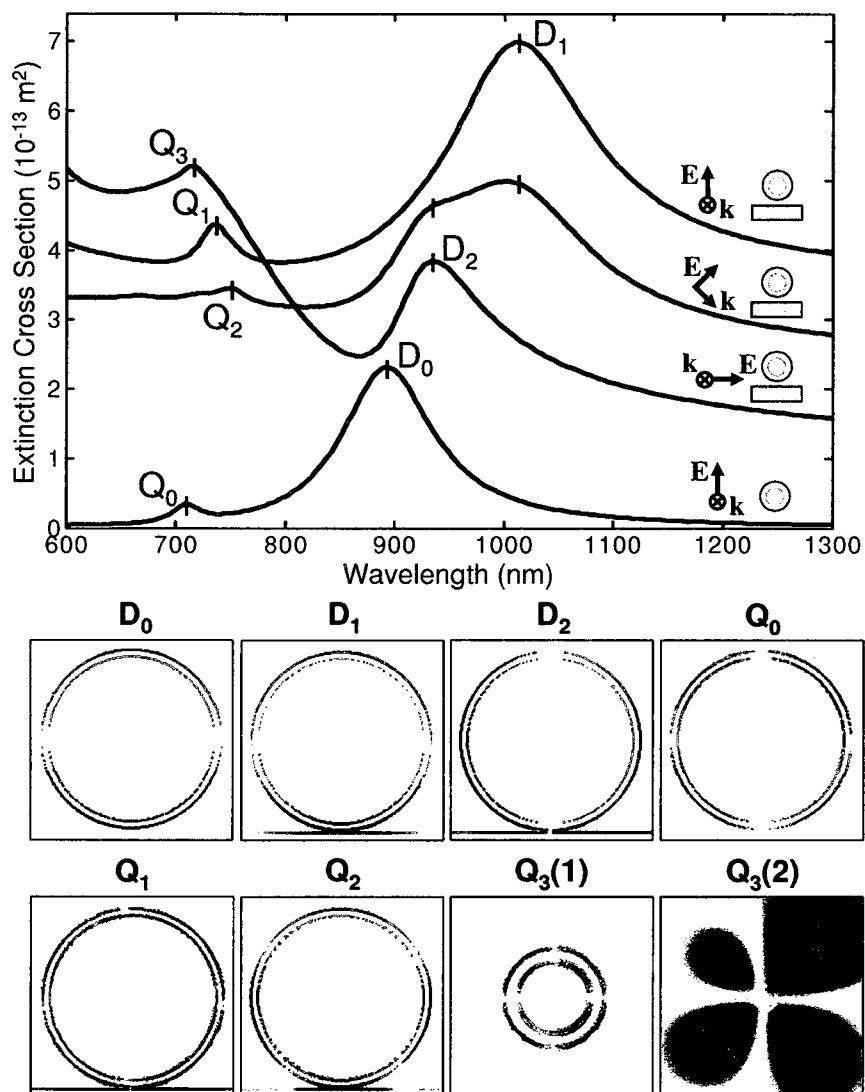


**Figure 4.3** Upper panel: extinction cross section spectra of the gold nanoshell/dielectric slab structure for different polarizations of the incident field: p-polarized (red), 45 degree-polarized (green), and s-polarized (blue). The individual nanoshell spectrum (black) is shown for comparison. The slab parameters are  $L=320$  nm,  $T=80$  nm,  $d=2$  nm, and  $\epsilon_S=6.5$ . The contour plots show the charge distributions for the different modes apparent in the spectra. For  $Q_3(1)$ , the contour plane is the top view of  $xy$  plane at 15 nm from the slab surface. For  $Q_3(2)$ , the contour plane is the upper surface of the slab. For the other panels, the contour plane is the  $xz$  plane through the center of the nanoshell.

with the substrate. The spectra show that the intensity of the  $D_1$  resonance is larger than for the  $D_2$  mode. The spectral intensity of a mode is proportional to the square of its dynamical dipole moment. For the  $D_1$  mode, the screening from the substrate provides a dipole oriented in the same direction as the nanoparticle dipole and thus increase the effective dipole moment of the mode. For the  $D_2$  mode, the substrate screening is equivalent to a dipole oriented in the opposite direction and thus results in a lower effective dipole moment and excitation probability. For 45-degree polarization, both the  $D_1$  and  $D_2$  modes appear in the spectrum. For the quadrupolar modes, three resonances show up at 737.2 nm ( $Q_1$ ), 752.0 nm ( $Q_2$ ), and 716.3 nm ( $Q_3$ ) for the respective polarizations. The  $Q_2$  mode has the lowest resonance frequency confirming that this mode exhibits the largest interaction with the substrate. The relative intensities of the quadrupolar modes compared to the dipolar modes are enhanced on the substrate because of the substrate-induced hybridization of the nanoparticle quadrupolar and dipolar modes as illustrated in Figure 4.2c. The intensity enhancement of the  $Q_2$  mode is somewhat obscured by the simultaneous excitation of also the  $Q_1$  and  $Q_3$  modes for 45-degree polarization. We will show in Section III that dark-field scattering calculation can effectively improve the resolution of spectra. Detailed discussion about the relative height of quadrupoles will be conducted as well. In the lower part of Figure 4.3, the surface charge distributions for the dipolar and quadrupolar modes are plotted and clearly confirm the symmetry



classification discussed in Figure 4.2a-b.

In addition to the hybridized nanoshell resonances, the spectra in Figure 4.3 show a significant broad spectral feature for short wavelengths, particularly for s-polarized excitation. This is caused by Fabry-Perot (FP) resonances in a finite dielectric slab. When the width or thickness of the slab is equal to an integer number of half wavelengths of the incident light in the substrate medium, such FP resonances can significantly influence the extinction. The energy of these FP resonances depend strongly on the polarization of the incident light and the dimensions of the slab but are always sufficiently broad that the much narrower quadrupolar resonances can be identified unambiguously.

#### 4.2.2 Finite slab effects

When modeling the nanoparticle substrate interaction using finite slabs, it is important to use a sufficiently large slab that the substrate induced screening is properly accounted for. In addition, for a finite slab, edge effects can influence the the amount and spatial distribution of the induced charges on substrate surfaces, and result in artificial shifts and hybridization of the plasmon modes. In this subsection we study how the dimensions of the slab affect the nanoparticle plasmon resonances.

In Figure 4.4, we plot the energies of the dipolar and quadrupolar nanoshell plasmon resonances for different slab dimensions  $L$  and  $T$ . We also include exact results (red lines) for a nanoshell near an infinite substrate obtained using the method de-

scribed in section III. For a fixed slab thickness  $T$  when the lateral width of the slab  $L$  is smaller than the diameter of the nanoshell, the image charges are "squeezed" in the  $\hat{x}$  and  $\hat{y}$  directions, resulting in a weaker nanoparticle substrate interaction. As  $L$  increases, all the plasmon modes exhibit redshifts. When  $L$  is larger than 320 nm, twice as large as the diameter of the nanoshell, all the modes have converged to the exact solutions. We note that the quadrupolar modes converge faster than the dipolar modes, which can be understood qualitatively because the quadrupole-quadrupole interaction decays faster as  $1/r^5$  instead of  $1/r^3$  for the dipole-dipole interaction. For a slab of fixed lateral width  $L$  but varying thickness  $T$ , the situation is similar. As the thickness  $T$  is increased, the energies of the plasmon modes redshift monotonously and converge at a thickness approximately equal to the diameter of the nanoparticle. The reason why convergence is reached faster in  $T$  is that the electromagnetic field across the nanoshell originating from the surface charges on the opposite side of the slab are screened and play a less important role for the plasmon energies.

These convergence studies are not restricted only to nanoshell particles interacting with dielectric slabs but apply for any plasmonic nanoparticle of an overall diameter  $D$ . The minimum dimensions of the slab required for converged plasmon energies are  $T \geq D$  and  $L \geq 2D$ . This finding agrees with previous DDA studies using finite slab models of different shapes.[100]

The results presented in this subsection shows that finite slab models can be

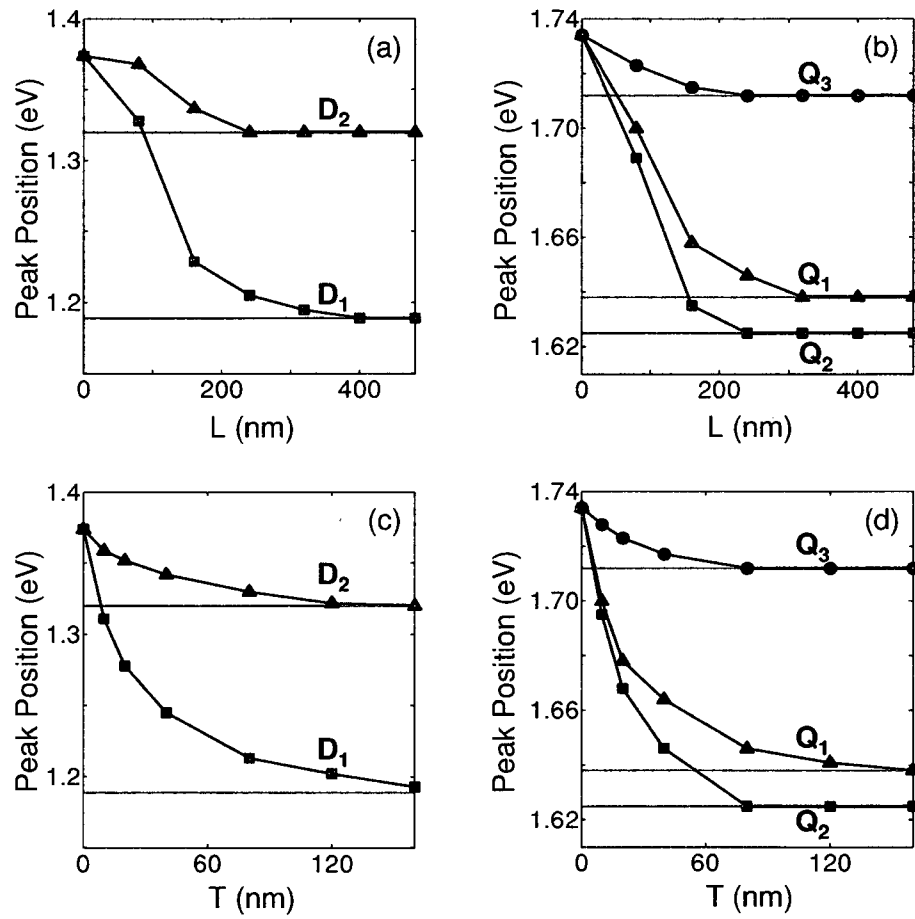


**Figure 4.4** Effect of substrate size on the energy of the gold nanoshell plasmon resonances. Dependence on  $L$  for  $T=160$  nm (panel (a) and (b)) and dependence on  $T$  for  $L=320$  nm (panel (c) and (d)). Red lines are the exact solutions. The slab parameters are  $\epsilon_S=6.5$  and  $d=2$  nm.

used to calculate the shifts of nanoparticle plasmon energies caused by substrate interactions due to the localized nature of the induced surface charges. However, the extinction spectra obtained from finite slab models can be strongly distorted by FP resonances which would not be present for an infinite substrate. Below in section III, we will show how the FP resonances can be eliminated by embedding the finite slab in an absorbing medium.

### 4.2.3 Effect of nanoparticle-substrate separation

As for metallic nanoparticle dimers, the influence of a dielectric surface is expected to decrease with increased nanoshell-substrate gap distance  $d$ . In Figure 4.5, we show the  $d$  dependence of the energies of the dipolar and quadrupolar nanoshell plasmon modes outside a dielectric substrate. For decreasing separation  $d$ , the plasmon modes exhibit monotonous redshift. The redshifts of the dipolar  $D_1$  and quadrupolar  $Q_1$  and  $Q_2$  modes are much larger than the shifts of the  $D_2$  and  $Q_3$  and are consistent with the spatial distributions of the plasmon induced surface charges in Figure 4.2a-b. For separations  $d$  larger than the diameter of the nanoshell  $2R_2=160$  nm the plasmon modes converge towards the degenerate plasmon modes of a nanoshell in vacuum. This result is consistent with the previous observations of the distance dependent nanosphere/nanoshell dimers plasmon resonances[125] and the separation dependent plasmon resonances of nanoparticle clusters influenced by a metallic substrate,[55] showing that the interaction with a substrate is negligible when  $d$  is larger than the

size of nanoparticles.

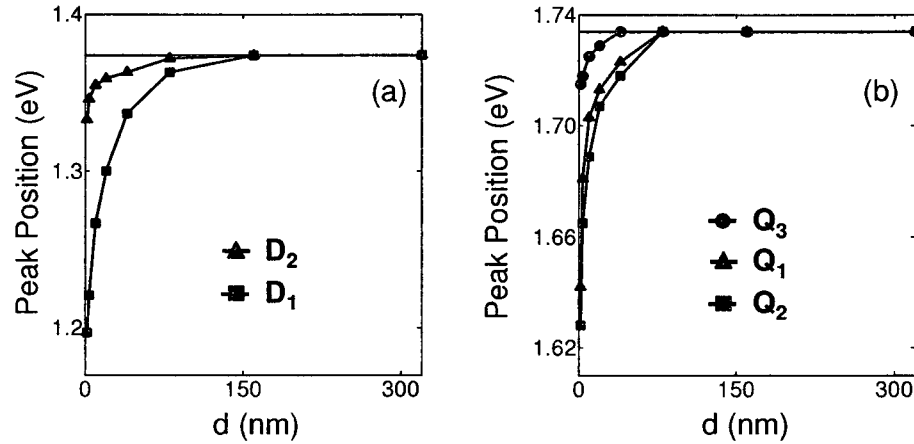


**Figure 4.5** Effect of nanoparticle-substrate separation  $d$  on the energy of the dipolar (a) and quadrupolar (b) nanoshell plasmon resonances. The red lines are the degenerate dipolar and quadrupolar modes of a nanoshell in vacuum. The dielectric permittivity of the substrate is  $\epsilon_S=6.5$ .

#### 4.2.4 Effect of substrate permittivity

In Figure 4.6 we show how the energies of the nanoshell plasmon modes dependent on the dielectric permittivity of the substrate  $\epsilon_S$ . The plasmon energies redshift monotonously with increasing  $\epsilon_S$ . The reason for this is that the magnitude of the image charges,  $(\epsilon_S - 1)/(\epsilon_S + 1)$ , increases with increasing  $\epsilon_S$ . and converges to 1 for large  $\epsilon_S$ . For small  $\epsilon_S$ , the redshifts and energy splitting of the dipolar modes ( $D_1$  and  $D_2$ ) are approximately linear in  $\epsilon_S$ . [101] For  $\epsilon_S$  larger than 7, the redshift of the modes begins to saturate and the energy splitting becomes constant.

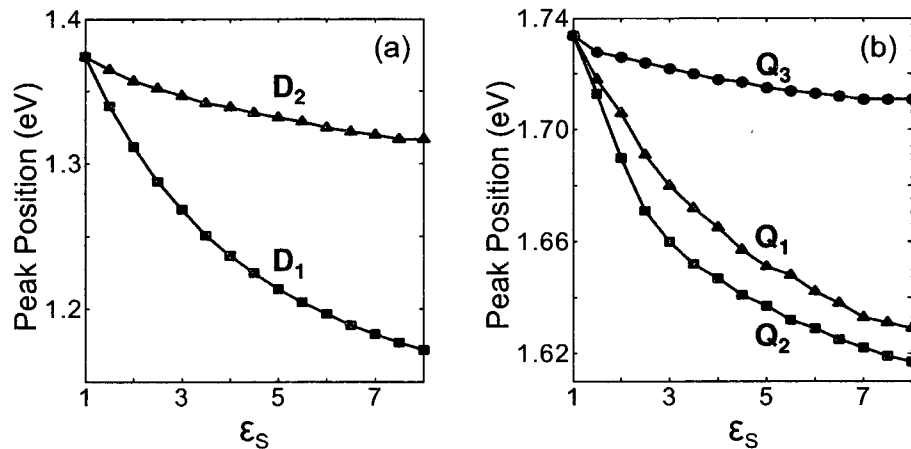


**Figure 4.6** Energies of the dipolar (a) and quadrupolar (b) nanoshell plasmon modes as a function of dielectric permittivity of the substrate  $\epsilon_S$ . The nanoshell-substrate separation is  $d = 2$  nm.

### 4.3 Dark-field Scattering

The dark-field microspectroscopy is widely employed in experiments to measure the scattering spectrum of individual nanoparticles.[90, 125, 101] In typical instruments, light is incident on an individual nanoparticle and the light scattered by the nanoparticle is collected within a cone of opening angle  $\theta_{obj}$  defined by the Numerical Aperture (NA),  $NA = \sin\theta_{obj}$  of the microscope objective.

In Figure 4.7 we show examples of how the extinction and differential scattering cross sections appropriate for dark-field spectroscopy can be calculated using the FDTD algorithm. A modulated Gaussian pulse (black arrows) is inserted into the computational domain using the Total-Field/Scattered-Field (TFSF) technique.[126] A virtual rectangular surface (red box) referred to as a Discrete Fourier Transfer (DFT) monitor is defined for the collection of the near-zone scattered fields. These

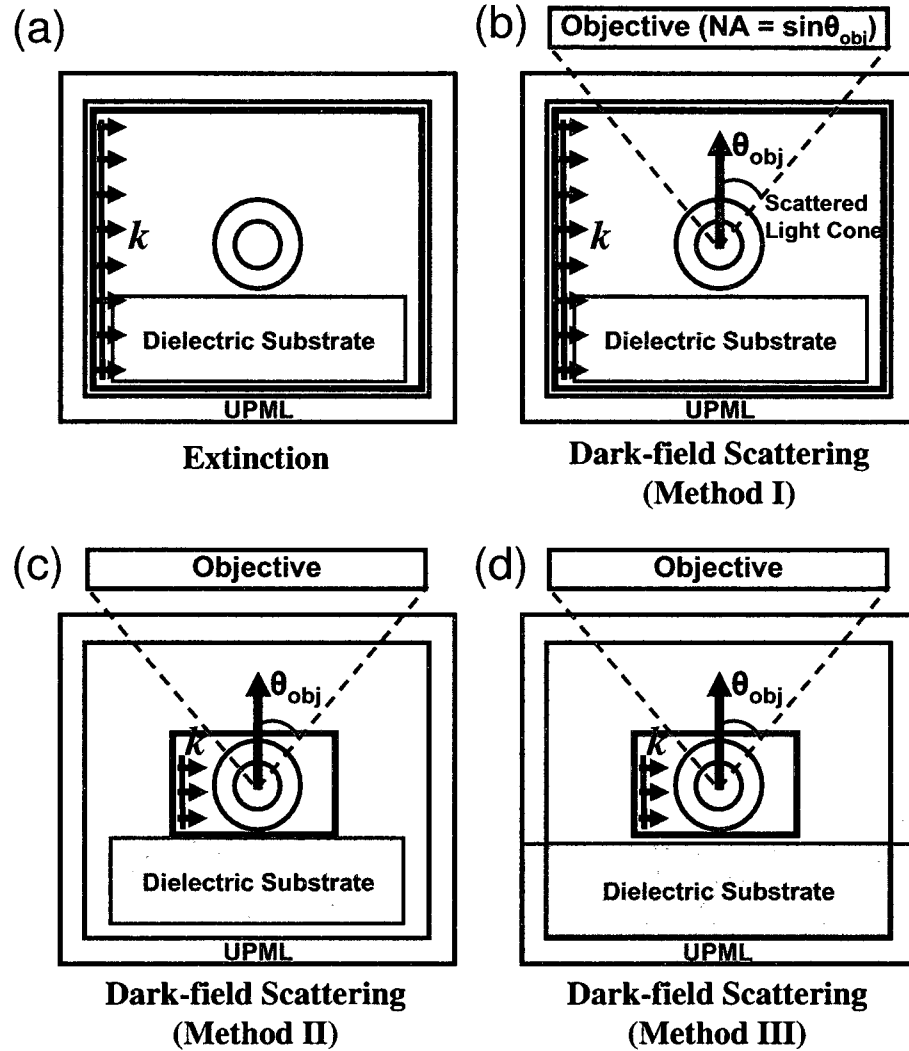


**Figure 4.7** Schematic illustrations of extinction calculations (a) and three different approaches (Methods I-III) for calculating the dark-field scattering spectrum using FDTD. The black arrows represent the pulse insertion. The red boxes represent Discrete Fourier Transform (DFT) monitors enclosing both the nanoshell and substrate (b), or the nanoshell only in (c) and (d). In (b) and (c), the simulation domain is enclosed by a uniform UPML (gray) which is impedance matched to the background medium (vacuum). In (d) the UPML splits into two parts with the upper part matching vacuum and the lower part matching the dielectric. The dark-field spectrum is calculated by integrating the differential far-field scattering spectrum withing the opening angle  $\theta_{obj}$  of the objective.

near-fields are then transformed to angle dependent far-fields using the near-to-far-field transformation based on the Surface Equivalence Theorem.[126] The dark-field scattering spectrum is then calculated by integrating the far-field scattering into the collection cone of the objective (green box). To prevent artificial reflections when the pulse and scattered fields reach the simulation boundaries, the entire simulation domain is enclosed by an efficient absorbing layer, Uniaxial Perfectly Matched Layer (UPML).[126]

While the extinction spectrum can be calculated simply as the sum of absorption and total scattering cross sections, several choices for DFT monitoring and pulse insertions are possible for the dark-field spectrum. Method I (Figure 4.7b) employs the same DFT monitors and pulse insertion as for the extinction spectrum (Figure 4.7a). The scattering spectrum will thus be the true scattering spectrum from a nanoparticle near a finite dielectric slab and thus directly influenced by the FP resonances in the slab. Method II (Figure 4.7c) uses a smaller DFT monitor only enclosing the nanoparticle and a local pulse insertion around the nanoparticle. In this approach, the FP resonances induced in the slab will not contribute directly to the scattering spectrum since the slab is outside the the DFT monitor and the slab is not directly excited by incident light. However, FP resonances will still be induced in the slab due to the near-field coupling between the nanoparticle and the slab. These FP resonances will modulate and enhance the surface charges on the slab and thus indirectly influence



the coupling between the nanoparticle and the surface. In Figure 4.7d, we present an approach (Method III) that effectively eliminates the FP resonances in the slab and provides the differential scattering spectrum for a nanoparticle interacting with an infinite dielectric substrate. The DFT monitor and pulse insertion are the same as for Method II and local to the nanoparticle. A modified UPML is attached directly to the side and bottom surfaces of the slab. This UPML is impedance matched to the dielectric permittivity of the slab so that no internal reflections occur at the relevant surfaces.[126] Therefore, if the dimensions of the slab is sufficiently large that the induced charges at the edges are small, the slab effectively becomes equivalent to an infinite surface.

In Figure 4.8 we compare the extinction spectrum with the dark-field scattering spectrum calculated using methods I-III for different polarizations. The scattering spectrum calculated using Method I displays the same FP resonances as the extinction spectra. Since the same TFSF and DFT boundaries were employed in both extinction and dark-field scattering calculations, the FP resonances originating from the finite substrate modulates the scattering from the finite slab and obscures the plasmon resonances of the nanoparticle. The scattering spectrum calculated using Method II displays no FP resonances and the dipolar and quadrupolar nanoparticle plasmon resonances appears as distinct peaks. The scattering spectrum calculated using Method III is qualitatively similar to that obtained from Method II but with

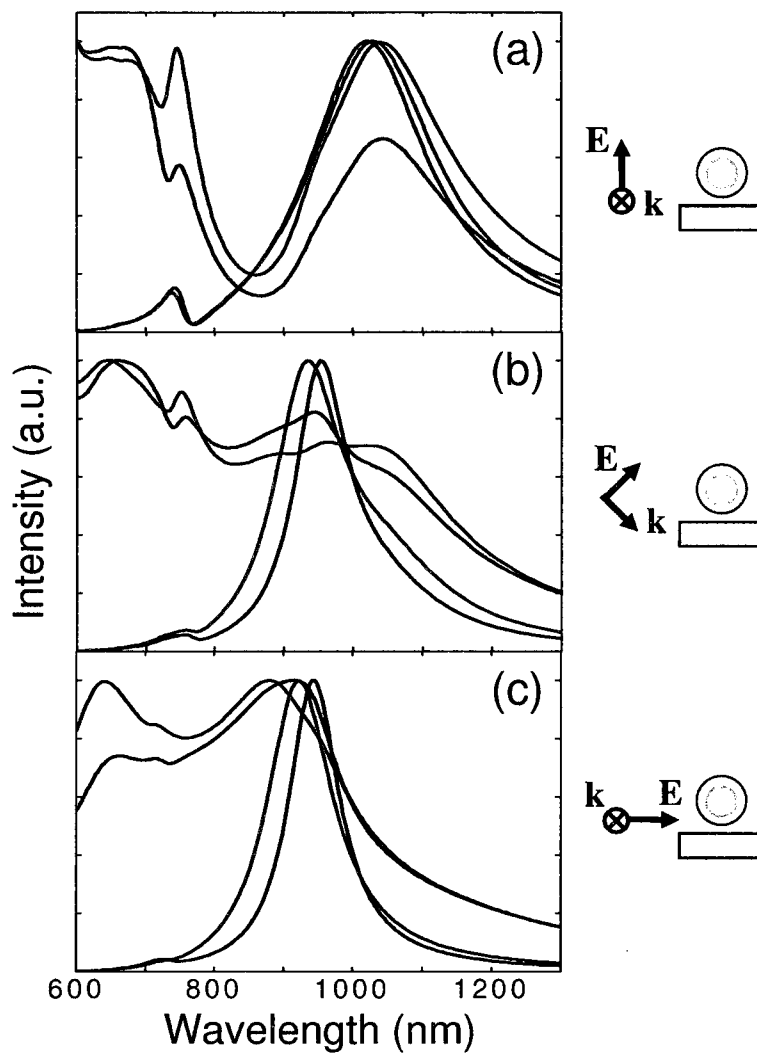


**Figure 4.8** Comparison of the extinction (black) spectra and dark-field scattering spectra calculated using Methods I (green), II (blue), and III (red) for a gold nanoshell near a dielectric surface for different polarizations. The parameters of the dielectric slab are  $\epsilon_S=6.5$ ,  $T=160$  nm,  $L=320$  nm and  $d=2$  nm.

slightly blueshifted peaks. This discrepancy is caused by the indirect excitation of the slab FP resonances through the near-field coupling between the nanoparticle and the slab. The surface charges associated with these FP resonances exaggerates the coupling between the nanoparticle and the surface. Calculations using method III for larger and slightly smaller slabs yield results that are identical to the present results (the convergence tests are shown in Appendix C) and we conclude that the results obtained using method III are the exact results for the scattering spectrum of a nanoparticle on an infinite substrate.

We note that the intensity of the quadrupolar modes is larger for the nanoparticle/substrate system than for the nanoparticle in vacuum (Figure 4.3) because of the substrate-induced hybridization of the nanoparticle quadrupolar and dipolar modes (Figure 4.2c). However, since the effective dipole moment of  $D_1$  for 45-degree polarization is approximately equal to the perpendicular component, i.e.,  $1/\sqrt{2}$ , of the dipole moment of  $D_1$  for the p-polarization, the absolute intensity of the  $Q_2$  mode is not as strong as that of the  $Q_1$  mode, though the intensity ratio of the dipole and quadrupole is roughly the same. To understand why the intensity of the  $Q_1$  mode is strong, one can imagine that, as shown in Figure 4.9a, due to retardation effects, the incident fields first approach the front side of the nanoshell exciting a local dipole on the front part and consequentially excite another dipole with a phase-lag when the incident fields propagate to the back side of the nanoshell. The  $Q_1$  mode can

therefore hybridize with the  $D_1$  mode through the screening charges induced on the substrate by these two dipoles, and result in a larger admixture of the dipole moment. The  $Q_2$  mode hybridizes with the  $D_1$  as well (Figure 4.9b) but possesses a smaller dipole moment. For small nanoparticles when retardation effects are negligible, the enhancement of the  $Q_2$  mode is expected larger than of the  $Q_1$  mode.

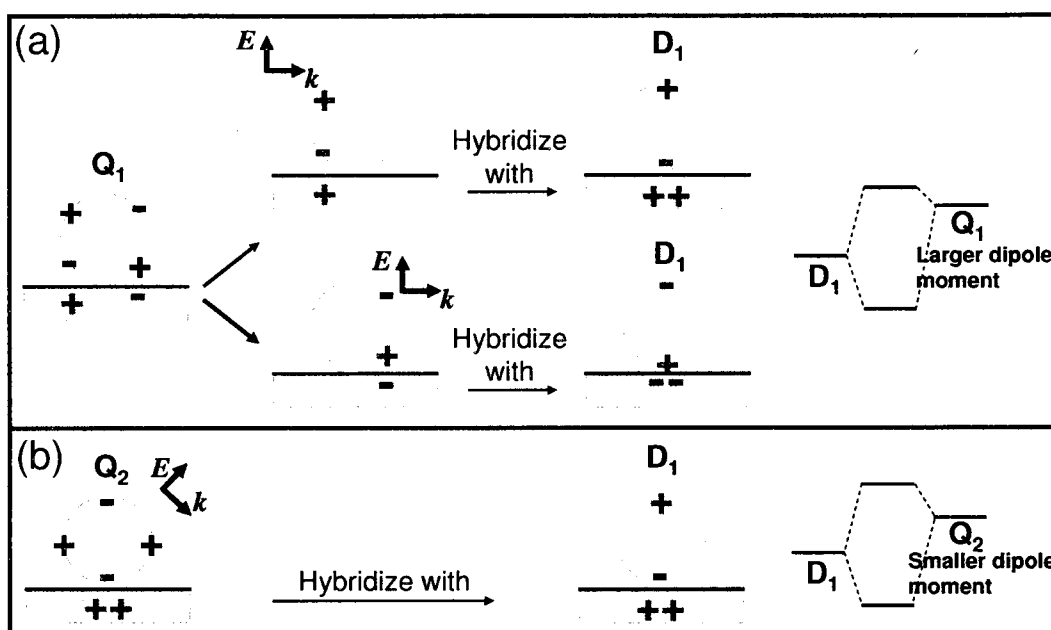


**Figure 4.9** Schematic picture illustrating how quadrupolar mode  $Q_1$  (a) and  $Q_2$  (b) hybridize with the dipolar bonding mode  $D_1$ . Due to the retardation effects,  $Q_1$  possesses a larger dipole moment, while  $Q_2$  possesses a smaller one.

#### 4.4 Experiments and FEM results

Spectra of individual nanoshells on glass, sapphire, and ZnSe substrates were obtained for both s-polarized and p-polarized incident light excitation and compared with both FEM and FDTD calculations of each system (Figure 4.10). On a glass sub-

strate, a relatively small difference is observed in peak energies between s-polarized and p-polarized light. However, the line width of the p-polarized spectrum is increased dramatically relative to the s-polarized spectrum. We also show that the s-polarized spectrum on glass gives a spectrum nearly identical to the result obtained from Mie theory for the same nanoparticle in vacuum. This suggests that one can experimentally approximate the vacuum behavior of a nanoparticle by supporting the particle on a low-index substrate and using only s-polarized light excitation.

Increasing the substrate permittivity increases the mode splitting observed in the s- and p- polarized spectra (Figure 4.10). The broader peaks observed for p-polarized incident light are due to the simultaneous excitation of modes associated with polarizations parallel and perpendicular to the substrate. For the objective used, the polarized light was incident on the sample at an angle of  $79 \pm 2^\circ$ . For s-polarized light, this allows an almost pure polarization parallel to the substrate surface; for p-polarized light, this includes components polarized both perpendicular and parallel to the substrate. Despite the large perpendicularly polarized component of the p-polarized incident light, the associated nanoparticle spectra all have a significant parallel (s-like) component, since the radiation pattern associated with the parallel mode preferentially scatters into the objective.

For p-polarization to the ZnSe substrate, the interaction with the ZnSe surface is sufficiently strong that the quadrupolar nanoshell mode around 2.1 eV also shows up

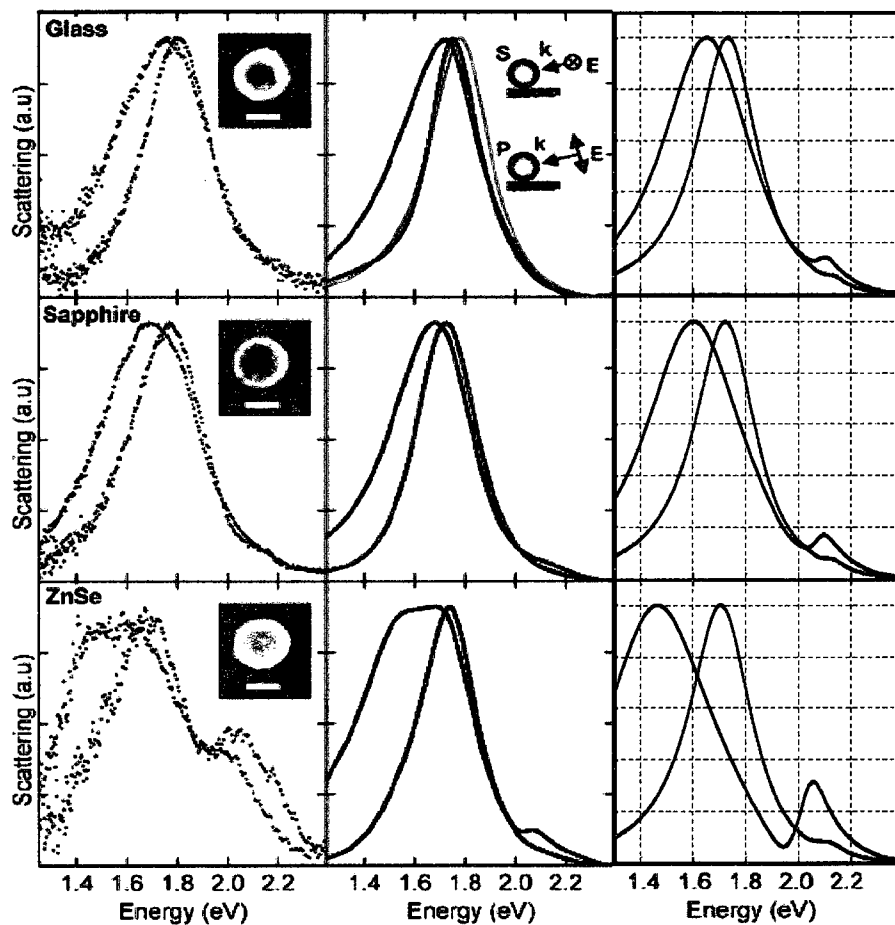


**Figure 4.10** Comparison of experimental (left column) and theoretical calculations (FEM: middle column; FDTD: right column) for nanoshells on glass ( $n = 1.52$ ), sapphire ( $n = 1.77$ ), and ZnSe ( $n = 2.67$ ). Incident light was p-polarized (blue) or s-polarized (black) and incident at  $79 \pm 2^\circ$ . Theoretical spectra correspond to an  $[r_1, r_2] = [67.0, 79.5]$  nm nanoshell calculated 1 nm above the substrate using polarized light incident at  $79^\circ$  with  $NA = 0.9$ . The red curve is Mie theory for the same nanoshell in an isotropic medium (air). Scale bars are 100 nm.

in the scattering spectrum. As mentioned above, this is caused by the inhomogeneous electromagnetic field induced by the substrate. The electromagnetic field induced by the image of a real dipolar nanoparticle plasmon will have a quadrupolar component across the nanoparticle. Similarly, the field from the image of a real quadrupolar nanoparticle plasmon will have a dipolar component across the nanoparticle. The substrate-induced electromagnetic field thus couples the nanoparticle dipolar and quadrupolar plasmons and results in hybridized nanoparticle plasmons of finite dipole moments. The calculated FEM and FDTD spectra agree very well with the experimentally measured spectra for both s- and p-polarizations and for the three different substrates. The slight discrepancies between theory and experiment are most likely due to slight structural deviations from a perfectly spherical nanoshell and perfectly smooth planar substrates in the experimental sample. We also notice that FDTD results show much stronger quadrupole peak compared to FEM results, which is closer to the experimental measurements.

## 4.5 Conclusion

In this chapter, we have performed an extensive FDTD study of the plasmonic interactions between a metallic nanoshell and an adjacent dielectric surface. We show that an extended substrate can be modeled using a finite slab model of sufficient size and how the differential scattering cross section appropriate for typical dark-field single particle spectroscopy can be calculated efficiently. The results of this investigation

show that the symmetry breaking introduced by the substrate can have a profound effect on the plasmon modes of a spherical nanoparticle. In the presence of a dielectric substrate, the degeneracy of the nanoshell dipolar and quadrupolar plasmon resonances is lifted. The three-fold degenerate dipolar mode splits into a redshifted mode oriented perpendicularly to the substrate and two degenerate dipolar modes oriented parallel to the substrate surface. The five-fold degenerate quadrupole modes split into three redshifted modes that can be excited for different polarizations of the incident light. For small nanoparticle-substrate separations, the surface mediates an effective interaction between the different multipolar plasmon resonances of the nanoparticle resulting in intra-nanoparticle hybridization of the plasmon resonances. This hybridization enhances the cross section for the quadrupolar and higher multipolar modes. The redshift and splitting of the modes were found to depend strongly on dimensions of dielectric slabs, nanoparticle-surface separation and the dielectric permittivity of the substrate.



# Chapter 5

## Nanobowtie structures

### 5.1 Introduction

Single-molecule detection with chemical specificity is a powerful and much desired tool for biology, chemistry, physics, and sensing technologies. Surface-enhanced spectroscopies enable single-molecule studies, however, it has been an ongoing challenge to design and fabricate a substrate for systematic SERS at the single-molecule level. Single-molecule SERS sensitivity was first clearly demonstrated using random aggregates of colloidal nanoparticles. [17, 16, 18, 57] Numerous other metal substrate configurations have been used for SERS, including chemically engineered nanoparticles,[36, 58, 59] nanostructures defined by bottom-up patterning,[60, 61] and those made by traditional lithographic approaches.[62] In the most sensitive substrate geometries, incident light excites adjacent subwavelength nanoparticles or nanostructures, resulting in large field enhancements within the interparticle gap.[63, 64] Fractal aggregates of nanoparticles[65] can further increase field enhancements by focusing plasmon energy from larger length scales down to particular nanometer-scale hotspots. [45] However, precise and reproducible formation of such assemblies in predetermined locations has been extremely challenging. An alternative approach is tip-enhanced Raman spectroscopy (TERS), in which the incident light excites an interelectrode plasmon resonance localized between a sharp, metal scanned probe tip and an un-

derlying metal substrate. Recent progress has been made in single-molecule TERS detection.[66, 67, 68] A similar approach was recently attempted using a mechanical break junction.[69] While useful for surface imaging, TERS requires feedback to control the tip-surface gap and is not scalable or readily integrated with other sensing modalities.

A scaleable and highly reliable method was recently demonstrated for producing planar extended electrodes with nanoscale spacings that exhibit very large SERS signals, with each electrode pair having one well-defined hot spot.[70] The structures were fabricated on a Si wafer topped by 200 nm of thermal oxide. Electron beam lithography is used to pattern "multibowtie" structures as shown in Figure 5.1A. As shown, the multibowties consist of two larger pads connected by multiple constrictions. Electromigration was used to form nanometer-scale gaps in the constrictions in parallel, as shown in Figure 5.1B. Figure 5.1C is the close-up of the indicated red square in Figure 5.1B. Postmigration high-resolution scanning electron microscopy (SEM) shows interelectrode gaps ranging from 5 nm to 8 nm.

Confocal scanning Raman microscopy demonstrates the localization of the enhanced Raman emission. The SERS response is consistent with a very small number of molecules in the hotspot, showing blinking and spectral diffusion of Raman lines. Sensitivity is sufficiently high that SERS from physisorbed atmospheric contaminants may be detected after minutes of exposure to ambient conditions. The Raman en-

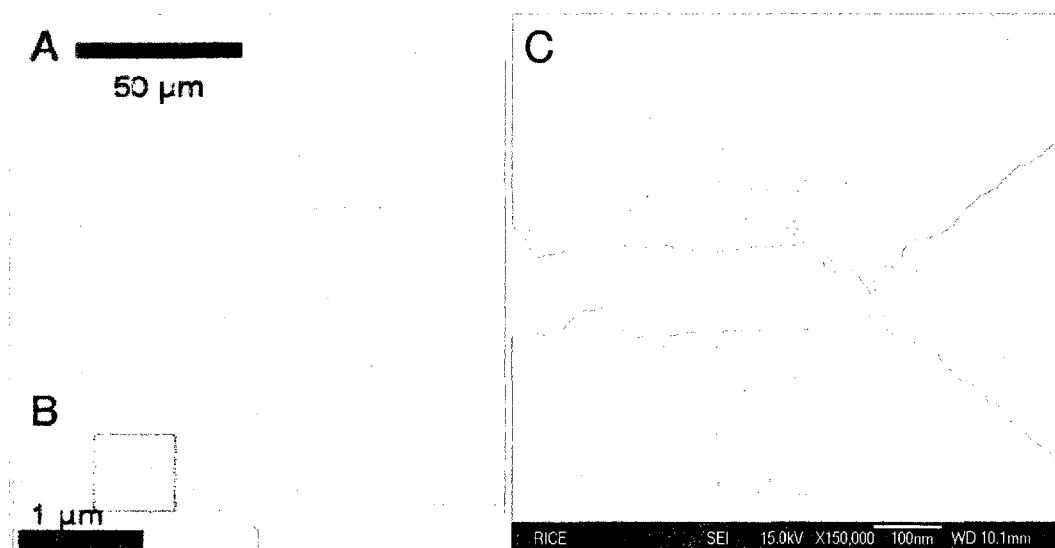


**Figure 5.1** (A) Full multibowtie structure, with seven nanoconstrictions. (B) Close-up of an individual constriction after electromigration. Note that the resulting nanoscale gap is toward the right edge of the indicated red square. (C) Close-up of the indicated red square. The closest separation is around 5 nm.

hancement for para-mercaptoaniline (pMA) is estimated from experimental data to exceed  $10^8$ .

FDTD modeling of realistic structures reveals a rich collection of interelectrode plasmon modes that can readily lead to SERS enhancements as large as  $5 \times 10^{10}$  over a broad range of illumination wavelengths. These structures hold the promise of integration of single-molecule SERS with electronic transport measurements, as well as other near-field optical devices.

Nanoscale gap structures were also used to perform simultaneous measurements of electronic transport and SERS. [71] Conductance in nanoscale gap structures is dominated by roughly a molecular volume. The conductance as a function of time

is observed to correlate strongly with the SERS signal in the junctions measured. Conductance changes correlate with sudden changes in the intensity of sets of Raman modes and with spectral diffusion of mode positions. Experimental data suggest that both SERS and conductance changes are most likely due to changes in conformation and binding of an individual molecule. The combined data provide a great deal of information about the effect of molecular orientation and environment on both conduction and SERS, although a detailed understanding of this correlated information is indeed a very significant theoretical challenge. The most likely explanation for these results is that single-molecule multimodal sensing is possible. This combined measurement technique also opens the possibility of direct assessment of vibrational pumping and local heating in single-molecule electronic transport.

## 5.2 FDTD calculations and discussions

The optical properties of the bowtie structure were calculated using the Finite-Difference Time-Domain method (FDTD). A Drude dielectric function was employed with parameters fitted to the experimental data for gold. This fit provides an accurate description of the optical properties of gold for wavelengths larger than 500 nm.[87] These calculations do not account for reduced carrier mean free path due to surface scattering in the metal film, nor do they include interelectrode tunneling. However, such effects are unlikely to change the results significantly.

### 5.2.1 Perfectly symmetric bowties

As illustrated in Figure 5.2, the bowtie is modeled as a two finite triangular structures truncated in the middle by a gap of air. Our computational method requires the nanostructures to be modeled to be of finite extent. The plasmon modes of a finite system are standing modes with frequencies determined by the size of the sample and the number of nodes of the surface charge distribution associated with the plasmon. For an extended system such as the bowties manufactured in this study, the plasmon resonances can be characterized as traveling surface waves with a continuous distribution of wavevectors.

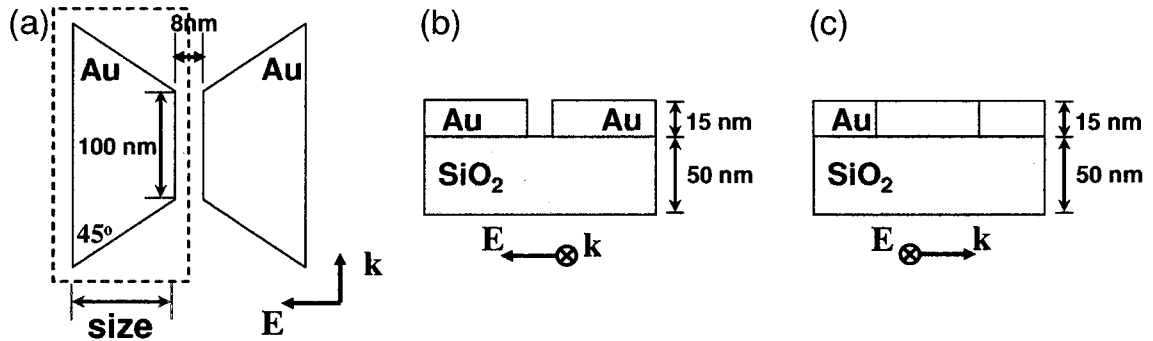


**Figure 5.2** Geometry and parameters of the perfectly symmetric nanobowtie structure. The bowtie is modeled as a two finite gold triangular structures truncated in the middle by a gap of air. (a) Top view. The shorter parallel side of the trapezoid is 100 nm and the base angle is  $45^\circ$ . The size, or the height of the trapezoid is varied. The gap distance is 8 nm. The  $\mathbf{k}$  vector of the excitation is along the parallel sides of trapezoids and  $\mathbf{E}$  is perpendicular to the parallel sides of trapezoids. (b) Side view. A 15 nm Au is deposited on top of a 50 nm  $\text{SiO}_2$  layer. (c) Cross section view.

A series of calculations of bowties with increasing length reveals that the optical spectrum is characterized by increasingly densely spaced plasmon resonances in the

wavelength regime 500-1000 nm and a low energy finite-size induced split-off state involving plasmons localized on the outer surfaces of the bowtie, as shown in Figure 5.3. For a large bowtie, we expect the plasmon resonances in the 500-1000 nm wavelength interval to form a continuous band.[127]

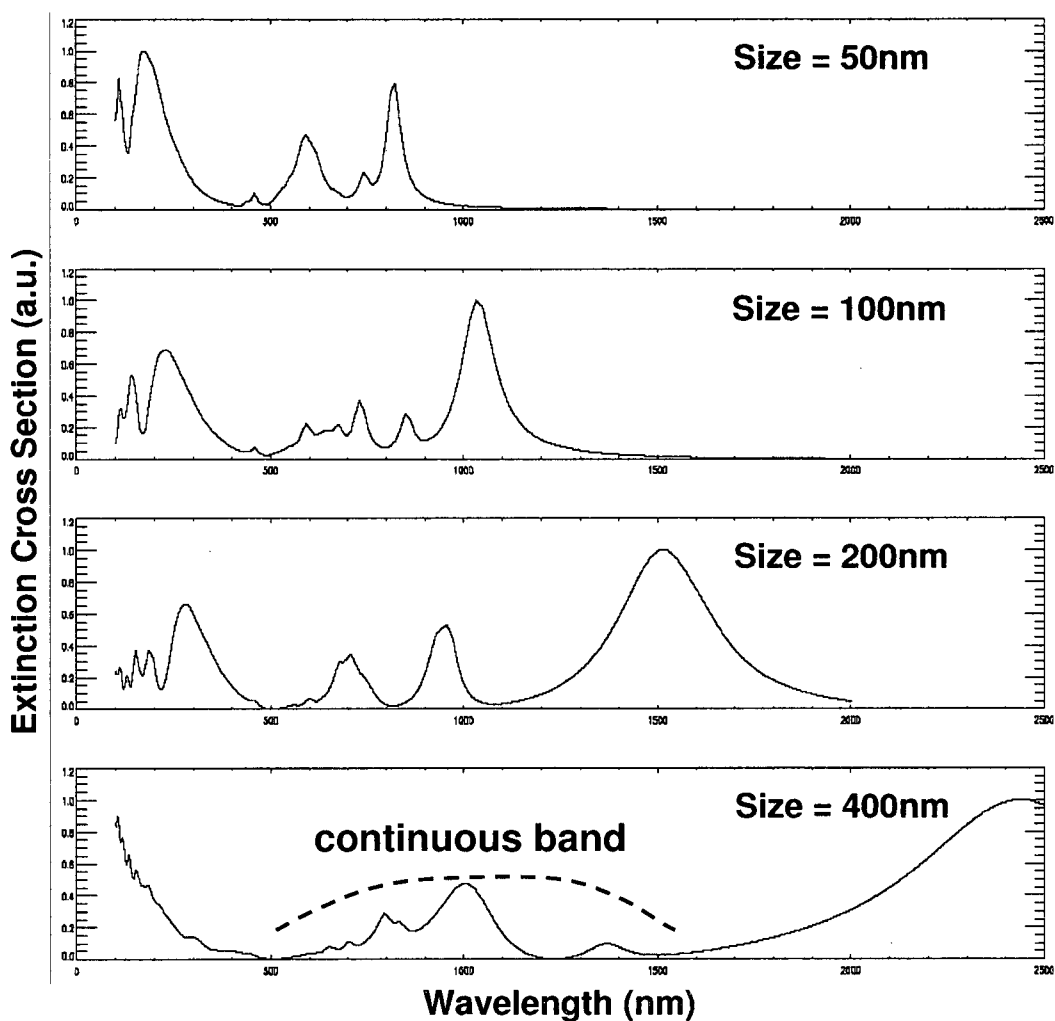


**Figure 5.3** Calculated extinction cross section spectra for bowties with different length, i.e., the height of the trapezoid.

The electric field enhancements across the bowtie junction for the plasmon modes

within this band are relatively similar with large and uniform enhancements in the range of 50-150. The magnitudes of the field enhancements were found to increase with increasing size of the bowtie structure. For instance, the maximum field enhancement factor was found to be 115 for a 200 nm bowtie (Each half of the bowtie is modeled as a truncated triangle 200 nm long.) and 175 for a 400 nm bowtie. Our use of a finite gridsize also underestimates the electric field enhancements.[86] Thus our calculated electric field enhancements are likely to significantly underestimate the actual electric field enhancements in the experimentally manufactured bowties.

### 5.2.2 Bowties with nanoscale asperities

For a perfectly symmetric bowtie, significant field enhancements are only induced for incident light polarized across the junction. If the mirror symmetry is broken, for instance by making one of the structures thicker or triangular, large field enhancements are induced for all polarizations of incident light. To investigate the effects of nanoasperities, FDTD calculations were performed for a bowtie with two semi-spherical Au protrusions in the junction as shown in Figure 5.4. As expected, in Figure 5.5, we find the presence of these protrusions does not influence the optical spectrum. However, the local field enhancements around the protrusions become very large, typically three or four times higher than for the corresponding structure without the defect. The physical mechanism for this increase is an antenna effect caused by the coupling of plasmons localized on the protrusion with the extended plasmons

on the remaining bowtie structure.[128]

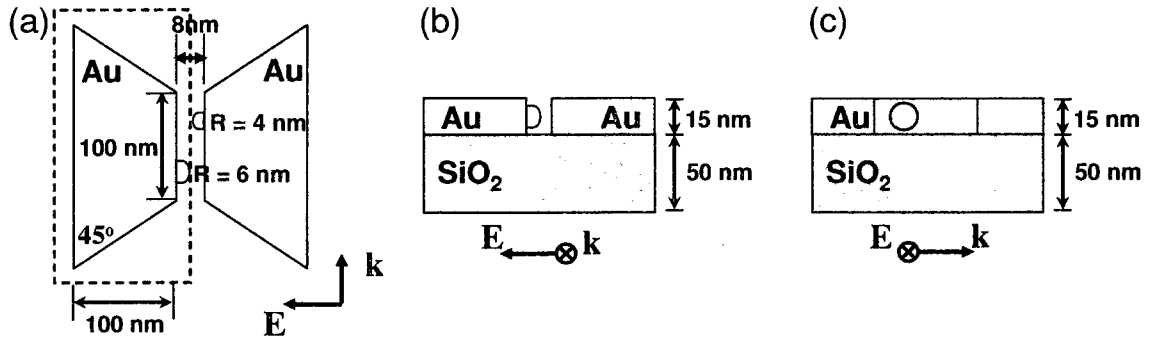


**Figure 5.4** Geometry and parameters of the nanobowtie structure with two protrusions. Same bowtie is modeled as in Figure 5.2 and the length is fixed at 100 nm. (a)-(c) are the same view as explained in Figure 5.2. Two semi-spherical Au protrusions are added in gap region, attaching the cross section of each Au pad, respectively. Protrusion on left (right) electrode has radius of 6 nm (4 nm). The centers of protrusions are both at half of the total thickness of the Au film. The separation of the two protrusions is 50 nm.

### 5.2.3 Hot spots

Furthermore, we use FDTD calculations to understand the strong SERS response in the bowtie structure and roughly estimate enhancement factors. Figure 5.6 shows a calculated extinction spectrum and map of  $|E|^4$  in the vicinity of the junction. These calculations predict that there should be large SERS enhancements across a broad bandwidth of exciting wavelengths because of the complicated mode structure possible in the interelectrode gap. As mentioned previously, nanometer-scale asperities from the electromigration process break the interelectrode symmetry of the structure. The result is that optical excitations at a variety of polarizations can excite many interelectrode modes besides the simple dipolar plasmon commonly consid-



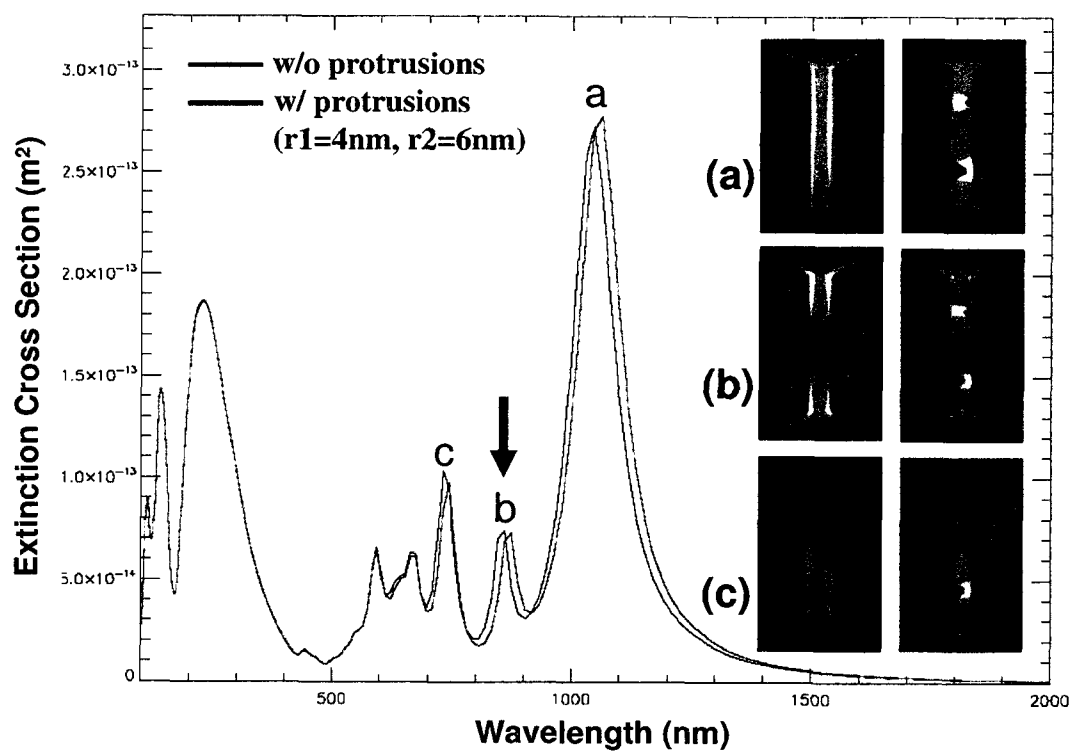


**Figure 5.5** Comparison of calculated extinction cross section spectra for 100 nm bowties (size = 100 nm) with (red) and without (black) protrusions. Panel (a)-(c) are the plots of local electric field enhancements around the gap region for peak a-c marked in the spectrum, respectively.

ered. For extended electrodes, a continuous band of plasmon resonances coupling to wavelengths from 500 to 1000 nm is expected.[127] This broken symmetry also leads to much less dependence of the calculated enhancement on polarization direction, as seen experimentally. The calculations confirm that the electromagnetic enhancement is confined in the normal direction to the film thickness. Laterally, the field enhancement is confined to a region comparable to the radius of curvature of the asperity, as shown in Figure 5.7-5.9. For gaps and asperities in the range of 2 nm, purely electromagnetic enhancements can exceed  $10^{11}$ , approaching that sufficient for single-molecule sensitivity.

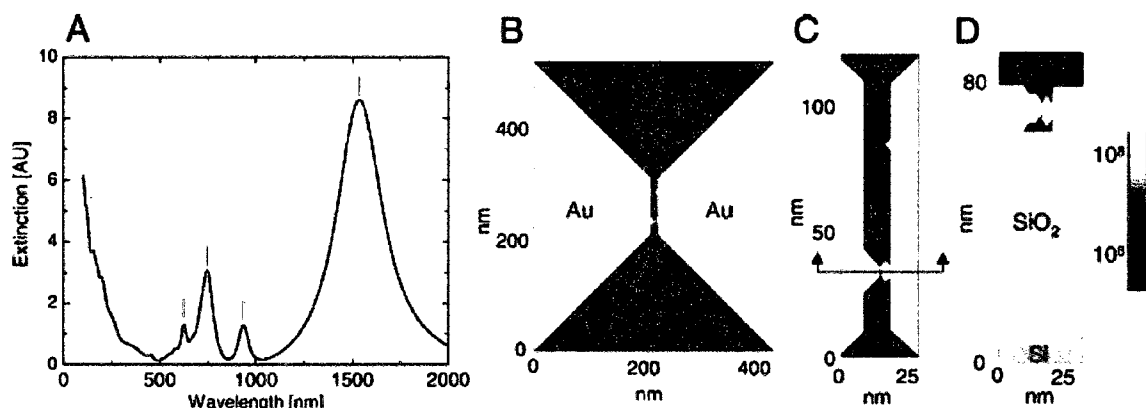


**Figure 5.6** (A) FDTD-calculated extinction spectrum from the model electrode configuration shown in (B). (B) Mock-up electrode tips capped with nanoscale hemispherical asperities, with  $|E|^4$  plotted for the 937 nm resonance of (A). Constriction transverse width at narrowest point is 100 nm. Gap size without asperities is 8 nm. Asperity on left (right) electrode has radius of 6 nm (4 nm). Au film thickness is 15 nm, SiO<sub>2</sub> underlayer thickness is 50 nm. Radiation is normally incident, with polarization oriented horizontally. Grid size for FDTD calculation is 2 nm. (C) Close-up of central region of (B), showing extremely localized enhancement at asperities. (D) Cross section indicated in (C), showing that enhancement in this configuration does not penetrate significantly into the substrate. Predicted maximum electromagnetic Raman enhancement in this mode exceeds  $10^8$ .

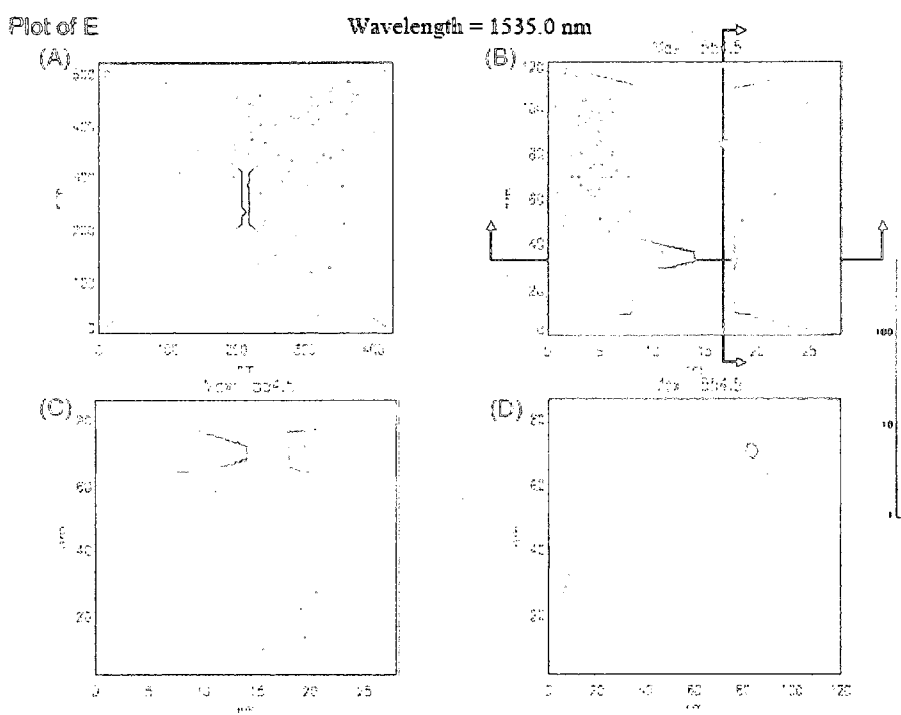


**Figure 5.7** Maps of FDTD-calculated  $|E|$  for the 1535 nm mode indicated in Figure 5.6. Color scale is logarithmic in  $|E|/|E_{inc}|$ . Illumination direction is normal incidence, with electric field polarization oriented horizontally in (A)-(C). Maximum field enhancements are shown. (A) Overall view. (B) Close-up of interelectrode gap showing asperities. (C) Side-view of section indicated in (B) in red. (D) Side view of section indicated in (B) in blue.

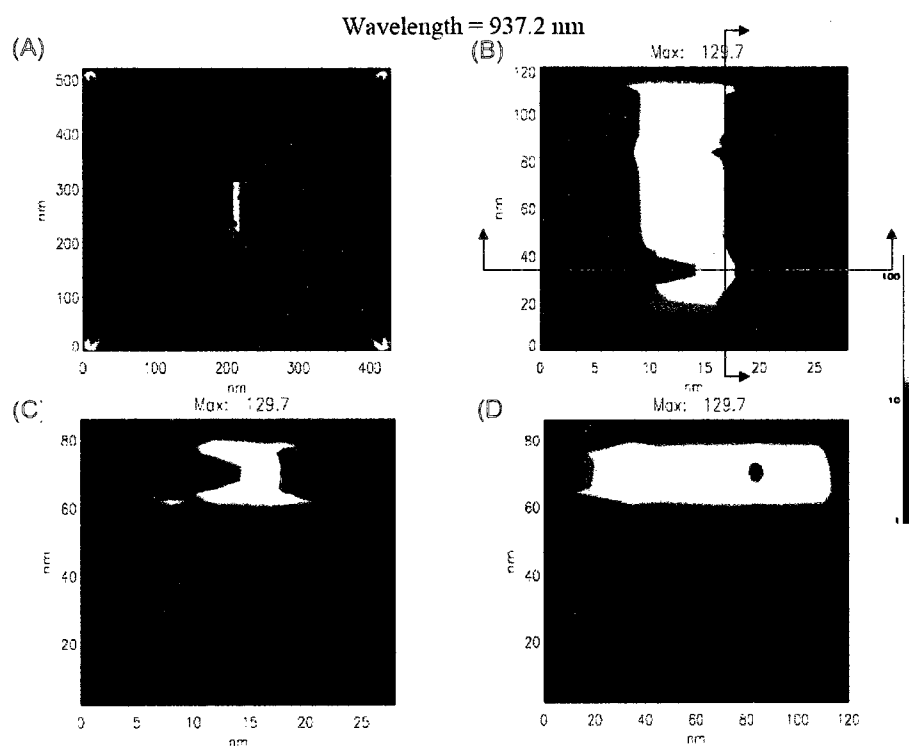


**Figure 5.8** Maps of FDTD-calculated  $|E|$  for the 937 nm mode indicated in Figure 5.6. Color scale is logarithmic in  $|E|/|E_{inc}|$ . Illumination direction is normal incidence, with electric field polarization oriented horizontally in (A)-(C). Maximum field enhancements are shown. (A) Overall view. (B) Close-up of interelectrode gap showing asperities. (C) Side-view of section indicated in (B) in red. (D) Side view of section indicated in (B) in blue.

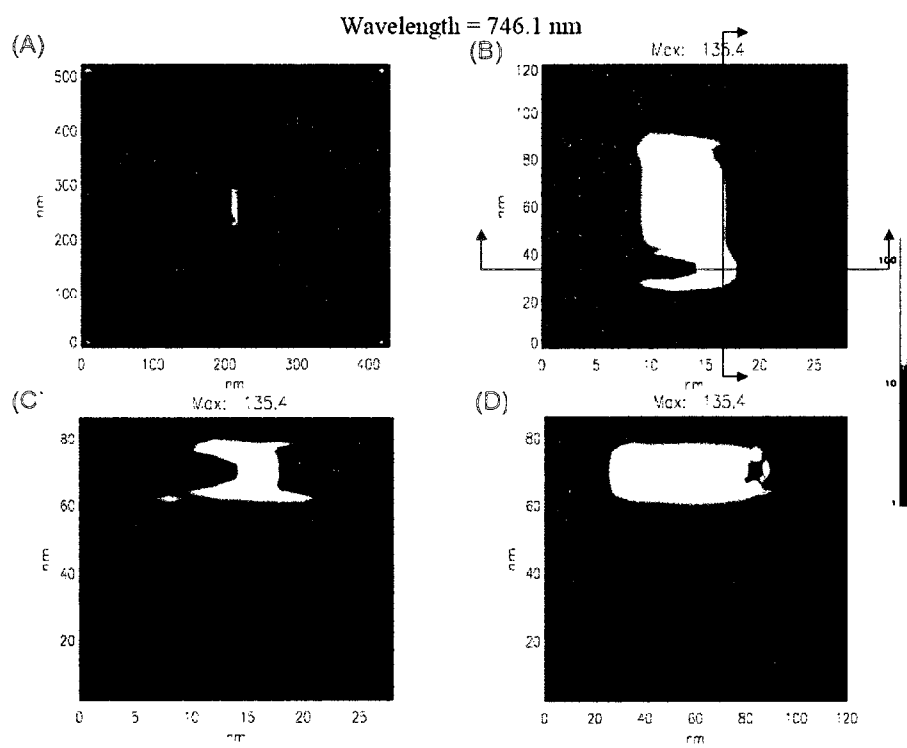


**Figure 5.9** Maps of FDTD-calculated  $|E|$  for the 746 nm mode indicated in Figure 5.6. Color scale is logarithmic in  $|E|/|E_{inc}|$ . Illumination direction is normal incidence, with electric field polarization oriented horizontally in (A)-(C). Maximum field enhancements are shown. (A) Overall view. (B) Close-up of interelectrode gap showing asperities. (C) Side-view of section indicated in (B) in red. (D) Side view of section indicated in (B) in blue.

#### 5.2.4 Interelectrode conductance

Experimentally, [71] it was found that when the conductance of the junction drops below the conductance quantum,  $G_0 = 2e^2/h$ , a tunneling gap is formed, and simultaneous conductance and Raman measurements are performed. It was also found that there are strong correlations in time between conduction and Raman emission. There was a serious concern that changes in tunneling conduction in one part of the junction may alter the plasmon mode structure and affect Raman emission from elsewhere in the junction. Such a scenario could lead to the aforesaid correlations even if conduction and Raman emission are not from the same molecule.

To investigate the effects of a conductance shunting the nanoscale gap, we perform FDTD calculations of the optical properties of such junctions to assess this issue, and the results effectively rule out this concern. The nano-scale gap structures are again modeled as a bowtie with two semi-spherical protrusions in the junction as shown in the closeup in the inset of Figure 5.10a. The electrodes are modeled as regular trapezoids of a height of 50 nm, and a 1 nm grid size was used. The conductance was modeled as a cubical volume 2 nm on a side located between the 6 nm radius asperity and the facing electrode, where the local field enhancement is maximized for modes relevant to the wavelengths used in the experiment. The conductivity of the material was set to be frequency independent over the wavelength range of interest (as expected for tunneling), and chosen such that the conductance of that interelectrode

link was the desired value. The frequency dependent dielectric permittivity of the material is therefore

$$\epsilon(\omega) = \epsilon_{\infty} + \frac{\sigma}{i\omega\epsilon_0} \quad (5.1)$$

where

$$\sigma = G \times \frac{l}{A} \quad (5.2)$$

Figure 5.10a shows a comparison of calculated extinction spectra that characterize the plasmonic mode structure of the gap structure shown, for various values of interelectrode conductance connecting the source and drain at the indicated point. The three most prominent features in the calculated extinction spectrum are labeled. Peak "a" corresponds to the mode shown in the inset, believed to be most relevant for the experiments at hand. An analysis of the instantaneous charge distribution associated with the plasmon resonances in Figure 5.10a shows that negligible charge transfer occurs between the two electrodes for conductances smaller than  $G_0$ . Figure 5.10b shows the evolution of the electric field enhancement factor (calculated for the mid-point of the conducting volume standing in for the molecule) as a function of interelectrode conductance. The field enhancement and mode shapes due to local features in the junction are essentially unaffected by the interelectrode conductance until that conductance exceeds the order of  $G_0 = 2e^2/h = 7.74 \times 10^5 S$ . For conductances significantly larger than  $G_0$ , charges can flow between the two electrodes and a new low energy plasmon resonance appears at wavelengths that depend on

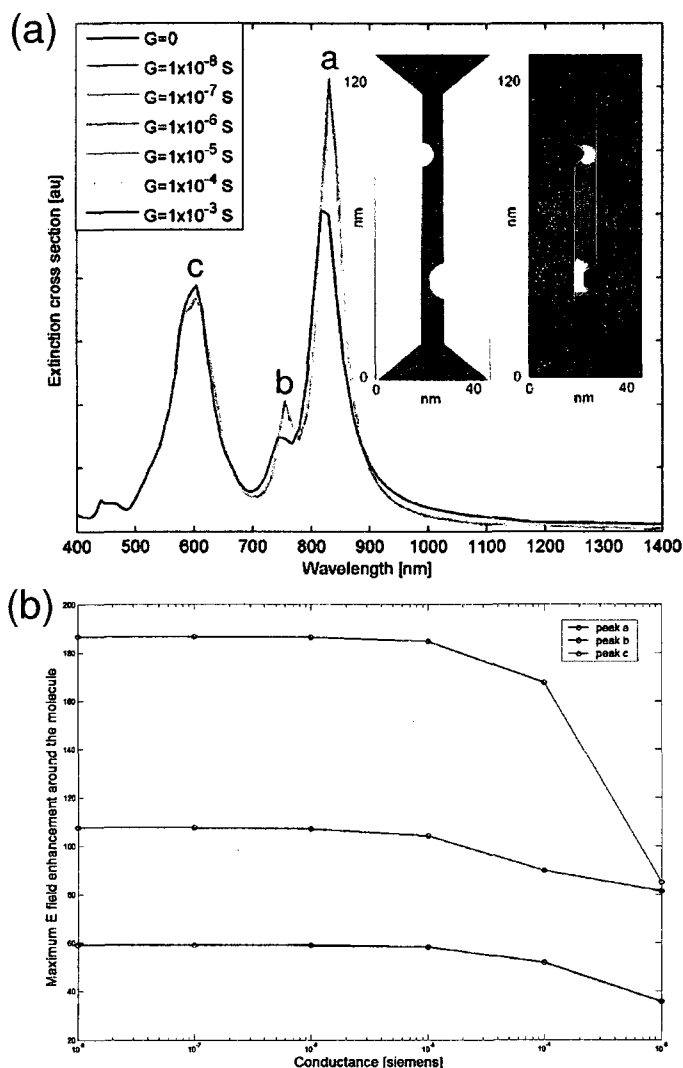


**Figure 5.10** (a) Extinction spectrum calculated using a 1 nm grid size for the structure partially shown in the right inset. The electrodes are modeled as Au, 15 nm thick, sitting on 50 nm thick  $\text{SiO}_2$  dielectric, with an overall interelectrode gap of 8 nm. The upper and lower protrusions into that gap shown are modeled as hemispheres of radii 4 and 6 nm, respectively. The red square indicates the location of the modeled interelectrode conductance (a volume 2 nm on a side, meant to represent a molecule at the interelectrode gap). The right inset shows a map of  $|E|^4$ , where  $E$  is the local electric field normalized by the magnitude of the incident field (roughly the Raman enhancement factor), for the mode near 825 nm. White corresponds to an enhancement of 109. This field map is essentially unchanged until the junction conductance approaches  $10^{-4} S \approx G_0$ . (b) Field enhancement (relative to incident field) calculated at the midpoint of the interelectrode conductance region for the three modes labeled in the upper graph, as a function of interelectrode conductance. Very little change in field enhancement or distribution is seen until interelectrode conductance exceeds  $G_0$ .



the conductance of the shunt. These calculations are completely consistent with the observations in experiments: The plasmonic mode structure responsible for enhanced local fields in the nanogap is established once the interelectrode conductance falls well below  $G_0$ . Given these FDTD results, the only plausible explanation for the aforesaid strong correlations in time between conduction and Raman emission is that both processes involve the same molecule or molecules.

### 5.3 Conclusion

In this chapter, a SERS substrate capable of extremely high sensitivity for trace chemical detection was introduced. Unlike previous substrates, these nanojunctions may be mass fabricated in controlled positions with high yield using a combination of standard lithography and electromigration. FDTD simulations have been performed showing large SERS/local electric field enhancements over a broad band of illuminating wavelengths. FDTD simulations also show that the presence of asperities breaks the mirror symmetry of the bowtie structure, which was used to model electrodes, does not influence the optical spectrum. However, the local field enhancements around the protrusions become very large so the hot spots are well-defined. This was understood as an antenna effect caused by the coupling of plasmons localized on the protrusion with the extended plasmons on the remaining bowtie structure.

The extended electrode geometry and underlying gate electrode are ideal for integration with other sensing modalities such as electronic transport. The plasmonic

mode structure responsible for enhanced local fields in the nanogap is established once the interelectrode conductance falls well below  $G_0$ . The strong correlations in time between conduction and Raman emission is that both processes involve the same molecule or molecules. FDTD calculations are consistent with the observations in experiments.

# Chapter 6

## Conclusions

In this thesis, we apply both Plasmon Hybridization method and Finite-Difference Time-Domain method in analyzing and simulating various metallic nanostructures, such as nanoshells, nanoeegs, nanoshell near dielectric surfaces and nanobowties. We focus on the optical spectrum and both the near-field and far-field of these systems. We also compare our results with experimental measurements and the results from other analytical and numerical algorithms such as Mie Theory as well as the Finite Element method.

For nonconcentric nanoshells, we have shown that symmetry breaking can strongly modify the selection rules for the interaction of plasmon modes on an individual nanoparticle. This finding has profound consequences for the optical spectrum of the particle, allowing all plasmon modes to possess some dipolar character and contribute to additional features in the optical spectrum as symmetry is reduced. For concentric nanoshells, reduction in symmetry also is accompanied by an increased electromagnetic field enhancement on its external surface, located at the narrowest region of shell thickness. This approach may be useful in analyzing and understanding the local and far-field optical responses of other reduced-symmetry nanostructures of even greater complexity and, ultimately, in the design of various nanoparticle geometries

with specific near-field optical properties.

For nanoshells near a dielectric surface, we have shown that the presence of a dielectric substrate beneath an individual plasmonic nanoparticle can strongly influence its plasmon modes, causing the degenerate dipolar peak to split into two distinct modes corresponding to the dipoles oscillating parallel or perpendicular to the surface. These modes can be probed separately using s- or p-polarized incident light. For unpolarized incident light, both modes will be excited, resulting in an anomalously broad plasmon line width due to the mode splitting, rather than the intrinsic lifetime of the modes. The splitting between the perpendicular and parallel mode is found to increase linearly with increasing substrate permittivity, and is strongest for solid Au nanospheres. The finding of a strong substrate-induced anisotropy of the plasmon resonances of nanoshells deposited on a dielectric surface is expected to apply quite generally to other geometries and types of metallic nanoparticles. This effect needs to be considered when using spectra from individual nanoparticles on substrates to deduce plasmon energies and linewidths of individual nanoparticle plasmon modes.

For the nanobowties, we have demonstrated a SERS substrate capable of extremely high sensitivity for trace chemical detection. Unlike previous substrates, these nanojunctions may be mass fabricated in controlled positions with high yield using a combination of standard lithography and electromigration. The resulting hotspot geometry is predicted to allow large SERS enhancements over a broad band

of illuminating wavelengths. Other nonlinear optical effects should be observable in these structures as well. The extended electrode geometry and underlying gate electrode are ideal for integration with other sensing modalities such as electronic transport. Tuning molecule/electrode charge transfer via the gate electrode may also enable the direct examination of the fundamental nature of chemical enhancement in SERS.

We have shown that symmetry breaking can strongly modify the selection rules for the interaction of plasmon modes on an individual nanoparticle. This finding has profound consequences for the optical spectrum of the particle, allowing all plasmon modes to possess some dipolar character and contribute to additional features in the optical spectrum as symmetry is reduced.

# Appendix A

## Facts of RiceFDTD3.0

### A.1 Real-time information

RiceFDTD (current version 3.0) is our homemade parallel computing software package developed by Yanpeng Wu in Nordlander's group at Rice University. This package is used for our basic plasmonic physics research purposes, such as spectral analysis and electric field enhancement simulations of metallic nanostructures.

A big advantage of FDTD is that it provides real time information and allows wide frequency calculations in a single simulation. As shown in Figure A.1, a gold nanoshell (Figure A.1a) with a silica core was simulated. A modulated Gaussian pulse is inserted into the computational domain using the Total-Field/Scattered-Field (TFSF) technique. [126] Snapshots (Figure A.1c-f) of a plane bisecting the nanoshell (Figure A.1b) shows us how the nanoshell surface plasmons are excited. Attention should be paid that after when the pulse was about leaving the computational domain (Figure A.1e), surface plasmon resonances are still observed and then slowly decayed (Figure A.1f).

### A.2 Parallelism

Another advantage of FDTD is its natural parallelizability which allows FDTD being implemented on distributed memory super computers. In Figure A.2, we show

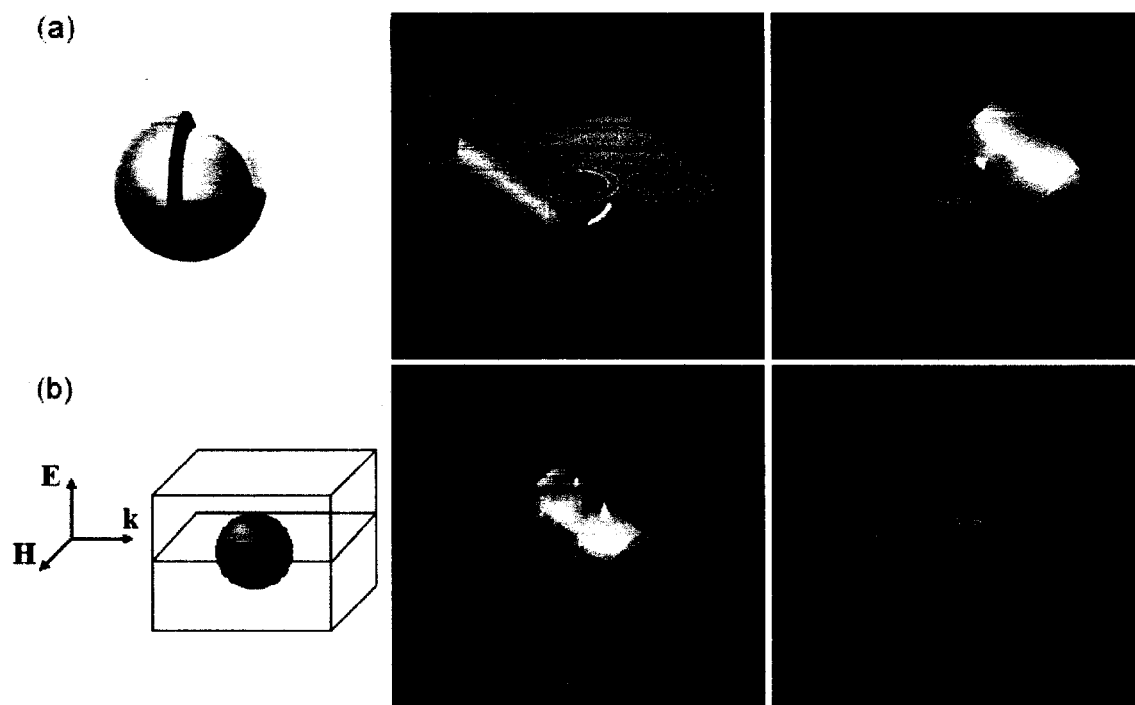


**Figure A.1** Real-time information of a metallic nanoshell surface plasmon resonances. (a) A gold nanoshell with a silica core. The inner and outer radii are 15 nm and 20 nm, respectively. (b) Polarization of the excitation and the plotted cross section: perpendicular to  $E$  cutting through the center of nanoshell. Snapshots are shown at different time step: (c) the pulse is inserted; (d) nanoshell surface plasmons are excited; (e) the pulse is leaving the computational domain; (f) after the pulse is gone.

how it works on RiceFDTD. The FDTD volume is usually divided into  $N$  subdomains and each one is handled by one processor (Figure A.2a). Typically sum of the interfacing areas between all neighbors is required to be smallest to minimize the communication workload when the system is parallelized. Figure A.2b-e show a complete cycle in FDTD simulations. It is important that we are only required to exchange the electric and magnetic field data at the subdomain boundaries. This makes our parallel computation very simple and efficient. [129] As mentioned previously, the electromagnetic dynamics is simulated this way in a leapfrog manner.

Figure A.3 shows a RiceFDTD simulation running across four different CPUs. The object is a gold cylinder and the pulse is inserted at  $45^\circ$  from the upper left corner of subdomain #1. The snapshot (Figure A.3b) shows a smooth and accurate updating process in a parallel FDTD simulation, acting like on a single CPU.

In Figure A.4, we will find the efficiency and scalability of RiceFDTD. The benchmarked super computer is the Shared Tightly Integrated Cluster (STIC), a Rice University's Intel Nahalem computing cluster. It consists of 90 Appro Greenblade E5530 compute nodes. Each node has two quad core 2.4 GHz Intel Xeon (Nahalem) CPUs with 8 MB cache. This gives the system a total of 720 compute cores. STIC is running Red Hat Enterprise Linux 5 and the 2.6.18 kernel. Compilers openmpi/1.3.3-gcc and openmpi/1.3.3-intel are both used for comparison. Same job is tested on 1, 2, 4, 8, 16, 32, 64, 128 and 256 CPUs. Figure A.4 shows the exact execution time



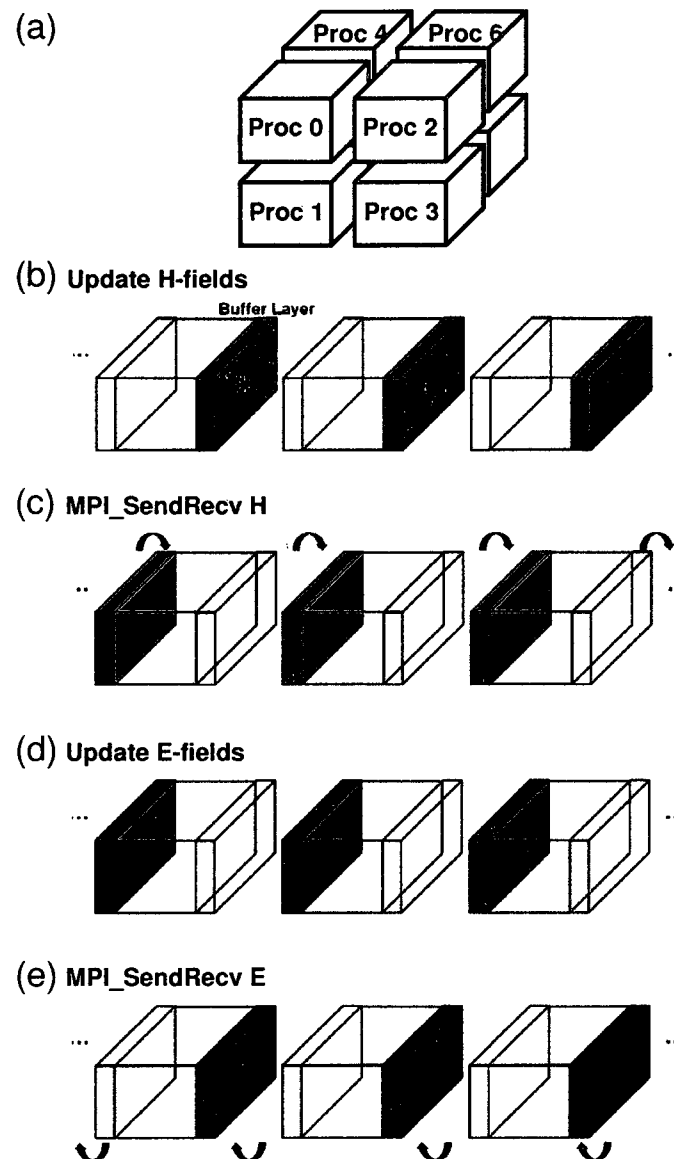


**Figure A.2** Global parallel algorithm in RiceFDTD (one cycle). (a) An entire FDTD volume is divided into 8 subdomains; each one is handled by one processor. All the processors execute the same program. (b) At time step  $T = n\Delta t$ , each processor updates H-fields in the subdomain and stores the boundary data to pre-assigned buffer layers. (c) Neighboring processors exchange boundary data of H-field at the buffer layers by calling MPI-SendRecv function. (d) At time step  $T = (n + 1/2)\Delta t$ , each processor updates E-fields in the subdomain and stores the boundary data to pre-assigned buffer layers. (e) Neighboring processors exchange boundary data of E-field at the buffer layers by calling MPI-SendRecv function.

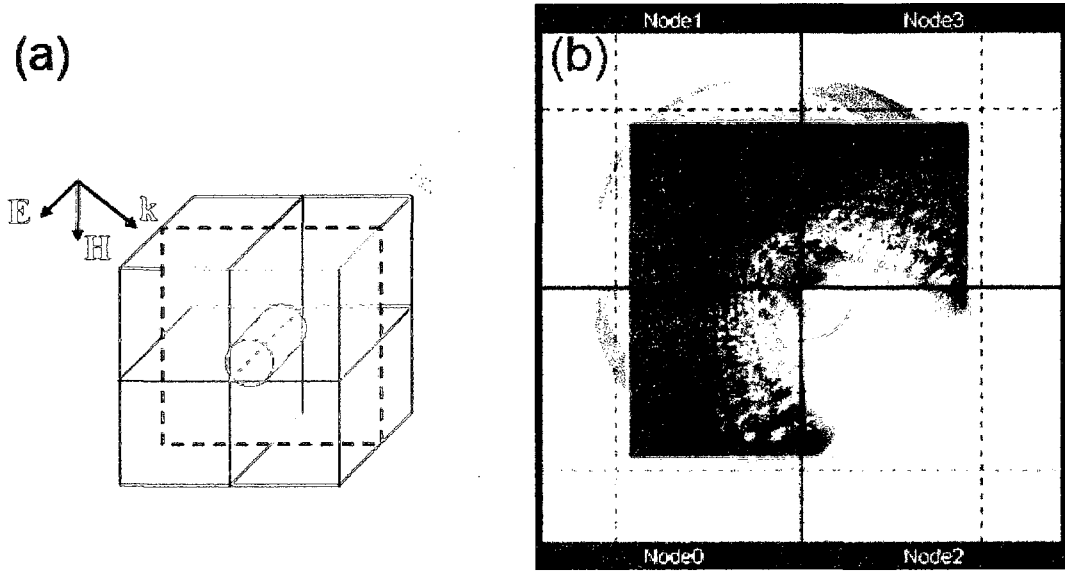


**Figure A.3** A RiceFDTD simulation running across four different CPUs. (a) Schematic picture showing a gold cylinder is bombarded by a pulse inserted from the upper left corner of subdomain # 1. (b) A snapshot of the plane cutting perpendicularly through the center of cylinder (shown in a).

(top), the speedup (middle) and the efficiency (bottom) for different tests, where the speedup is defined as

$$Speedup = \frac{T_1}{T_N} \quad (A.1)$$

and the efficiency is defined as

$$Efficiency = \frac{Speedup}{N}. \quad (A.2)$$

For this simulation, when 256 CPUs are used, the speedup factor approaches 100, so RiceFDTD is very scalable and efficient. When less than 64 CPUs are used, the efficiency is larger than 50%.

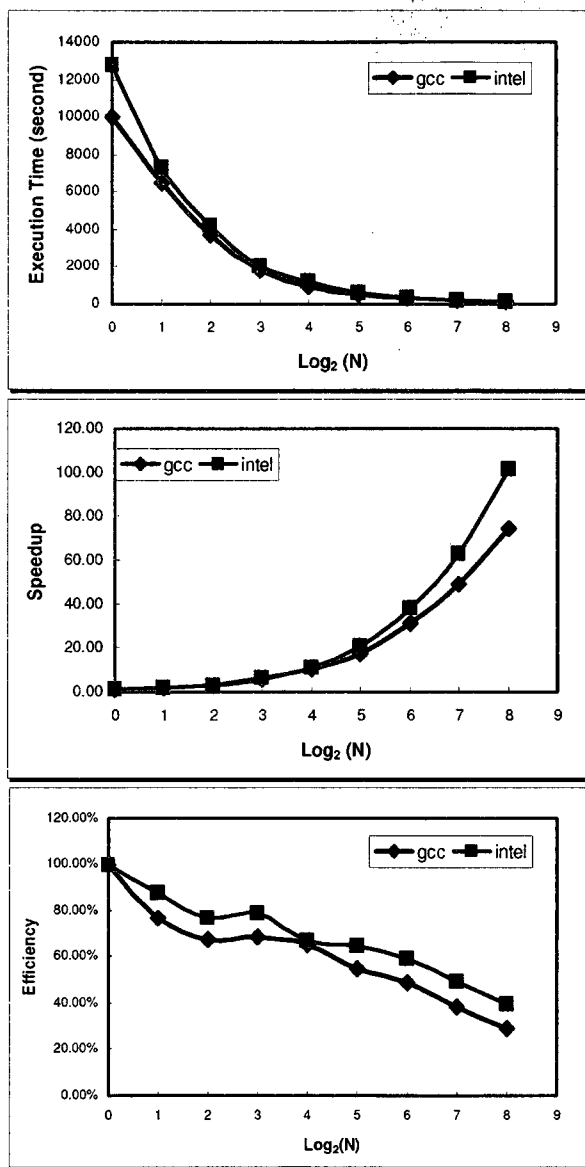


**Figure A.4** Scalability of RiceFDTD on STIC. Exact execution time (top), the speedup (middle) and the efficiency (bottom) for different tests - use different number of CPUs on the same simulation.

# Appendix B

## Derivation of the Lagrangian

### B.1 Matrix notation

In this appendix we describe the matrix notation introduced in the main text. The vector  $\mathbf{X}_m$  is the primitive plasmon amplitude vector defined in Eq. (3.7). For convenience, we introduce the two following notations:

$$\boldsymbol{\eta}_m = \begin{pmatrix} \eta_{C,1m} \\ \eta_{S,1m} \\ \dots \\ \eta_{C,l_{max}m} \\ \eta_{S,l_{max}m} \end{pmatrix}, \quad \boldsymbol{\sigma}_m = \begin{pmatrix} \sigma_{C,1m} \\ \sigma_{S,1m} \\ \dots \\ \sigma_{C,l_{max}m} \\ \sigma_{S,l_{max}m} \end{pmatrix}, \quad (\text{B.1})$$

where  $\eta_{C,lm}$  and  $\eta_{S,lm}$  are the multipolar components in Eq. (3.1) associated with the cavity and sphere plasmon resonances, respectively.  $\sigma_{C,lm}$  and  $\sigma_{S,lm}$  are the multipolar components in Eq. (3.4) and Eq. (3.5), respectively. In the same basis we also introduce a block diagonal matrix  $\hat{R}$  defined as:

$$\hat{R} = \begin{pmatrix} \hat{R}_{ab} & 0 \\ & \dots \\ 0 & \hat{R}_{ab} \end{pmatrix}, \quad \text{where } \hat{R}_{ab} = \begin{pmatrix} a & 0 \\ 0 & b \end{pmatrix}. \quad (\text{B.2})$$

It follows that  $\boldsymbol{\eta}_m = \hat{A}_m \dot{\mathbf{X}}_m$  and  $\boldsymbol{\sigma}_m = (n_0 e) \hat{B}_m \mathbf{X}_m$ , where  $\hat{A}_m$  and  $\hat{B}_m$  are block

diagonal matrices:

$$\hat{A}_m = \begin{pmatrix} \hat{A}_{1m} & & 0 \\ & \dots & \\ 0 & & \hat{A}_{l_{max}m} \end{pmatrix}, \hat{B}_m = \begin{pmatrix} \hat{B}_{1m} & & 0 \\ & \dots & \\ 0 & & \hat{B}_{l_{max}m} \end{pmatrix}, \quad (\text{B.3})$$

with the general term

$$\hat{A}_{lm} = \begin{pmatrix} \sqrt{\frac{1}{(l+1)a}} Y_{lm}(\Omega_C) & x^l \sqrt{\frac{1}{lb}} M_{lm}(\Omega_C) \\ x^{l+1} \sqrt{\frac{1}{(l+1)a}} N_{lm}(\Omega_S) & \sqrt{\frac{1}{lb}} Y_{lm}(\Omega_S) \end{pmatrix}, \quad (\text{B.4})$$

and

$$\hat{B}_{lm} = \begin{pmatrix} \sqrt{\frac{l+1}{a^3}} Y_{lm}(\Omega_C) & -x^{l-1} \sqrt{\frac{l}{b^3}} P_{lm}(\Omega_C) \\ -x^{l+2} \sqrt{\frac{l+1}{a^3}} Q_{lm}(\Omega_S) & \sqrt{\frac{l}{b^3}} Y_{lm}(\Omega_S) \end{pmatrix}, \quad (\text{B.5})$$

where  $x = a/b$  is the aspect ratio and we define

$$M_{lm}(\Omega_C) = \left[ \frac{r_S(a, \theta_C)}{a} \right]^l Y_{lm}(\Omega_S(a, \Omega_C)) \quad (\text{B.6})$$

$$N_{lm}(\Omega_S) = \left[ \frac{b}{r_C(b, \theta_S)} \right]^{l+1} Y_{lm}(\Omega_C(b, \Omega_S)) \quad (\text{B.7})$$

$$P_{lm}(\Omega_C) = \frac{\partial}{\partial r_C} \left[ \frac{r_S^l(r_C, \theta_C)}{la^{l-1}} Y_{lm}(\Omega_S(r_C, \theta_C)) \right] \Big|_{r_C=a} \quad (\text{B.8})$$

$$Q_{lm}(\Omega_S) = -\frac{\partial}{\partial r_S} \left[ \frac{b^{l+2} Y_{lm}(\Omega_C(r_S, \theta_S))}{(l+1)r_C^{l+1}(r_S, \theta_S)} \right] \Big|_{r_S=b} \quad (\text{B.9})$$

### B.1.1 Kinetic energy

In our matrix notation, the kinetic energy Eq. (3.6) becomes

$$T_m = \frac{m_e}{2e} \sum_{l_i, l_j} \left[ \int a^2 \eta_{l_i, m}^* \dot{\sigma}_{C, l_j m} \Big|_{r_C=a} d\Omega_C \right]$$

$$\begin{aligned}
& + \left[ \int b^2 \eta_{i,m}^* \dot{\sigma}_{S,l_j,m} \Big|_{r_S=b} d\Omega_S \right] \\
& = \frac{m_e}{2e} \int (\hat{R} \boldsymbol{\eta}_m^*)^T (\hat{R} \dot{\boldsymbol{\sigma}}_m) d\Omega \\
& = \frac{1}{2} n_0 m_e \int (\hat{R} \hat{A}_m^* \dot{\mathbf{X}}_m)^T (\hat{R} \hat{B}_m \dot{\mathbf{X}}_m) d\Omega, \tag{B.10}
\end{aligned}$$

where  $\Omega$  denotes the appropriate solid angle in the coordinate system. Here and in the following, a superscript  $\mathbf{T}$  indicates the transpose of a vector or matrix. We therefore express  $T_m$  as a matrix:

$$T_m = \frac{1}{2} n_0 m_e (\dot{\mathbf{X}}_m^T \hat{T}_m \dot{\mathbf{X}}_m) \Leftrightarrow \hat{T}_m = \int \hat{A}_m^{*\mathbf{T}} \hat{R}^T \hat{R} \hat{B}_m d\Omega. \tag{B.11}$$

Here  $\hat{T}_m$  is a  $2l_{max} \times 2l_{max}$  matrix. All odd rows and columns represent  $C$  terms and the even ones represent  $S$  terms. To refer to the matrix elements, we use a notation  $T_{XY,l_i,l_j}^{(m)}$ . For example,  $T_{CS,l_i,l_j}^{(m)}$  represents the element located at the  $(2l_i - 1)$ th row and the  $(2l_j)$ th column. In this notation, we can express the elements of  $\hat{T}_m$  as:

$$T_{CC,l_i,l_j}^{(m)} = \delta_{l_i,l_j} - x^{l_i+l_j+1} \sqrt{\frac{l_i+1}{l_j+1}} I_{l_i,l_j,m}^{S,Q,N} \tag{B.12}$$

$$T_{SS,l_i,l_j}^{(m)} = \delta_{l_i,l_j} - x^{l_i+l_j+1} \sqrt{\frac{l_i}{l_j}} I_{l_i,l_j,m}^{C,P,M} \tag{B.13}$$

$$T_{CS,l_i,l_j}^{(m)} = \sqrt{\frac{l_i+1}{l_j}} \left[ x^{l_j+1/2} I_{l_i,l_j,m}^{C,Y,M} - x^{l_i+1/2} I_{l_i,l_j,m}^{S,Q,Y} \right] \tag{B.14}$$

$$T_{SC,l_i,l_j}^{(m)} = \sqrt{\frac{l_i}{l_j+1}} \left[ x^{l_j+1/2} I_{l_i,l_j,m}^{S,Y,N} - x^{l_i+1/2} I_{l_i,l_j,m}^{C,P,Y} \right], \tag{B.15}$$

where we define:

$$I_{l_i,l_j,m}^{r,\Gamma,\Delta} = \int \Gamma_{l_i,m}^*(\Omega_r) \Delta_{l_j,m}(\Omega_r) d\Omega_r. \tag{B.16}$$

In this definition, the superscript  $r$  indicates the coordinate system, i.e.  $C$ , the coordinate system centered on the cavity or  $S$ , the coordinate system centered on the sphere.  $\Gamma$  represents  $P_{lm}(\Omega_C)$ , or  $Q_{lm}(\Omega_S)$ , or the spherical harmonics  $Y_{lm}(\Omega_C)$  or  $Y_{lm}(\Omega_S)$ , depending on what the superscript  $r$  is. Similarly,  $\Delta$  represents  $M_{lm}(\Omega_C)$ , or  $N_{lm}(\Omega_S)$ , or  $Y_{lm}(\Omega_C)$  or  $Y_{lm}(\Omega_S)$ . The subscripts of  $I_{l_i, l_j, m}^{r, \Gamma, \Delta}$ ,  $(l_i, m)$  and  $(l_j, m)$  are the multipolar order of  $\Gamma$  and  $\Delta$  respectively. The quantity  $\delta_{l_i, l_j}$  is Dirac's delta function.

For a concentric nanoshell  $D = 0$ ,  $I_{l_i, l_j, m} \rightarrow \delta_{l_i, l_j}$ , and  $\hat{T}_m$  reduces to a block diagonal matrix. As the offset  $D$  increases, the off-diagonal ( $l_i \neq l_j$ ) terms become finite.

### B.1.2 Potential energy

To calculate the electrostatic potential, we start from the multipole expansion:

$$\begin{aligned} \Phi(\mathbf{r}) &= \int \frac{\sigma(\mathbf{r}')}{|\mathbf{r} - \mathbf{r}'|} d\mathbf{r}' = \sum_{l', m'} \frac{4\pi}{2l' + 1} Y_{l', m'}(\Omega) \times \\ &\int \frac{r'^l}{r^{l'+1}} Y_{l', m'}^*(\Omega') \sigma(\mathbf{r}') r'^2 dr' d\Omega' . \end{aligned} \quad (\text{B.17})$$

Since only the spill out charges will contribute to the electrostatic potential, we use  $\Phi^{(in)}$  and  $\Phi^{(out)}$  to represent electrostatic potential on the inner and outer surfaces, respectively.

On the inner surface, where  $r_C = a$ ,  $\Phi^{(in)}$  can be separated into two parts:

$$\Phi^{(in)}(\Omega_C) = \Phi_C^{(in)} + \Phi_S^{(in)} , \quad (\text{B.18})$$

where the subscript  $C$  means the contribution comes from the inner surface charges and  $S$  means from the outer surface charges. These two components are:

$$\begin{aligned} \Phi_{C,lm}^{(in)}(\Omega_C) &= \left[ \frac{4\pi}{2l+1} \sqrt{\frac{l+1}{a}} Y_{lm}(\Omega_C) \right] C_{lm} - \\ &\left[ \sum_{l'} \frac{4\pi}{2l'+1} \sqrt{\frac{l}{b}} x^l Y_{l'm}(\Omega_C) I_{l',l,m}^{C,Y,P} \right] S_{lm} \end{aligned} \quad (\text{B.19})$$

$$\begin{aligned} \Phi_{S,lm}^{(in)}(\Omega_C) &= \left[ \frac{4\pi}{2l+1} \sqrt{\frac{l}{b}} x^l M_{lm}(\Omega_C) \right] S_{lm} - \\ &\left[ \sum_{l'} \frac{4\pi}{2l'+1} \sqrt{\frac{l+1}{a}} x^{l+l'+1} M_{l'm}(\Omega_C) I_{l',l,m}^{S,Y,Q} \right] C_{lm}, \end{aligned} \quad (\text{B.20})$$

where the function  $I$  is defined in Eq. (B.16).

In the same way, on the outer surface,

$$\Phi^{(out)}(\Omega_S) = \Phi_C^{(out)} + \Phi_S^{(out)} \quad (\text{B.21})$$

and

$$\begin{aligned} \Phi_{C,lm}^{(out)}(\Omega_S) &= \left[ \frac{4\pi}{2l+1} \sqrt{\frac{l+1}{a}} x^{l+1} N_{lm}(\Omega_S) \right] C_{lm} - \\ &\left[ \sum_{l'} \frac{4\pi}{2l'+1} \sqrt{\frac{l}{b}} x^{l+l'+1} N_{l'm}(\Omega_S) I_{l',l,m}^{C,Y,P} \right] S_{lm} \end{aligned} \quad (\text{B.22})$$

$$\begin{aligned} \Phi_{S,lm}^{(out)}(\Omega_S) &= \left[ \frac{4\pi}{2l+1} \sqrt{\frac{l}{b}} Y_{lm}(\Omega_S) \right] S_{lm} - \\ &\left[ \sum_{l'} \frac{4\pi}{2l'+1} \sqrt{\frac{l+1}{a}} x^{l+1} Y_{l'm}(\Omega_S) I_{l',l,m}^{S,Y,Q} \right] C_{lm}. \end{aligned} \quad (\text{B.23})$$



Again, with the notations introduced above, the electrostatic potential of azimuthal symmetry  $m$  can be written:

$$\Phi_m = \hat{\Phi}_m \mathbf{X}_m, \quad (\text{B.24})$$

where  $\hat{\Phi}_m$  is a block diagonal matrix:

$$\hat{\Phi}_m = \begin{pmatrix} \hat{\Phi}_{1m} & 0 \\ & \dots \\ 0 & \hat{\Phi}_{l_{max}m} \end{pmatrix}, \quad (\text{B.25})$$

with:

$$\hat{\Phi}_{lm} = \begin{pmatrix} \Phi_{CC,lm}^{(in)} + \Phi_{SC,lm}^{(in)} & \Phi_{CS,lm}^{(in)} + \Phi_{SS,lm}^{(in)} \\ \Phi_{CC,lm}^{(out)} + \Phi_{SC,lm}^{(out)} & \Phi_{CS,lm}^{(out)} + \Phi_{SS,lm}^{(out)} \end{pmatrix}. \quad (\text{B.26})$$

Here for example the notation  $\Phi_{SC,lm}^{(in)}$  represents the coefficient of  $C_{lm}$  term in  $\Phi_{S,lm}^{(in)}(\Omega_C)$  (Eq. (B.20)) and it is similar for the others. In this way, we collect the coefficients of  $C_{lm}$  terms in the left column and the coefficients of  $S_{lm}$  terms in the right column of matrix  $\hat{\Phi}_{lm}$ . The elements in top and bottom rows are functions of the coordinates  $\Omega_C$  and  $\Omega_S$ , respectively.

The potential energy is obtained from Eq. (3.9) and can be written in a matrix form:

$$V_m = \frac{1}{2} \sum_{l_i, l_j} \left[ \int a^2 \sigma_{C,l_i m}^*(\Omega_C) \Phi_{l_j m}^{(in)}(\Omega_C) d\Omega_C + \int b^2 \sigma_{S,l_i m}^*(\Omega_S) \Phi_{l_j m}^{(out)}(\Omega_S) d\Omega_S \right]$$

$$\begin{aligned}
&= \frac{1}{2} \int (\hat{R}\boldsymbol{\sigma}_m^*)^T (\hat{R}\boldsymbol{\Phi}_m) d\Omega \\
&= \frac{1}{2} n_0 m_e \int (\hat{R}\hat{B}_m^* \mathbf{X}_m)^T (\hat{R}\hat{\Phi}_m \mathbf{X}_m) d\Omega.
\end{aligned} \tag{B.27}$$

As for the kinetic energy Eq. (B.11), we can express the potential energy as a quadratic form:

$$V_m = \frac{1}{2} n_0 m_e (\mathbf{X}_m^T \hat{V}_m \mathbf{X}_m) \Leftrightarrow \hat{V}_m = \int \hat{B}_m^{*T} \hat{R}^T \hat{R} \hat{\Phi}_m d\Omega. \tag{B.28}$$

Using the same index notation as for  $\hat{T}_m$ , we express the matrix elements of  $\hat{V}_m$  as:

$$\begin{aligned}
V_{CC,l_i,l_j}^{(m)} &= \omega_{C,l_i} \omega_{C,l_j} \left[ \delta_{l_i,l_j} - \sqrt{\frac{2l_i+1}{2l_j+1}} x^{l_i+l_j+1} I_{l_i,l_j,m}^{S,Q,N} \right. \\
&\quad \left. + \sum_{l'} \frac{\sqrt{(2l_i+1)(2l_j+1)}}{2l'+1} x^{l_j+1} \times \right. \\
&\quad \left. I_{l',l_j,m}^{S,Y,Q} \left( x^{l_i} I_{l_i,l',m}^{S,Q,Y} - x^{l'} I_{l_i,l',m}^{C,Y,M} \right) \right]
\end{aligned} \tag{B.29}$$

$$\begin{aligned}
V_{SS,l_i,l_j}^{(m)} &= \omega_{S,l_i} \omega_{S,l_j} \left[ \delta_{l_i,l_j} - \sqrt{\frac{2l_i+1}{2l_j+1}} x^{l_i+l_j+1} I_{l_i,l_j,m}^{C,P,M} \right. \\
&\quad \left. + \sum_{l'} \frac{\sqrt{(2l_i+1)(2l_j+1)}}{2l'+1} x^{l_j+1} \times \right. \\
&\quad \left. I_{l',l_j,m}^{C,Y,P} \left( x^{l_i} I_{l_i,l',m}^{C,P,Y} - x^{l'} I_{l_i,l',m}^{S,Y,N} \right) \right]
\end{aligned} \tag{B.30}$$

$$\begin{aligned}
V_{CS,l_i,l_j}^{(m)} &= \omega_{C,l_i} \omega_{S,l_j} \left[ \sqrt{\frac{2l_i+1}{2l_j+1}} \left( x^{l_j+1/2} I_{l_i,l_j,m}^{C,Y,M} - \right. \right. \\
&\quad \left. \left. x^{l_i+1/2} I_{l_i,l_j,m}^{S,Q,Y} \right) - \sqrt{\frac{2l_j+1}{2l_i+1}} x^{l_j+1/2} I_{l_i,l_j,m}^{C,Y,P} \right. \\
&\quad \left. + \sum_{l'} \frac{\sqrt{(2l_i+1)(2l_j+1)}}{2l'+1} x^{l_i+l_j+l'+3/2} \times \right. \\
&\quad \left. I_{l_i,l',m}^{S,Q,N} I_{l',l_j,m}^{C,Y,P} \right]
\end{aligned} \tag{B.31}$$

$$\begin{aligned}
V_{SC,l,l_j}^{(m)} = & \omega_{S,l_i} \omega_{C,l_j} \left[ \sqrt{\frac{2l_i+1}{2l_j+1}} (x^{l_j+1/2} I_{l_i,l_j,m}^{S,Y,N} - \right. \\
& x^{l_i+1/2} I_{l_i,l_j,m}^{C,P,Y}) - \sqrt{\frac{2l_j+1}{2l_i+1}} x^{l_j+1/2} I_{l_i,l_j,m}^{S,Y,Q} \\
& + \sum_{l'} \frac{\sqrt{(2l_i+1)(2l_j+1)}}{2l'+1} x^{l_i+l_j+l'+3/2} \times \\
& \left. I_{l_i,l',m}^{C,P,M} I_{l',l_j,m}^{S,Y,Q} \right], \tag{B.32}
\end{aligned}$$

where we introduce the plasmon frequency for a cavity,

$$\omega_{C,l} = \omega_B \sqrt{\frac{l+1}{2l+1}} \tag{B.33}$$

and for a solid sphere,

$$\omega_{S,l} = \omega_B \sqrt{\frac{l}{2l+1}}. \tag{B.34}$$

When  $D$  equals zero,  $\hat{V}_m$  reduces to a block diagonal matrix. For finite  $D$ , the off diagonal ( $l_i \neq l_j$ ) terms in  $\hat{V}_m$  become finite.

### B.1.3 Optical absorption

Using our matrix notation, the coupling between the incident light field Eq. (3.12) can be expressed as,

$$V_{ext} = E_0(t) (n_0 e) \mathbf{X}_m^T \hat{B}_m^{*T} \hat{R}^{L+2} \hat{Y}_M, \tag{B.35}$$

where  $\hat{Y}_M$  is a block diagonal matrix:

$$\hat{Y}_M = \begin{pmatrix} \hat{Y}_{1M} & & 0 \\ & \dots & \\ 0 & & \hat{Y}_{l_{max}M} \end{pmatrix}, \tag{B.36}$$

with

$$\hat{Y}_{LM} = \begin{pmatrix} Y_{LM}(\Omega_C) & 0 \\ 0 & Y_{LM}(\Omega_S) \end{pmatrix}. \quad (\text{B.37})$$

The Lagrangian of the system becomes:

$$\begin{aligned} L_m &= \frac{n_0 m_e}{2} [\dot{\mathbf{X}}_m^T \hat{T}_m \dot{\mathbf{X}}_m - \mathbf{X}_m^T \hat{V}_m \mathbf{X}_m] \\ &\quad - E_0(t) (n_0 e) \mathbf{X}_m^T \hat{B}_m^{*T} \hat{R}^{L+2} \hat{Y}_M \end{aligned} \quad (\text{B.38})$$

and leads to the following equations of motion:

$$\begin{aligned} \frac{n_0 m_e}{2} [\omega^2 (\hat{T}_m + \hat{T}_m^T) - (\hat{V}_m + \hat{V}_m^T)] \mathbf{X}_{lm} = \\ E_0(t) (n_0 e) \hat{B}_m^{*T} \hat{R}^{L+2} \hat{Y}_M \end{aligned} \quad (\text{B.39})$$

Due to the orthogonality of the spherical harmonics, the term on the right hand side of the above equation is nontrivial only when  $M = m$ . The frequency dependent polarizability is equal to the multipole moment of the system when the amplitude of  $E_0(t)$  is set to one,

$$\begin{aligned} \alpha(\omega)_m &= \int r^L \sigma_m^*(\mathbf{r}) Y_{LM}(\Omega) dS = \left( \hat{B}_m^{*T} \hat{R}^{L+2} \hat{Y}_m \right)^T \times \\ &\quad \left[ \omega^2 (\hat{T}_m + \hat{T}_m^T) - (\hat{V}_m + \hat{V}_m^T) \right]^{-1} \left( \hat{B}_m^{*T} \hat{R}^{L+2} \hat{Y}_m \right). \end{aligned} \quad (\text{B.40})$$

## Appendix C

### Convergence Test for modeling an extended dielectric surface

In this appendix we present how the Method III (see in Chapter 4) has been tested showing that, for larger and slightly smaller slabs, the calculated results are identical. Figure C.1a shows the geometry of the FDTD simulation domain. The thickness of UPML is fixed at 15 grid lengths. The distance from edge of the nanoparticle to the inner boundary of UPML,  $l$ , is varied. In Figure C.1b, we show the calculated polarization dependent dark-field scattering spectra for different  $l$ . Red curves are the same results as we have shown in Figure 4.8 of Chapter 4, where  $l = 3$  grid lengths. The cyan and brown curves are for  $l = 3 + R = 43$  and  $l = 3 + 2R = 83$  grid lengths, respectively, where  $R$  is the outer radius of the nanoshell. For Method III, these three curves are identical except a little difference ( $\Delta\lambda \leq 5 \text{ nm}$ ) for the p-polarization (top). Results for a finite slab using Method II is also included for comparison. Therefore, we conclude that, using Method III, the effect of induced charges at the edges of our finite slab is negligible and the results obtained are the exact solutions for the scattering spectrum of a nanoparticle on an infinite substrate.

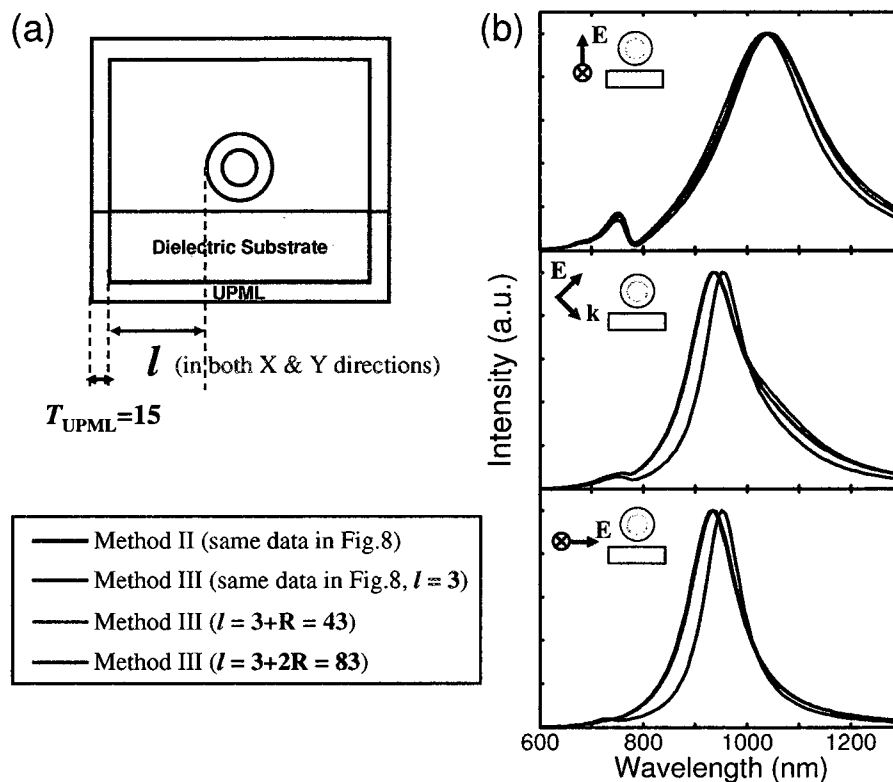


**Figure C.1** Convergence tests for modeling an extended dielectric surface in the FDTD dark-field scattering calculations. (a) Schematic picture depicting the geometry in the FDTD simulations.  $l$  is varied in both X and Y directions.  $T_{UPML}$  is fixed at 15 grid lengths. (b) Calculated dark-field scattering spectra for the three polarizations as shown in insets. Results for different  $l$  using Method III are plotted for a convergence test. Result for a finite slab using Method II is included for comparison.

## References

1. S. Maier, *Plasmonics: Fundamentals and Applications* (Springer, Berlin, 2007).
2. E. Prodan, C. Radloff, N. J. Halas, and P. Nordlander, *Science* **302**, 419 (2003).
3. S. Link and M. A. El-Sayed, *J. Phys. Chem. B* **103**, 8410 (1999).
4. C. J. Murphy, T. K. San, C. J. Orendorff, J. X. Gao, L. Gou, S. E. Hunyadi, and T. Li, *J. Phys. Chem. B* **109**, 13857 (2005).
5. J. Aizpurua, P. Hanarp, D. S. Sutherland, M. Kall, G. W. Bryant, and F. J. G. de Abajo, *Phys. Rev. Lett.* **90**, 057401 (2003).
6. Y. Sun and Y. Xia, *Science* **298**, 2176 (2002).
7. L. J. Sherry, S. H. Chang, G. C. Schatz, R. P. van Duyne, B. J. Wiley, and Y. Xia, *Nano Lett.* **5**, 2034 (2005).
8. S. H. Chen and D. L. Carroll, *Nano Lett.* **2**, 1003 (2002).
9. R. Jin, Y. Wei, C. A. Mirkin, K. L. Kelly, G. C. Schatz, and J. G. Zheng, *Science* **294**, 1901 (2001).
10. I. Pastoriza-Santos and L. M. Liz-Marzan, *Nano Lett.* **2**, 903 (2002).
11. R. D. Averitt, D. Sarkar, and N. J. Halas, *Phys. Rev. Lett.* **78**, 4217 (1997).
12. S. Oldenburg, R. D. Averitt, S. Westcott, and N. J. Halas, *Chem. Phys. Lett.* **288**, 243 (1998).
13. H. Wang, D. W. Brandl, F. Le, P. Nordlander, and N. J. Halas, *Nano Lett.* **6**, 827 (2006).
14. S. H. Chen, Z. L. Wang, J. Ballato, S. H. Foulger, and D. L. Carroll, *J. Am. Chem. Soc.* **125**, 16186 (2003).
15. E. Hao, R. C. Bailey, G. C. Schatz, J. T. Hupp, and S. Li, *Nano Lett.* **4**, 327 (2004).
16. S. Nie and S. R. Emory, *Science* **275**, 1102 (1997).
17. K. Kneipp, Y. Wang, H. Kneipp, L. T. Perelman, I. Itzkan, R. R. Dasari, and M. S. Feld, *Phys. Rev. Lett.* **78**, 1667 (1997).

18. H. X. Xu, E. J. Bjerneld, M. Kall, and L. Borjesson, *Phys. Rev. Lett.* **83**, 4357 (1999).
19. H. Xu and M. Kall, *ChemPhysChem* **4**, 1001 (2003).
20. M. Moskovits, L. Tay, J. Yang, and T. Haslett, *Topics Appl. Phys.* **82**, 215 (2002).
21. G. C. Schatz and R. P. van Duyne, in *Handbook of Vibrational Spectroscopy*, edited by J. M. Chalmers and P. R. Griffiths (John Wiley, Chichester, 2002), pp. 1–16.
22. M. Moskovits and D. H. Jeong, *Chem. Phys. Lett.* **397**, 91 (2004).
23. L. R. Hirsch, R. J. Stafford, J. A. Bankson, S. R. Sershen, B. Rivera, R. E. Price, J. D. Hazle, N. J. Halas, and J. L. West, *Proc. Nat. Acad. Sci. USA* **22**, 47 (2003).
24. C. Loo, A. Lowery, N. J. Halas, J. West, and R. Drezek, *Nano Lett.* **5**, 709 (2005).
25. C. Loo, L. Hirsch, M. H. Lee, E. Chang, J. West, N. J. Halas, and R. Drezek, *Optics Lett.* **30**, 1012 (2005).
26. S. Sershen, S. L. Westcott, N. J. Halas, and J. L. West, *J. Biomed. Mat. Res.* **51**, 293 (2000).
27. L. R. Hirsh, J. B. Jackson, A. Lee, N. J. Halas, and J. L. West, *Anal. Chem.* **75**, 2377 (2003).
28. E. Hao, S. Li, R. C. Bailey, S. Zou, G. C. Schatz, and J. T. Hupp, *J. Phys. Chem. B* **108**, 1224 (2004).
29. A. Moroz, *Chem. Phys.* **317**, 1 (2005).
30. G. Raschke, S. Brogl, A. S. Sush, A. L. Rogath, T. A. Klar, J. Feldman, B. Fieres, N. Petkov, T. Bein, A. Nichtl, and K. Kurzinger, *Nano Lett.* **4**, 1853 (2004).
31. Y. Sun and Y. Xia, *Anal. Chem.* **74**, 5297 (2002).
32. T. V. Teperik, V. V. Popov, and F. J. G. de Abajo, *Phys. Rev. B* **69**, 155402 (2004).
33. R. Baer, D. Neuhauser, and S. Weiss, *Nano Lett.* **4**, 85 (2004).



34. E. Prodan and P. Nordlander, *Nano Lett.* **3**, 543 (2003).
35. D. P. O'Neal, L. R. Hirsch, N. J. Halas, J. D. Payne, and J. L. West, *Cancer Lett.* **209**, 171 (2004).
36. J. B. Jackson and N. J. Halas, *Proc. Nat. Acad. Sci. USA* **101**, 17930 (2004).
37. E. Prodan and P. Nordlander, *J. Chem. Phys.* **120**, 5444 (2004).
38. N. K. Grady, N. J. Halas, and P. Nordlander, *Chem. Phys. Lett.* **399**, 167 (2004).
39. H. Metiu, *Prog. Surf. Sci.* **17**, 153 (1984).
40. C. Charnay, A. Lee, S.-Q. Man, C. E. Moran, C. Radloff, R. K. Bradley, and N. J. Halas, *J. Phys. Chem. B* **107**, 7327 (2003).
41. C. E. Talley, J. B. Jackson, C. Oubre, N. K. Grady, C. W. Hollars, S. M. Lane, T. R. Huser, P. Nordlander, and N. J. Halas, *Nano Lett.* **5**, 1569 (2005).
42. H. Wang, G. P. Goodrich, C. Oubre, P. Nordlander, and N. Halas, *J. Phys. Chem. B* **109**, 11083 (2005).
43. G. Shvets and Y. A. Urzhumov, *Phys. Rev. Lett.* **93**, 243902 (2004).
44. P. K. Aravind, A. Nitzan, and H. Metiu, *Surf. Sci.* **110**, 189 (1981).
45. K. R. Li, M. I. Stockman, and D. J. Bergman, *Phys. Rev. Lett.* **91**, 227402 (2003).
46. F. Tam, C. Moran, and N. J. Halas, *J. Phys. Chem. B* **108**, 17290 (2004).
47. A. Dmitriev, C. Hägglund, S. Chen, H. Fredriksson, T. Pakizeh, M. Käll, and D. S. Sutherland, *Nano Lett.* **8**, 3893 (2008).
48. V. Myroshnychenko, J. Rodrigues-Fernandez, I. Pastoriza-Santos, A. M. Funston, C. Novo, P. Mulvaney, L. M. Liz-Marzan, and F. J. G. de Abajo, *Chem. Soc. Rev.* **37**, 1792 (2008).
49. T. Sannomiya, C. Hafner, , and J. Voros, *Nano Lett.* **8**, 3450 (2008).
50. K. M. Mayer, S. Lee, H. Liao, B. C. Rostro, A. Fuentes, P. T. Scully, C. L. Nehl, and J. H. Hafner, *ACS Nano* **2**, 687 (2008).
51. C. Sönnichsen, T. Franzl, T. Wilk, G. von Plessen, J. Feldmann, O. Wilson, and P. Mulvaney, *Phys. Rev. Lett.* **99**, 077402 (2002).

52. P. Nordlander and E. Prodan, *Nano Lett.* **4**, 2209 (2004).
53. F. Le, N. Z. Lwin, J. M. Steele, M. Kall, N. J. Halas, and P. Nordlander, *Nano Lett.* **5**, 2009 (2005).
54. F. Le, N. Z. Zwin, N. J. Halas, and P. Nordlander, *Phys. Rev. B* **76**, 165410 (2007).
55. A. Pinchuk, A. Hilger, and G. von Plessen, *Nanotechnology* **15**, 1890 (2004).
56. J. J. Mock, R. T. Hill, A. Degiron, S. Zauscher, A. Chilkoti, and D. R. Smith, *Nano. Lett.* **8**, 2245 (2008).
57. A. M. Michaels, J. Jiang, and L. E. Brus, *J. Phys. Chem. B* **104**, 11965 (2000).
58. H. Wang, C. S. Levin, and N. J. Halas, *J. Am. Chem. Soc.* **127**, 14992 (2005).
59. S. J. Oldenburg, S. L. Westcott, R. D. Averitt, and N. J. Halas, *J. Chem. Phys.* **111**, 4729 (1999).
60. C. L. Haynes and R. P. V. Duyne, *J. Phys. Chem. B* **105**, 5599 (2001).
61. L. Qin, S. Zou, C. Xue, A. Atkinson, G. C. Schatz, and C. A. Mirkin, *Proc. Natl. Acad. Sci. USA* **103**, 13300 (2006).
62. D. P. Fromm, A. Sundaramurthy, A. Kinkhabwala, P. J. Schuck, G. S. Kino, and W. E. Moerner, *J. Chem. Phys.* **124**, 061101 (2006).
63. A. J. Hallock, P. L. Redmond, and L. E. Brus, *Proc. Natl. Acad. Sci. USA* **102**, 1280 (2005).
64. P. Nordlander, C. Oubre, E. Prodan, K. Li, and M. I. Stockman, *Nano Lett.* **4**, 899 (2004).
65. Z. Wang, S. Pan, T. D. Krauss, H. Dui, and L. J. Rothberg, *Proc. Nat. Acad. Sci. USA* **100**, 8638 (2003).
66. K. F. Domke, D. Zhang, and B. Pettinger, *J. Am. Chem. Soc.* **128**, 14721 (2006).
67. C. C. Neacsu, J. Dreyer, N. Behr, and M. B. Raschke, *Phys. Rev. B* **73**, 193406 (2006).
68. J. Zhang, Y. Fu, M. H. Chowdury, and J. R. Lakowicz, *J. Phys. Chem. C* **111**, 11784 (2007).

69. J.-H. Tian, B. Liu, X. Li, Z.-L. Yang, B. Ren, S.-T. Wu, N. Tao, and Z.-Q. Tian, *J. Am. Chem. Soc.* **128**, 14748 (2006).
70. D. R. Ward, N. K. Grady, C. S. Levin, N. J. Halas, Y. P. Wu, P. Nordlander, and D. Natelson, *Nano Lett.* **7**, 1396 (2007).
71. D. R. Ward, N. J. Halas, J. W. Ciszek, J. M. Tour, Y. P. Wu, P. Nordlander, and D. Natelson, *Nano Lett.* **8**, 919 (2008).
72. E. Prodan, P. Nordlander, and N. J. Halas, *Nano Lett.* **3**, 1411 (2003).
73. D. W. Brandl, C. Oubre, and P. Nordlander, *J. Chem. Phys.* **123**, 024701 (2005).
74. D. W. Brandl, N. A. Mirin, and P. Nordlander, *J. Phys. Chem. B* **110**, 12302 (2006).
75. K. S. Yee, *IEEE Trans. Antenn. Propag.* **17**, 585 (1966).
76. A. Taflove and S. C. Hagness, *Computational Electrodynamics: The Finite-Difference Time Domain Method* (Artech House, INC., Norwood, MA 02062, 2000).
77. D. M. Sullivan, *Electromagnetic Simulation Using the FDTD Method* (IEEE Press, Piscataway, NJ 08855-1331, 2000).
78. G. Mur, *IEEE Trans. Electromagnetic Compatibility* **23**, 377 (1981).
79. J. Ren, O. P. Gandhi, L. R. Walker, J. Fraschilla, and C. R. Boerman, *IEEE Microwave Guided Wave Lett.* **4**, 109 (1994).
80. K. H. Lee and S. R. Laxpati, *Proc. 1996 IEEE Antennas and Propagation Society International Symposium, Baltimore, MD* **2**, 1284 (1996).
81. M. Fujii, D. Lukashevich, I. Sakagami, and P. Russer, *IEEE Trans. Microwave Wireless Comp. Lett.* **13**, 469 (2003).
82. S. Schmidt and G. Lazzi, *IEEE Trans. Microwave Theory Tech.* **52**, 1952 (2004).
83. O. Hess, C. Hermann, and A. Klaedtke, *Phys. Stat. Sol.* **197**, 605 (2003).
84. W. Kuang, W. J. Kim, and J. D. O'Brien, *J. Lightwave Technol.* **25**, 2612 (2007).

85. B. Wu, E. Yang, J. A. Kong, J. A. Oswald, K. A. McIntosh, L. Mahoney, and S. Verghese, *Microw. Opt. Techn. Lett.* **27**, 81 (2000).
86. C. Oubre and P. Nordlander, *J. Phys. Chem. B* **109**, 10042 (2005).
87. C. Oubre and P. Nordlander, *J. Phys. Chem. B* **108**, 17740 (2004).
88. D. W. Brandl and P. Nordlander, *J. Chem. Phys.* **126**, 144708 (2007).
89. F. Hao and P. Nordlander, *Appl. Phys. Lett.* **89**, 103101 (2006).
90. H. Wang, Y. Wu, B. Lassiter, C. L. Nehl, J. H. Hafner, P. Nordlander, and N. J. Halas, *Proc. Natl. Acad. Sci. USA* **103**, 10856 (2006).
91. S. L. Westcott, J. B. Jackson, C. Radloff, and N. J. Halas, *Phys. Rev. B* **66**, 155431 (2002).
92. L. He, E. A. Smith, M. J. Natan, and C. D. Keating, *J. Phys. Chem. B* **108**, 10973 (2004).
93. N. Papanikolaou, *Phys. Rev. B* **75**, 235426 (2007).
94. N. Nedyalkov, T. Sakai, T. Miyanishi, and M. Obara, *J. Phys. D* **39**, 5037 (2006).
95. G. Leveque and O. J. F. Martin, *Opt. Express* **14**, 9971 (2006).
96. S.-K. Eah, H. M. Jaeger, N. F. Scherer, G. P. Wiederrecht, and X.-M. Lin, *J. Phys. Chem. B* **109**, 11858 (2005).
97. A. Rueda, M. Stemmler, R. Bauer, K. Mullen, Y. Fogel, and M. Kreiter, *New. J. Phys.* **10**, 113001 (2008).
98. W. H. Park, S. H. Ahn, and Z. H. Kim, *ChemPhysChem*. **9**, 2491 (2008).
99. M. G. Boyle, J. Mitra, and P. Dawson, *Appl. Phys. Lett.* **94**, 233118 (2009).
100. M. D. Malinsky, K. L. Kelly, G. C. Schatz, and R. P. van Duyne, *J. Phys. Chem. B* **105**, 2343 (2001).
101. M. W. Knight, Y. P. Wu, J. B. Lassiter, P. Nordlander, and N. J. Halas, *Nano Lett.* **9**, 2188 (2009).
102. S. A. Maier, *Opt. Express* **14**, 1957 (2006).
103. S. Lal, N. K. Grady, J. Kundu, C. S. Levin, J. B. Lassiter, and N. J. Halas, *Chem. Soc. Rev.* **37**, 898 (2008).

104. S. J. Lee, J. M. Baik, and M. Moskovits, *Nano Lett.* **8**, 3244 (2008).
105. J. M. Baik, S. J. Lee, and M. Moskovits, *Nano Lett.* **9**, 672 (2009).
106. T. A. Laurence, G. Braun, C. Talley, A. Schwartzberg, M. Moskovits, N. Reich, and T. Huser, *J. Am. Chem. Soc.* **131**, 162 (2009).
107. C. L. Du, M. X. Wang, Y. M. You, T. Chen, H. Y. Chen, and Z. X. Shen, *Chem. Phys. Lett.* **473**, 317 (2009).
108. I. Yoon, T. Kang, W. Choi, J. Kim, Y. Yoo, S. W. Joo, Q. H. Park, H. Ihee, and B. Kim, *J. Am. Chem. Soc.* **131**, 758 (2009).
109. M. Spuch-Calvar, L. Rodrigues-Lorenzo, M. P. Morales, R. A. Alvarez-Puebla, and L. M. Liz-Marzan, *J. Phys. Chem. C* **113**, 3373 (2009).
110. J. M. Oran, R. J. Hinde, N. A. Hatab, S. T. Retterer, and M. J. Sepaniak, *J. Raman Spectr.* **39**, 1811 (2008).
111. H. Ko, S. Singamaneni, and V. V. Tsukruk, *Small* **4**, 1576 (2008).
112. H. Wei, U. Hakansson, Z. Yang, F. Hook, and H. X. Xu, *Small* **4**, 1296 (2008).
113. Z. P. Li, T. Shegai, G. Haran, and H. X. Xu, *ACS Nano* **3**, 637 (2009).
114. M. Pelton, J. Aizpurua, and G. W. Bryant, *Laser and Photon. Rev.* **2**, 136 (2008).
115. M. W. Knight and N. J. Halas, *New. J. Phys.* **10**, 105006 (2008).
116. C. J. Heo, S. H. Kim, S. G. Jang, S. Y. Lee, and S. M. Yang, *Adv. Mat.* **21**, 1726 (2009).
117. J. Ye, P. V. Dorpe, W. V. Roy, G. Borghs, and G. Maes, *Langmuir* **25**, 1822 (2009).
118. J. Ye, P. V. Dorpe, W. V. Roy, K. Lodewijks, I. D. Vlamincx, G. Maes, and G. Borghs, *J. Phys. Chem. C* **113**, 3110 (2009).
119. Y. B. Zheng, Y. W. Yang, L. Jensen, L. Fang, B. K. Juluri, A. H. Flood, P. S. Weiss, J. F. Stoddart, and T. J. Huang, *Nano Lett.* **9**, 819 (2009).
120. W. A. Murray, B. Auguie, and W. L. Barnes, *J. Phys. Chem. C* **113**, 5120 (2009).

121. S. A. Maier, *Nature Mat.* **8**, 699 (2009).
122. N. Liu, L. Langguth, T. Weiss, J. Kastel, M. Fleischhauer, T. Pfau, and H. Giessen, *Nature Mat.* **8**, 758 (2009).
123. B. E. Brinson, J. B. Lassiter, C. S. Levin, R. Bardhan, N. Mirin, and N. J. Halas, *Langmuir* **24**, 14166 (2008).
124. P. B. Johnson and R. W. Christy, *Phys. Rev. B* **6**, 4370 (1972).
125. J. B. Lassiter, J. Aizpurua, L. I. Hernandez, D. W. Brandl, I. Romero, S. Lal, J. H. Hafner, P. Nordlander, and N. Halas, *Nano Lett.* **8**, 1212 (2008).
126. A. Taflove and S. C. Hagness, *Computational Electrodynamics: The Finite-Difference Time Domain Method* (Artech House, INC., Norwood, MA 02062, 2005).
127. P. Nordlander and F. Le, *Appl. Phys. B* **84**, 35 (2006).
128. F. Hao, C. L. Nehl, J. H. Hafner, and P. Nordlander, *Nano Lett.* **7**, 729 (2007).
129. C. Guiffaut and K. Mahdjoubi, *IEEE Antennas and Propagation Magazine* **43**, 94 (2001).